EMBEDDED MICROVASCULAR NETWORKS FOR ELECTRONICALLY RECONFIGURABLE MATERIALS

BY

ANTHONY GRIFFIN

THESIS

Submitted in partial fulfillment of the requirements
for the degree of Master of Science in Materials Science and Engineering
in the Graduate College of the
University of Illinois at Urbana-Champaign, 2015

Urbana, Illinois

Advisers:

Professor Nancy Sottos
Professor Scott White

ABSTRACT

Microvascular networks in biological systems carry out various functions, such as damage repair, temperature regulation, and nutrient transport. Biological vasculature has inspired the use of microfluidic networks in various synthetic materials to achieve similar functionality such as vascular-based healing and cooling in structural composites.

A recent use of microvascular structures in synthetic materials is for the selective alteration of electromagnetic properties of materials using conductive fluids. Specifically a Gallium-Indium alloy which is liquid at room temperature is used to reconfigure radio frequency wireless signal devices. Previous work has focused on the use of microelectromechanical systems, solid state diodes, or physical actuation to reconfigure such devices, but various problems limit the applicability of these solutions to high power applications.

This thesis first describes a new set of fabrication techniques used to overcome various issues with previous applications of conductive fluids in microvascular networks for electromagnetic configurability. Vascular networks are formed in a structural epoxy which is bonded to the active device. The channels selectively contact electronic components, forming conductive pathways between components when filled with liquid metal.

The fabrication techniques described are then used to fabricate two novel reconfigurable radio frequency wireless devices, a coplanar waveguide and a cross-polarization patch antenna. The coplanar waveguide achieves phase reconfiguration with a single serpentine channel design, while the cross-polarization antenna achieves polarization reconfiguration using dual 3D network architectures.

ACKNOWLEDGEMENTS

I would like to thank everyone who has helped me explore the unending possibilities of life and allowed me to take the road less travelled. I especially would like to express my deep gratitude to my parents, Rick and Lu, for raising me as a free spirit and feeding my curiosity of the world, which led me to be an engineer and scientist. Their support in my college and graduate education, going months without seeing me even though they are just a couple hours away, was very meaningful to me. I would also like to thank my brother, Alex, for pushing the limits of my knowledge and challenging my supposed knowledge. By asking the questions no one else is brave enough to ask, he pushed me to further explore the true nature of the universe and our place in it. I appreciate further support from my aunt, grandparents, cousins, and other family members who have supported me along the way.

I am truly humbled by the unending support and advice of my advisers, Professor Nancy Sottos and Professor Scott White. Their guidance, patience, connections, funding, and various celebrations have been critical in my pursuit of higher knowledge. It is their work and support which has inspired me to continue my education in graduate school. I also wish to thank the various graduate students who have guided me throughout my education, Dr. Henghua Jin, Anthony Coppola, and Dr. Jason Patrick. All three of them have continuously been positive influences on my research and life in general.

I would like to acknowledge support and assistance from the Autonomous Material Systems (AMS) research group, which has provided a unique collaborative environment with many wonderful people. Further support, facilities, and guidance were provided by the Beckman Institute, the Imaging Technology group at the Beckman Institute, Dr. Leilei Yin, and various

others. I deeply value all the collaborators who have worked through some very tough problems with me, including Professor Gregory Huff at Texas A&M University, Professor Jennifer Bernhard, Dr. Joel Barrera, Kurt Schab, and Hong Pan. Finally, I want to acknowledge the University of Illinois at Urbana-Champaign, the College of Engineering, and the Department of Materials Science and Engineering for fostering such an enthusiastic, supportive, and open environment, making me proud to say I am a materials engineer from UIUC.

TABLE OF CONTENTS

CHAPTER 1: Introduction....1
1.1 Thesis Scope....2
1.2 Organization of Thesis....3
1.3 References....4

CHAPTER 2: Literature Review....6
2.1 Introduction....6
2.2 Reconfigurable RF Wireless Electronic Devices....6
2.3 Fabrication of Microfluidic Networks....11
2.4 Summary....13
2.5 References....14
2.6 Figures....18

CHAPTER 3: Materials and Methods....26
3.1 Introduction....26
3.2 Microvascular Matrix Material Selection....26
3.3 Bonding of Vascularized Epoxy to RF Devices....31
3.4 Conductive Fluid Selection and Ohmic Contact....32
3.5 Conclusions....34
3.6 References....35
3.7 Tables....37
3.8 Figures....39

CHAPTER 4: Phase Reconfigurable Coplanar Waveguides....50
4.1 Introduction....50
4.2 Proof of Concept Phase Variable CPW....51
4.3 Redesigned Serpentine Network Phase Variable CPW....53
4.4 References....57
4.5 Figures....58

CHAPTER 5: Polarization Reconfigurable Patch Antenna....66
5.1 Introduction....66
5.2 Single Channel Polarization Reconfigurable Antenna....67
5.3 Dual Channel Polarization Reconfigurable Antenna....69
5.4 References....70
5.5 Figures....72

CHAPTER 6: Conclusions and Future Work....80
6.1 Conclusions....80
6.2 Future Work....81
6.3 References....83
6.4 Figures....84

CHAPTER 1

INTRODUCTION

Radio frequency (RF) antennas date back over a century, almost to the experimental confirmation of James Maxwell's theory of electromagnetism by Heinrich Hertz in 1886. While the use of electromagnetic radiation for communications had been lightly explored, Guglielmo Marconi was the first to patent an RF signal transmission system in 1894 and won the 1909 Nobel Prize in Physics for his pioneering work in this area.[1,2] Materials for the production and packaging of wireless communication devices have existed since this time, starting with simple conductive metal rods. As the need and uses for RF signal devices have expanded, so have the types of materials used to make and package them. Even so, the actual signal transmission portions of commercial RF antennas are still mostly made from a simple electrically conductive material – copper, which has been readily adapted to the changes in materials for modern packaging and larger integrated systems. Copper traces are ubiquitous in printed circuit-board (PCB) technology, where typically thin, planar copper layers are patterned on low dielectric, fiber reinforced composite substrates.[3-5] However, with the integration of microfluidic systems for reconfigurable RF signal devices, new materials and fabrication methods must be explored which compliment current PCB technology.

Microvascular networks are pervasive in nature and enable may critical functions of biological systems. For example, the human circulatory system vasculature facilitates thermal regulation, nutrient transport, and healing.[1-3] Inspired by biological systems, microvascular networks have been introduced into synthetic materials to provide a range of functions. In the past 15 years, microvascular polymers and composites have been developed for use in chemical

analysis, synthetic biological materials, cooling critical electronic components, and self-healing.[4-7]

Synthetic vasculature is produced by a wide array of fabrication methods. Initially 2D microvascular networks were created by soft lithography in relatively soft polymers, such as polydimethylsiloxane (PDMS). 3D vascular structures were fabrication by layering of these 2D networks.[8-10] Since then, many methods for creating vascular networks have been evaluated, including etching, electrostatic discharge, stereolithography, 2-photon polymerization, and incorporation of sacrificial materials.[11-16] Of particular interest to this work is the use of 3D printing to fabricate microvascular networks with the ability to form 3D, interconnecting structures and rapidly iterate network design.[17-20] This method can also be used in a range of materials and is readily scalable, overcoming many limitations faced by other fabrication methods.

1.1 Thesis Scope

The focus of this Thesis is to utilize microvascular networks embedded within a structural polymer to reconfigure radio-frequency (RF) active wireless signal devices. This is achieved through the use of 3D printing of a sacrificial material directly onto traditional wireless electronic devices then casting a carefully selected resin matrix over the assembly. The resulting networks are then filled with a conductive fluid in order to alter the physical characteristics of wireless signal devices, causing a change of their electronic behavior. The movement of conductive fluid to discrete predetermined positions within the network results in distinctive reconfigurations of the electronic signal. In this work, we demonstrate both phase reconfiguration in a co-planar waveguide (CPW) and polarization reconfiguration in a novel cross antenna design.

1.2 Organization of Thesis

In Chapter 2, background literature is reviewed including reconfiguration methods for radio frequency signal devices, as well as microfluidic network fabrication methods. Chapter 3 focuses on the fabrication methodology, materials selection, and network characterization processes used for this work which is also applicable to future efforts. In Chapter 4, the design and development of an 8-state additive phase reconfigurable CPW using methods described in the previous chapter is covered. Chapter 5 encompasses multiple design and fabrication iterations towards the development of a novel 3-state polarization reconfigurable cross antenna. In Chapter 6, the conclusions of this work are summarized, and future work in this area is briefly described.

1.3 References

1. N. Charkoudian, Skin blood flow in adult human thermoregulation: *How it Works, When It Does Not, and Why*. Mayo Clinical Proceedings, 2003, 78, p. 603-612.
2. C.G. Crandall, T.E. Wilson, and K. C. Kregel, *Mechanisms and modulators of temperature regulation.* Journal of Applied Physiology, 2010, 109, p. 1219-1220.
3. P. Martin, *Wound Healing – Aiming for perfect skin regeneration*. Science, 1997, 276, p. 75-81.
4. V. Srinivasan, V.K. Pamula, and R.B. Fair, *An integrated digital microfluidic lab-on-a-chip for clinical diagnostics on human physiological fluids*. Lab on a Chip, 2004, 4, p. 310-315.
5. N.W. Choi, M. Cabodi, B. Held, J.P. Gleghord, L.J. Bonassar, and A.D. Stroock, *Microfludic scaffolds for tissue engineering.* Nature Materials, 2007, 6, p. 908-915.
6. X. Wei, Y. Joshi, and M.K. Patterson, *Experimental and numerical study of a stacked microchannel heat sink for liquid cooling of microelectronic devices.* Transactions of the American Society of Mechanical Engineers, 2007, 129, p. 1432-1444.
7. K.S. Toohey, N.R. Sottos, J.A. Lewis, J.S. Moore, and S.R. White, *Self-healing materials with microvascular networks.* Nature Materials, 2007, 6, p. 581-585.
8. Y. Xia and G. M. Whitesides, *Soft Lithography*. Annual Review of Materials Science, 1998, 28, p. 153-184.
9. Y. Xia and G. M. Whitesides, *Soft Lithography*. Angewandte Chemie International Edition, 1998, 37, p. 550-575.
10. J. C. Love, J. R. Anderson, and G. M. Whitesdies, *Fabrication of three-dimensional microfluidic systems by soft lithography.* Materials Research Socieity Bulletin, 2001, p. 523-528.
11. J. H. Huang, J. Kim, N. Agrawal, A. P. Sudarsan, J. E. Maxim, A. Jayaraman, and V. M. Ugaz, *Rapid Fabrication of Bio-inspired 3D Microfluidic Vascular Networks.* Advanced Materials, 2009, 21, p. 3567-3571.
12. K. D. Behler and E. D. Wetzel, *Novel techniques for vascularization of structures: electrohydrodynamic viscous fingering and electrical treeing.* 27th Army Science Conference, 2008, p. 1-8.
13. R. B. Wicker, A. V. Ranade, and F. Medina, *Embedded micro-channel fabrication using line-scan stereolithography.* Assembly Automation, 2005, 25, p. 316-329.
14. D. Lim, Y. Kamotani, B. Cho, J. Mazumder, and S. Takayama, *Fabrication of microfluidic mixers and artificial vasculature using a high-brightness diode-pumped Nd:YAG laser direct write method.* Lab on a Chip, 2003, 3, p. 318-323.
15. W. Zhou, S. M. Kuebler, K. L. Braun, T. Yu, J. K. Cammack, C. K. Ober, J. W. Perry, and S. R. Marder, *An efficient two-photon-generated photoacid applied to positive-ton 3D microfabrication.* Science, 2002, 296, p. 1106-1109.
16. L. M. Bellan, S. P. Singh, P. W. Henderson, T. J. Porri, H. G. Craighead, and J. A. Spector, *Fabrication of an artificial 3-dimensional vascular network using sacrificial sugar structures.* Soft Matter, 2009, 5, p. 1354-1357.
17. D. Therriault, R.F. Sheperd, S.R. White, and J.A. Lewis, *Fugitive inks for direct-write assembly of three-dimensional microvascular networks.* Advance Materials, 2005, 17, p. 395-399.

18. R.B. Oueslati, D. Therriault, and S. Martel, *PCB-integrated heat exchanger for cooling electronics using microchannels fabricated with the direct-write method.* IEEE Tranasctions on components and packing technologies, 2008, 31, p. 869-874.
19. B.D. Kozola, L.A. Shipton, V.K. Natrajan, K.T. Christensen, and S.R. White, *Characterization of Active Cooling and Flow Distribution in Microvascular Polymers*. Journal of Intelligent Material Sytems and Structures, 2010, 21, p. 1147-1156.
20. C.J. Hansen, W. Wu, K.S. Toohey, N.R. Sottos, S.R. White, and J.A. Lewis, *Self-healing materials with interpenetrating microvascular networks*. Advanced Materials, 2009, 21, p. 1-5.

CHAPTER 2

LITERATURE REVIEW

2.1 Introduction

The literature review presented here will give an overview of the two primary bodies of work which motivate this thesis: tunable radio-frequency (RF) electronic devices as well as the fabrication and use of microvascular networks in synthetic materials. Specifically, the use of microelectromechanical systems (MEMS), solid-state devices, mechanical actuation, and fluidic networks for reconfiguration of RF signal devices will be the focus of section 2.2. Section 2.3 will review microvascular fabrication techniques with an emphasis on 3D printing of sacrificial materials.

2.2 Reconfigurable RF Wireless Electronic Devices

2.2.1 Background

The need for beamforming, pattern-adjustable wireless systems which improve efficiency and enable spatially directed communications has motivated a large body of work in reconfigurable, tunable wireless RF devices. The performance of wireless signal devices is dictated by geometry, physical dimensions, and material properties. In particular, the geometry of a wireless device is a key factor to determining resonance frequency, relative phase, and polarization. By altering the geometry of a device during operation, a shift in the characteristic resonant frequency, polarization or phase of the signal is achieved and can be exploited for tunability. Prior work has focused on the use of MEMS, solid-state devices and physical actuation to reconfigure RF devices, but these methods face a variety of technological barriers.[1]

2.2.2 MEMS for Reconfiguration

In many tunable RF wireless devices MEMS are used as mechanical switches which produce a physical actuation from electrostatic forces enabled by a direct current (DC) bias. Cetiner et al. demonstrated a frequency and polarization reconfigurable planar patch antenna in which copper "pixels" were conductively connected or disconnected using MEMS switches. The geometry and size of the antenna was effectively altered by connecting the various pixels together, giving rise to different modes of operation based on the effective geometry as shown by the schematics in Figure 2.1.[2]

MEMS devices have also been utilized to achieve continuous frequency configurability in CPW microstrip antennas by partially actuating over a range of bias voltages.[3] CPW phase reconfiguration was demonstrated by Somjit *et al.* [4] through the use of DC bias-controlled MEMS. In this example, MEMS bridges acted as additional tunable capacitors within the system, rather than simple mechanically activated switches. Even though a wide range of reconfigurable RF devices can be realized through the use of MEMS, issues such as impedance mismatch, packaging and manufacturing integration issues, self-actuation, latching, and bridge heating limit their use in high-power applications (Figure 2.2).[4-8] Generally, reconfiguration through conventional MEMS devices is not achievable above an RF signal power of 1W due to these problems.

2.2.3 Solid State Switches for Reconfiguration

Solid state devices, such as varactor and PIN diodes, also show promise for RF signal device reconfiguration. Both of these devices are suitable for tuning RF circuits for a number of reasons. Varactor diodes act as variable capacitors, offering low RF impedance at low or no bias and high capacitance or significantly higher impedance at RF under reverse bias and low capacitance. PIN diodes differ from varactors, offering high capacitance and high RF conductivity at reverse or no bias and a low capacitance and low RF conductivity at forward biases. This behavior allows these diodes to be utilized as DC controlled RF switches.

Yang and Rahmat-Samii [9] achieved polarization configurability in a patch antenna using PIN diodes where the bias was provided by the coaxial feed itself. However, the use of these PIN diodes caused an insertion loss, resulting in an overall loss in power efficiency of the antenna. In addition, the use of DC control circuits required blocking capacitors to isolate the DC control circuit from the RF circuit in order to prevent unwanted harmonic modes from arising.[10,11]

Behdad and Sarabandi [12,13] explored the use of varactor diodes for tunability of a dual-band slot antenna, in which a varactor served as a capacitive load to the slot (Figure 2.3). While the varactor diode in this antenna offered a much lower efficiency loss, a DC bias voltage and the accompanying circuitry and power were still required for operation.[12,13] Field effect transistors have also been utilized to reconfigure RF antenna switch applications, although the significant reduction in radiation efficiency observed has led research to primarily focus on diode switches.[14]

2.2.4 Mechanical Actuation for Reconfiguration

A third approach for RF device reconfiguration, mechanical actuation, is utilized for altering the geometry of RF signal devices. Unlike MEMS or solid-state devices, mechanical actuation is achieved through a range of strategies. One approach utilized the low temperature phase transition of a shape-memory alloy in order to move metallic parasitic plates, altering the radiation pattern of an active ring-patch antenna.[15] While electronic control systems are still required to actuate the shape-memory alloy springs, these control systems can be placed behind a ground plane and do not electrically connect to the antenna at all, unlike MEMS and solid-state control systems (Figure 2.4).[15] Analogous reconfiguration of a similar ring-patch antenna was also demonstrated using a piezoelectric elastomer that deforms under an applied voltage.[16]

Goessling *et al.* [17] switched between bistable modes in bilayer cantilever devices, but again required electrical control systems to produce temperature differences between layers. Others have combined mechanical actuation and fluidic systems in a simple, stretchable dipole antenna, where a liquid metal is enclosed in a single straight channel in an elastomer. When the elastomer matrix is stretched and released along the dipole axis, the liquid metal channel also lengthens and contracts, altering the resonant frequency (Figure 2.5).[18,19] While mechanically actuated systems do not encounter problems faced by MEMS and solid-state devices, such as latching, self-actuation, and interfering electrical control systems, the slow switching time between states and high power requirements for actuation are prohibitive.[15-19]

2.2.5 Fluidic Approaches to Reconfiguration

Fluidic approaches to reconfigure RF devices utilize materials with fluid filled channels and reservoirs to alter physical dimensions, electrically connect discrete antenna patches, and change capacitive loading.[20-24] Kondoh *et al.* [20] utilized gas thermal expansion to rapidly form small gaps in sections of mercury in micromachined channels, allowing for fast switching times with no electrical control systems near the operational antenna. However the toxicity of liquid mercury is generally avoided in production, packaging, and applications of such devices. Meineri *et al.* [21,22] reported the use of ethanol and silicon oil in open microchannels for phase tunability of a CPW (Figure 2.6a). Ethanol, with a low dielectric constant at RF, provided a relatively high differential phase shift of 6° at 10 GHz but caused a significant loss in power efficiency. Silicon oil provided a lower phase shift of 2.5° at 10 GHz but losses were reduced by an order of magnitude. Also, because the microchannels were open on the top, actuated fluid switching was not attempted.[21,22]

More recent work focused on the fabrication of fluid network architectures by soft lithography or laser machining in polydimethylsiloxane (PDMS). The resulting networks were filled with a non-toxic liquid metal, eutectic gallium-indium (EGaIn) (Figure 2.6b).[23,24] This liquid metal was used for tuning solid antenna structures as well as operating as the signal generating structure.[23] PDMS is a soft elastomer which does not impart structural rigidity to devices. More recently, a single microchannel was incorporated into a structural composite to create a switchable antenna through pneumatic movement of EGaIn (Figure 2.6c). A major issue in this work was the undesired transmission line mode originating from the ungrounded liquid metal in the microchannel.[25] Another technical challenge with the use of EGaIn was the

formation of an oxide layer on the channel walls, which interfered with antenna operation when the channel was emptied.[23-25]

2.3 Fabrication of Microfluidic Networks

2.3.1 Planar Networks

Planar networks and microchannels are introduced into a material through a variety of methods. Micromachining simply utilizes computer numeric control (CNC) of mill bits or electrical discharge machining (EDM) to form grooves on the surface of a material that must be joined or bonded with another surface to form closed channels.[26-28] Laser ablation can also be used to remove material in a similar manner to form channels on the order of 30 μm.[29,30] While this fabrication method is applicable to a diversity of materials and can produce small channel diameters (down to 10μm), the relatively high cost of manufacturing, planar nature, and need for surface bonding limit applicability.

More recent work in the area of electronically active fluidic networks employ soft lithography fabrication techniques.[18,19,21-23] Microchannels are formed by molding certain elastomeric polymers, such as PDMS, to lithographically patterned photoresists on silicon wafer substrates. The polymer is then removed from the photoresist and silicon substrate, resulting in surface patterning which is the negative of the photoresist pattern. The patterned polymer layer is then bonded to another flat surface to form a planar channel network with resolution on the order of nanometers (Figure 2.7).[31,32] Planar networks are subsequently stacked or layered in order to form 3D networks, but misalignment of layers can easily occur due to registration errors, and other flaws arise while bonding stacked layers.[33,34]

2.3.2 Three Dimensional Networks

Random 3D vascular networks are formed through either electrostatic discharge or the incorporation of spun soluble fibers. Electrostatic discharge requires that the material to be vascularized has a low dielectric permittivity. The material is then irradiated with high energy electrons (3 MeV or greater) and subsequently hit with a grounded needle, causing an electrical discharge throughout the material. The strength of this discharge creates highly branched hollow channels, with diameters spanning multiple orders of magnitude.[35-37] Highly interconnected network structures are formed by dissolving randomly oriented soluble fibers in a host matrix using a miscible solvent.[38,39] While both electrostatic discharge and embedded soluble fibers rapidly form highly interconnected and pervasive microfluidic networks, neither technique allows for control or reproducibility of network formation.

In contrast, 3D printing techniques enable highly controllable and repeatable network formation. An early approach to 3D printing is known as stereolithography, where a laser is used to cure horizontal slices of a photopolymerizable resin in a bath. After each slice is cured, the portion of the part which is already formed is lowered just underneath the surface of the bath of uncured resin, and the process is repeated layer by layer to form a 3D structure.[40,41] Uncured regions in planar layers stacked between cured regions form the network structures in this case. In two-photon polymerization fabrication, polymerization occurs in 3 dimensions simultaneously with very high resolution, rather than layer by layer.[42] A major setback of two-photon polymerization is small processing volumes.[43]

An alternate 3D fabrication strategy involves printing of sacrificial viscoelastic inks (Figure 2.8). This technique relies on a 3 axis motion controlled print head which contains a

reservoir of ink which is extruded through pressurized nozzles of varying diameter (10 – 500 μm).[44,45] The inks must be shear-thinning to enable flow through small diameter nozzle heads and subsequent 3D scaffold formation.[46,47] 3D structures can either be formed by layering of 2D layers or through direct vertical movement, since the print head can move along the vertical axis while extruding.[47] Once a 3D network structure is formed with the sacrificial ink, it is cast in a liquid resin which is then cured. After curing has taken place, the matrix and embedded ink are heated, the ink melts, and is removed with the application of a light vacuum.[44-47] 3D printing of sacrificial inks has many advantages over other microvascular fabrication techniques including the ability to fabricate complex 3D networks in a variety of polymers and at interfaces of dissimilar materials, high channel resolution, and the ability to fabricate a range of channel sizes in a single print run.[44-49]

2.4 Summary

In this chapter relevant literature in the areas of reconfigurable/tunable RF signal devices and fabrication techniques to form microvascular/microfluidic networks in synthetic material was reviewed. The advantages and limitations of several strategies to achieve RF device reconfiguration were summarized. For this thesis, we selected the use of liquid metal in 3D printed microvascular networks to achieve switchable reconfiguration of RF signal devices.

2.5 References

1. J. T. Bernhard, *Reconfigurable antennas and apertures: State-of-the-art and future outlook*. Proceedings of the Society of Photo-Optical Instrumentation Engineers, 2003, 5055, p. 1-9.
2. B. A. Cetiner, H. Jafarkhani, J. Y. Qian, H.J. Yoo, A. Grau, and F. De Flaviis, *Multifunctional reconfigurable MEMS integrated antennas for adaptive MIMO systems.* IEEE Communications Magazine, 2004, 42, p. 62-70.
3. E. Erdil, K. Topalli, K. M. Unlu, O. A. Civi, and T. Akin, *Frequency tunable microstrip patch antenna using RF MEMS technology*. IEEE Transactions on Antennas and Propagation, 2007, 55, p. 1193-1196.
4. N. Somjit, G. Stemme, and J. Oberhammer, *Power Handling Analysis of High-Power W-Band All-Silicon MEMS Phase Shifters*. IEEE Transactions on Electron Devices, 2011, 58, p. 1548-1555.
5. B. Pillans, J. Kleber, C. Goldsmith, and M. Eberly, *RF power handling of capacitive RF MEMS devices*. IEEE MTT-S International Microwave Symposium Digest, 2002, 1, p. 329-332.
6. B. Jlassi and A. Merdassi, *Design methodology of a high power RF MEMS switch for wireless applications*. 4th Annual Caneus Fly by Wireless Workshop, 2011, p. 1-4.
7. D. Peroulis, S. P. Pacheco, and L. P. B. Katehi, *RF MEMS switches with enhanced power-handling capabilities.* IEEE Transactions on Microwave Theory and Techniques, 2004, 52, p. 59-68.
8. G. H. Huff and J. T. Bernhard, *Integration of packaged RF MEMS switches with radiation pattern reconfigurable square spiral microstrip antennas.* IEEE Transactions on Antennas and Propagation, 2006, 54, p. 464-469.
9. F. Yang and Y. Rahmat-Samii, *A reconfigurable patch antenna using switchable slots for circular polarization diversity*. IEEE Microwave and Wireless Components Letters, 2002, 12, p.96-98.
10. D. Peroulis, K. Sarabandi, L. P. B. Katehi, *Design of reconfigurable slot antennas*. IEEE Transactions on Antennas and Propagation, 2005, 53, p. 645-654.
11. M. K. Fries, M. Grani, and R. Vahldieck, *A reconfigurable slot antenna with switchable polarization.* IEEE Microwave and Wireless Components Letters, 2003, 13, p. 490-492.
12. N. Behdad and K. Sarabandi, *A varactor-tuned dual-band slot antenna*. IEEE Transactions on Antennas and Propagation, 2006, 54, p. 401-408.
13. N. Behdad and K. Sarabandi, *Dual-band reconfigurable antenna with a very wide tunability range*. IEEE Transactions on Antennas and Propagation, 2006, 54, p. 409-416.
14. L. N. Pringle, P. H. Harms, S. P. Blalock, G. N. Kiesel, E. J. Kuster, P. G. Friederich, R. J. Prado, J. M. Morris, and G. S. Smith, *A reconfigurable aperture antenna based on switched links between electrically small metallic patches.* IEEE Transactions on Antennas and Propagation, 2004, 52, p. 1434-1445.

15. S. J. Mazlouman, A. Mahanfar, C. Menon, and R. G. Vaughan, *Square ring antenna with reconfigurable patch using shape memory alloy actuation.* IEEE Transactions on Antennas and Propagation, 2012, 60, p. 5627-5634.
16. S. J. Mazlouman, M. Soleimani, A. Mahanfar, C. Menon, and R. G. Vaughan, *Pattern reconfigurable square ring patch antenna actuated by hemispherical dielectric elastomer.* Electronics Letters, 2011, 47, p. 164-165.
17. B. A. Goessling, T. M. Lucas, E. V. Moiseeva, J. W. Aebersold and C. K. Harnett, *Bistable out-of-plane stress-mismatched thermally actuated bilayer devices with large deflection*. J. Micromech. Microeng., 2011, 21, DOI: 10.1088/0960-1317/21/6/065030.
18. J. So, J. Thelen, A. Qusba, G. J. Hayes, G. Lazzi, and M. D. Dickey, *Reversibly deformable and Mechanically Tunable Fluidic Antennas*. Advanced Functional Materials, 2009, 19, p. 3632-3637.
19. M. Kubo, X. Li, C. Kim, M. Hashimoto, B. J. Wiley, D. Ham, and G. M. Whitesides, *Stretchable Microfluidic Radiofrequency Antennas.* Advanced Materials, 2010, 22, p. 2749-2752.
20. Y. Kondoh, T. Takenaka, T. Hidaka, G. Tejima, Y. Kaneko, and M. Saitoh, *High-reliability, high-performance RF micromachined switch using liquid metal*. J. Microelectromechanical Systems, 2005, 14, p. 214-220.
21. P. Meineri, D. Dubuc, and K. Grenier, *Liquid-based tunable loaded-line phase shifter*. 42nd European Microwave Conference, 2012, p. 393-396.
22. P. Meineri, D. Dubuc, and K. Grenier, *Liquid-based tunable loaded-line phase shifter*. 9th European Radar Conference, 2012, p. 719-722.
23. G. J. Hayes, J. So, A. Qusba, M. D. Dickey, and G. Lazzi, *Flexible Liquid Metal Alloy (EGaIn) Microstrip Patch Antenna*. IEEE Transactions on Antennas and Propagation, 2012, 60, p. 2151-2156.
24. M. Kelley, C. Koo, H. Mcquilken, B. Lawrence, S. Li, A. Han, and G. H. Huff, *Frequency reconfigurable patch antenna using liquid metal as switching mechanism.* Electronics Letters, 2013, p. 1370-1371.
25. A. J. King, J. F. Patrick, N. R. Sottos, S. R. White, G. H. Huff, and J. T. Bernhard, *Microfluidically Switched Frequency-Reconfigurable Slot Antennas*. IEEE Antennas and Wireless Propagation Letters, 2013, 12, p. 828-831.
26. X. Peng and B. Weng, *Forced-Convection and Flow Boiling Heat-Transfer for Liquid Flowing through Microchannels.* International Journal of Heat and Mass Transfer, 1993, 36, p. 3421-3427
27. M. Murali and S. H. Yeo, *Rapid Biocompatible Micro Device Fabrication by Micro Electro-Discharge Machining.* Biomedical Microdevices, 2004, 6, p. 41-45.
28. H. R. Williams, R. S. Trask, and I. P. Bond, *Self-Healing Composite Sandwich Structures.* Smart Materials and Structures, 2007, 16, p. 1198-1207.

29. H. Qi, T. Chen, L. Yao, and T. Zuo, *Micromachining of microchannel on the polycarbonate substrate with CO2 laser direct-writing ablation.* Optics and Lasers in Engineering, 2009, 47, p. 594-598.
30. D. Gomez, I. Goenaga, I. Lizuain, and M. Ozaita, *Femtosecond laser ablation for microfluidics.* Optical Engineering, 2005, 45, p. 051101-051108.
31. Y. Xia and G. M. Whitesides, *Soft Lithography*. Annual review of materials Science, 1998, 28, p. 153-184.
32. B. D. Gates and G. M. Whitesides, *Replication of Vertical Features Smaller than 2 nm by Soft Lithography.* Journal of the American Chemical Society, 2003, 125, p. 14986-14987.
33. S. W. Lee and S. S. Lee, *Shrinkage ratio of PDMS and its alignment method for the wafer level process.* Microsystem Technologies, 2008, 14, p. 205-208.
34. C. Moraes, Y. Sun, and C. A. Simmons, *Solving the shrinkage-induced PDMS alignment registration issue in multilayer soft lithography.* J. Micromech. and Microeng., 2009, 19, DOI: 10.1088/0960-1317/19/6/065015.
35. J. Furuta, E. Hiraoka, and S. Okamoto, *Discharge figures in dielectrics by electron irradiation.* Journal of Applied Physics, 1966, 37, p. 1873-1878.
36. K. D. Behler and E. D. Wetzel, *Novel techniques for vasculatrization of structures: electrohydrodynamic viscous fingering and electrical treeing.* 27th Army Science Conference, 2008, p. 1-8.
37. J.-H. Huang, J. Kim, N. Agrawal, A. P. Sudarsan, J. E. Maxim, A. Jayaraman, and V. M. Ugaz, *Rapid Fabrication of Bio-inspired 3D Microfluidic Vascular Networks*. Advanced Materials, 2009, 21, p. 3567-3571.
38. L. M. Bellan, S. P. Singh, P. W. Henderson, T. J. Porri, H. G. Craighead, and J. A. Spector, *Fabrication of an artificial 3-dimensional vascular network using sacrificial sugar structures.* Soft Matter, 2009, 5, p. 1354-1357.
39. L. M. Bellan, E. A. Strychalski, and H. G. Craighead, *Nanochannels fabricated in polydimethylsiloxane using sacrificial electrospun polyethylene oxide nanofibers.* Journal of Vacuum Sci. and Tech. B, 2008, 26, p. 1728-1731.
40. K. Arcaute, B. K. Mann, and R. B. Wicker, *Stereolithography of three-dimensional bioactive poly(ethylene glycol) constructs with encapsulated cells.* Annals of Biomedial Engineering, 2006, 34, p. 1429-1441.
41. R. B. Wicker, A. V. Ranade, and F. Medina, *Embedded micro-channel fabrication using line-scan stereolithography.* Assembly Automation, 2005, 25, p. 316-329.
42. S. Kawata, H.-B. Sun, T. Tanaka, and K. Takada, *Finer features for functional microdevices.* Nature, 2001, 412, p. 697-698.
43. W. Zhou, S. M. Kuebler, K. L. Braun, T. Yu, J. K. Cammack, C. K. Ober, J. W. Perry, and S. R. Marder, *An efficient two-photon-generated phtoacid applied to positive-tone 3D microfabrication.* Science, 2002, 296, p. 1106-1109.
44. J. A. Lewis and G. M. Gratson, *Direct writing in three dimensions.* Materials Today, 2004, 7, p. 32-39.

45. D. Therriault, S. R. White, and J. A. Lewis, *Chaotic mixing in three-dimensional microvascular networks fabricated by direct-write assembly.* Nature Materials, 2003, 2, p. 265-272.
46. D. Therriault, S. R. White, and J. A. Lewis, *Rheological behavior of fugitive organic inks for direct-write assembly.* Applied Rheology, 2007, 17, p. 10112-10120.
47. J. Bruneaux, D. Therriault, and M. C. Heuzey, *Micro-extrusion of organic inks for direct-write assembly.* Journal of Micromech. and Microeng., 2008, 18, p. 1-11.
48. D. Therriault, R. F. Shepherd, S. R. White, and J. A. Lewis, *Fugitive inks for direct-write assembly of three-dimensional microvascular networks.* Advanced Materials, 2005, 17, p. 395-399.
49. J. A. Lewis, *Direct ink writing of 3D functional materials.* Advanced Functional Materials, 2006, 16, p. 2193-2204.

2.6 Figures

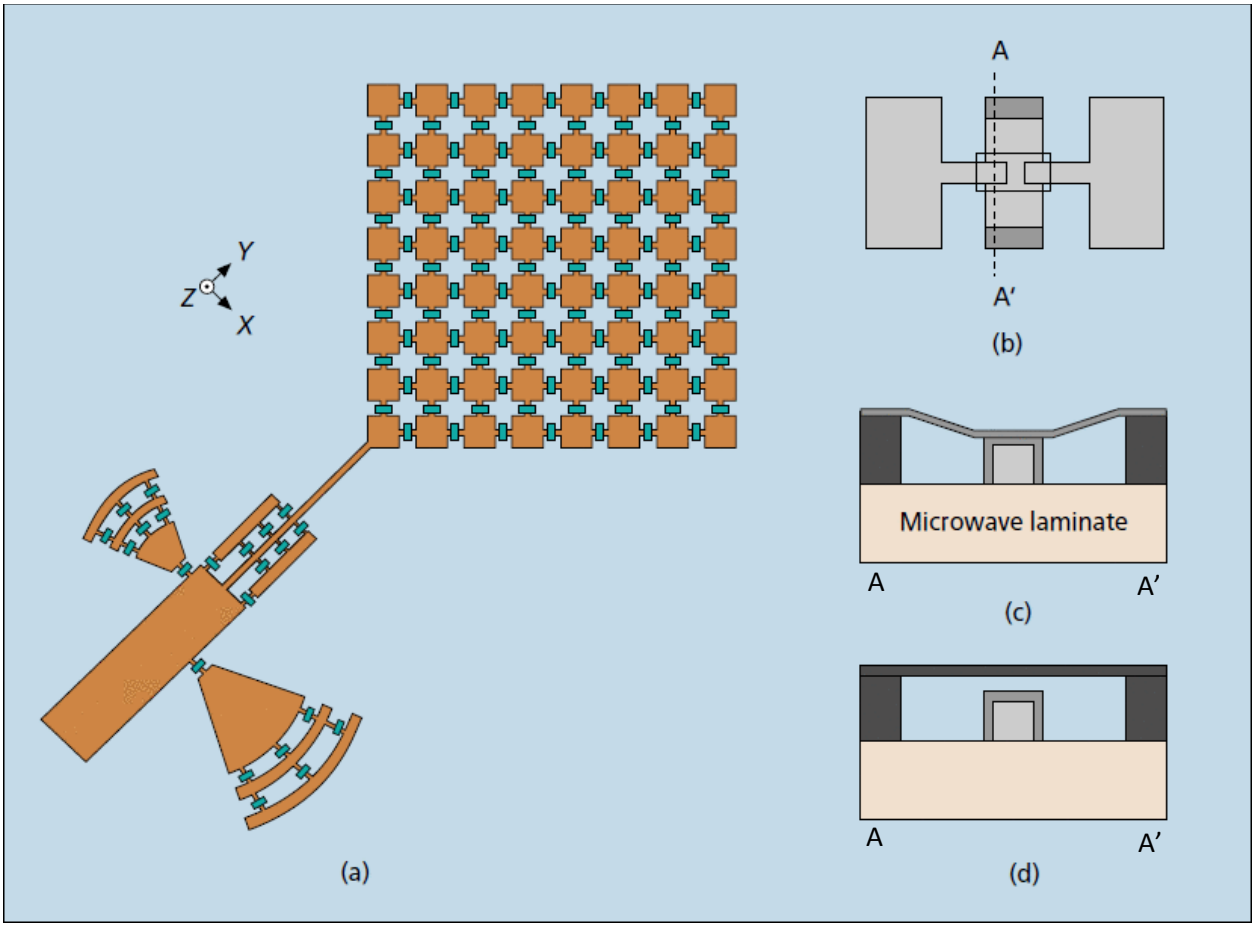

Figure 2.1. Schematics of a frequency and polarization reconfigurable pixel-patch antenna. (a) Schematic of the entire antenna with brown regions representing the copper patches and the MEMS devices represented by teal blocks. (b) Top down schematic of a MEMS bridge used in this antenna for connection switching. (c) Side view schematic of a MEMS bridge in the down position, creating an RF conduction pathway between adjacent patches. (d) Side view schematic of a MEMS bridge in the up position, preventing RF connection between adjacent patches. Figure adapted from [2].

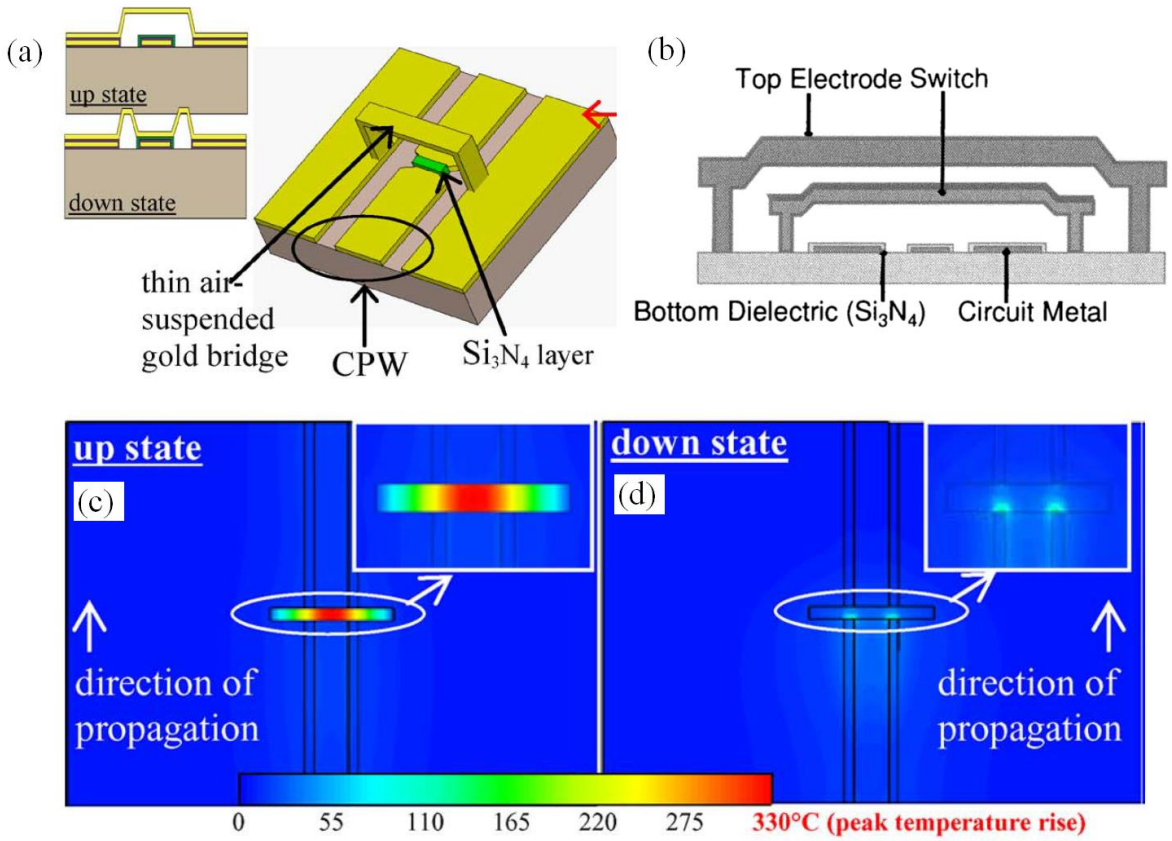

Figure 2.2. Use of MEMS devices in coplanar waveguides to achieve a signal phase shift and various problems encountered. (a) Isometric and side view schematics of a gold MEMS bridge used as a capacitive load in the down state to phase shift a CPW. Maximum RF power: 0.51 W. [4] (b) An additional top electrode switch to pull the bottom switch back after latching or self-actuation occurs. Maximum RF power: 0.8 W. [7] (c) and (d) Thermal maps of a MEMS switch in the up and down state respectively. Huge amounts of heat are generated within the gold bridge while operating at maximum power in the up state. [4]

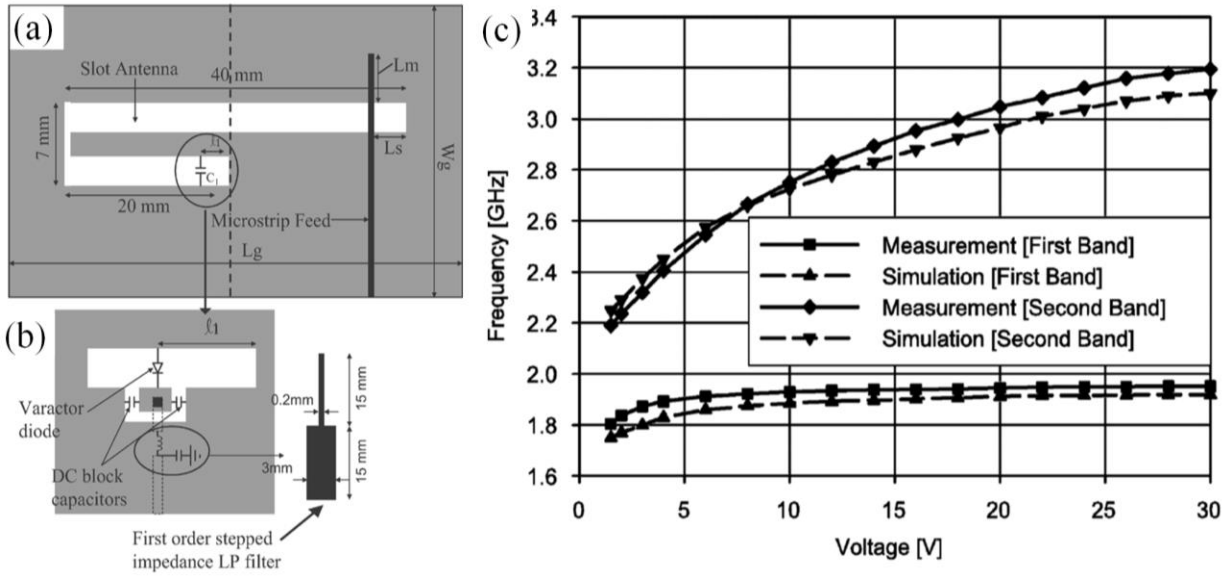

Figure 2.3. A frequency reconfigurable dual-band slot antenna enabled by a varactor diode. (a) Diagram of the entire antenna. (b) Magnified diagram of the varactor diode and associated control systems. (c) Simulated and measured band frequencies as a function of bias voltage across the varactor diode. Figures adapted from [12].

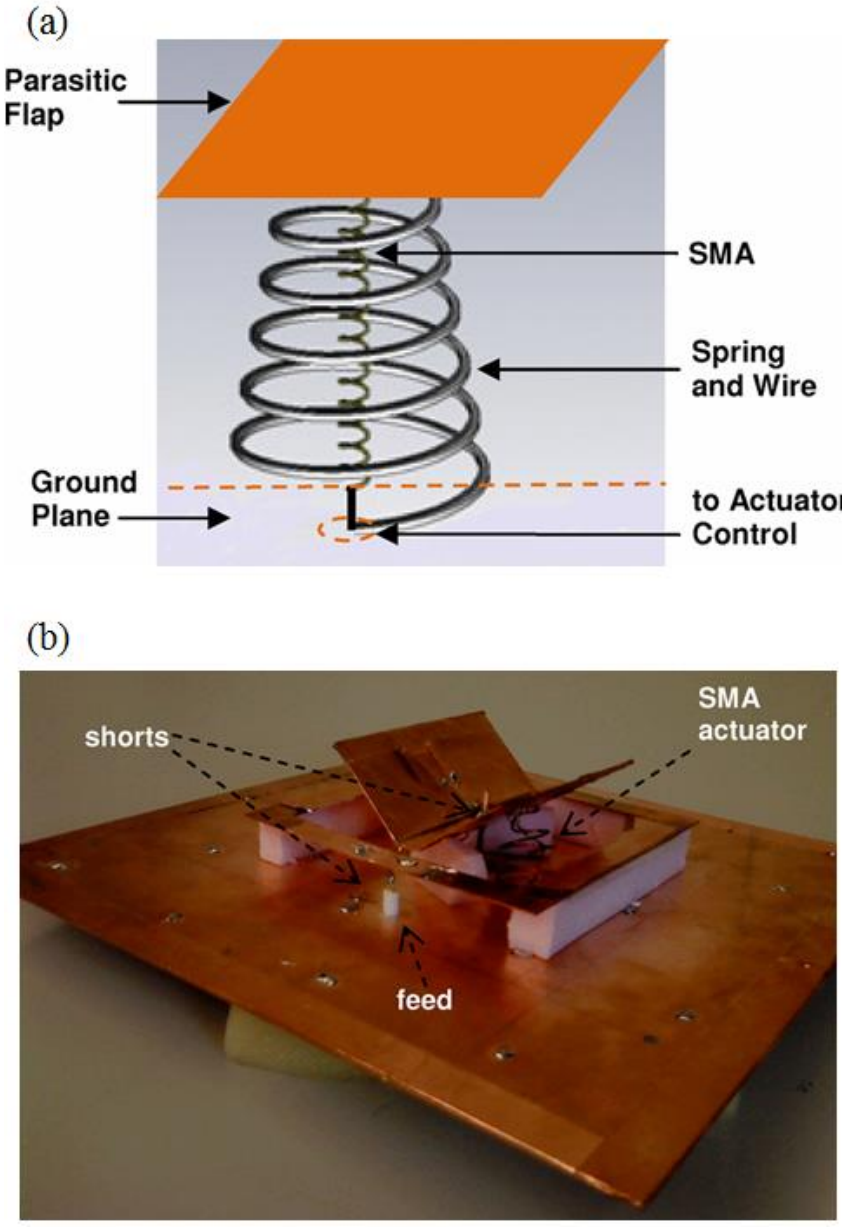

Figure 2.4. A radiation pattern reconfigurable square patch antenna. (a) Diagram of the shape memory alloy actuation system for moving the parasitic flaps up and down. (b) Image of the assembled antenna, with both flaps in the up position. The shape memory alloy can be seen underneath the near flap. Figures adapted from [15].

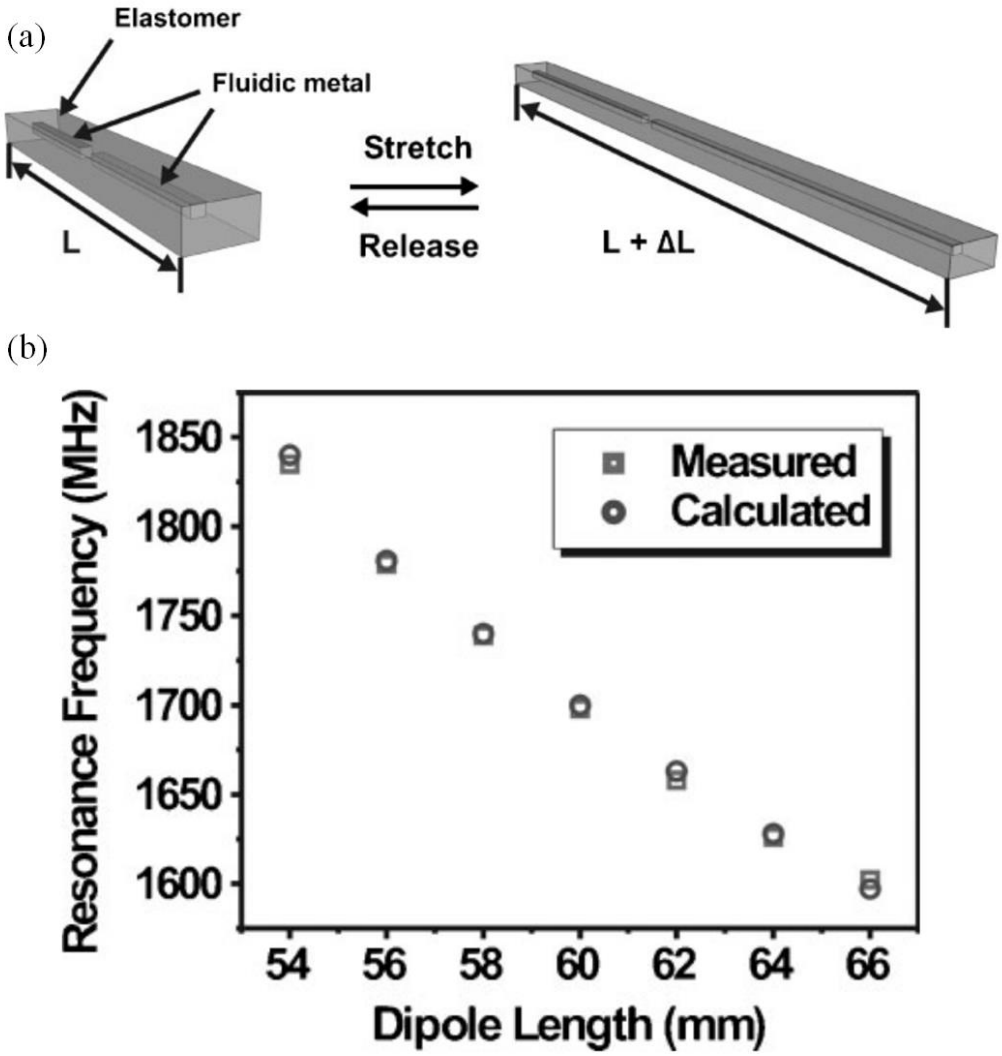

Figure 2.5. (a) Design for a mechanically actuated reconfigurable liquid metal dipole antenna, where closed microchannels in an elastomer contain the liquid metal. (b) Simulated and measured results for the dipole resonance frequency as a function of length. Figures adapted from [18].

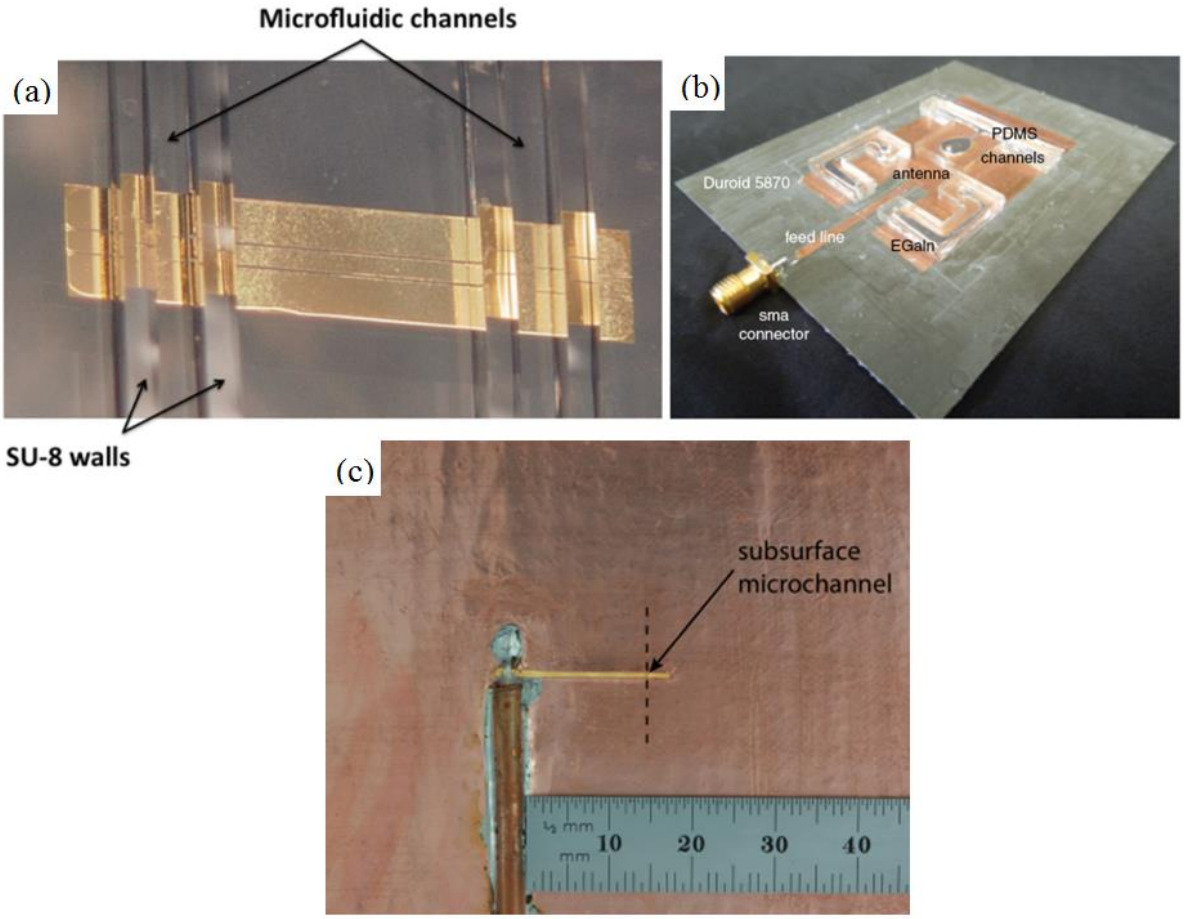

Figure 2.6. Various approaches to RF device reconfiguration through the use of fluidic networks. (a) A phase reconfigurable CPW with open channels formed by sidewalls of SU-8 photoresist. [22] (b) A frequency reconfigurable slot antenna enabled through the movement of EGaIn in a PDMS fluidic network. [24] (c) A frequency reconfigurable slot antenna with a single subsurface microchannel contained within a composite layer. [25]

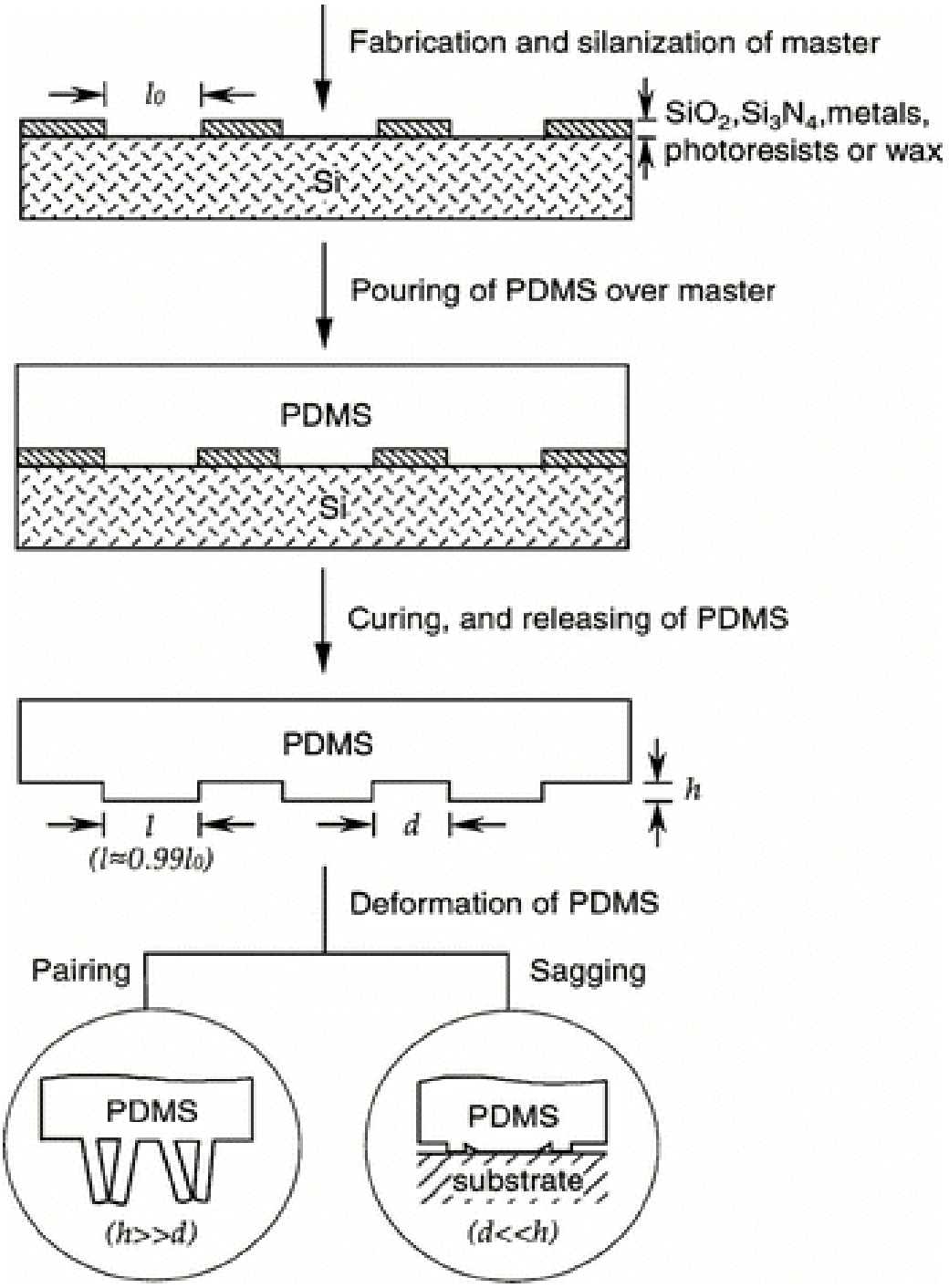

Figure 2.7. Process flow diagram of soft lithography for a PDMS elastomer. If this PDMS layer were to be bonded to another flat PDMS surface, rectangular microchannels of width *d* and height *h* would be formed. Figure adapted from [31]

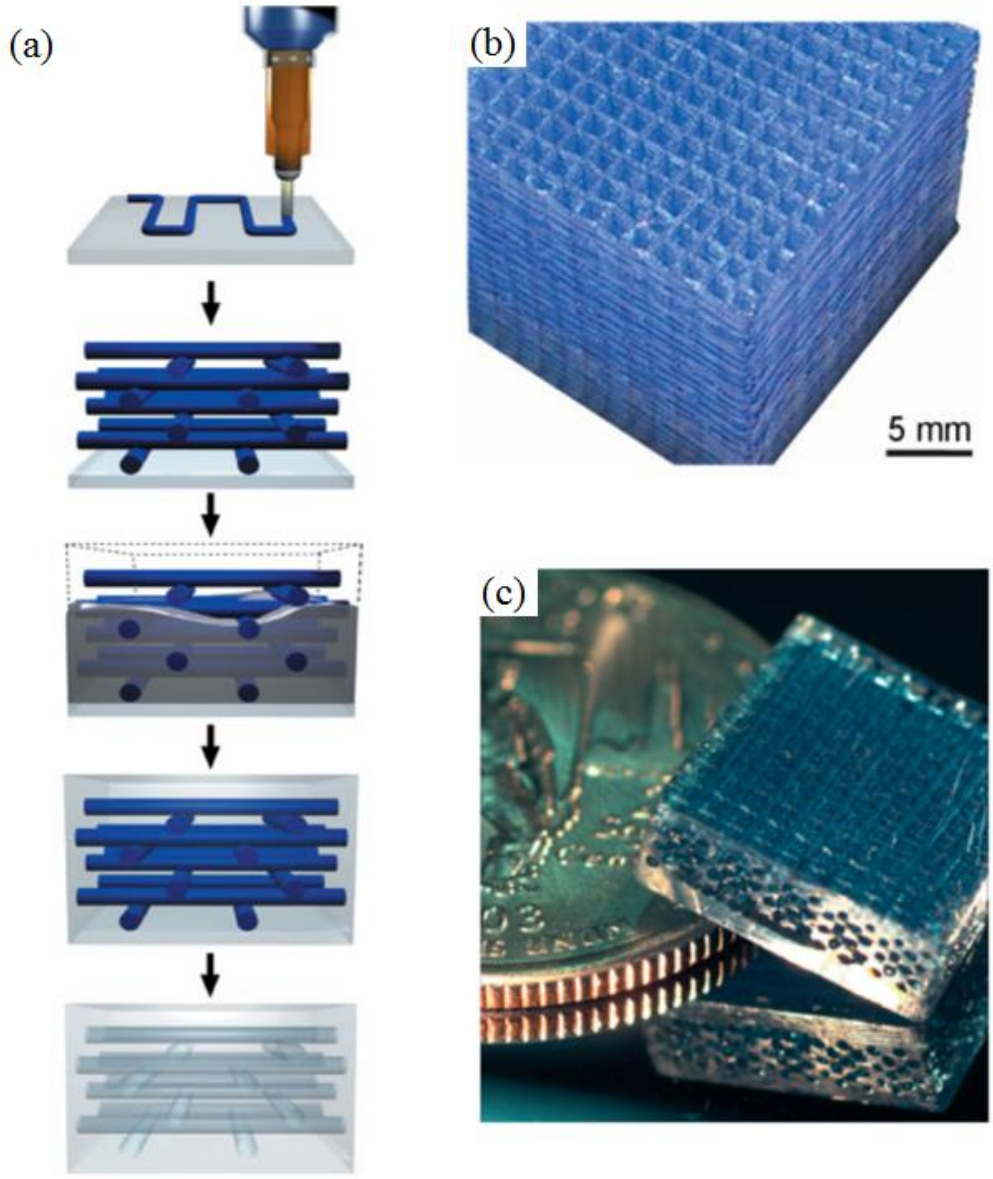

Figure 2.8. (a) Process flow diagram for the formation of microvascular networks using a sacrificial 3D printed viscoelastic ink. [48] (b) Optical image of a 3D printed scaffold network of sacrificial ink. [48] (c) Optical image of a sacrificial network which has been cast in epoxy and subsequently removed to form a microvascular network; a dime is included in the image for size comparison. [49]

CHAPTER 3

MATERIALS AND METHODS

3.1 Introduction

The materials selection and evaluation process covered in this chapter is focused on integration and effectiveness of microfluidic systems in high frequency PCB technology. The process starts with materials which are already commonly used in RF signal device applications and continues on to explore additional materials for forming compatible microvascular structures. Robust mechanical properties, dielectric behavior, thermal stability, and conformability are all important factors when selecting materials for microfluidic systems. Since the vascular network needs to physically contact the RF signal devices at select locations, bonding between the signal devices and the vascular matrix material is investigated. Finally conductivity experiments characterizing the ability of fluid contained in the vasculature to create an ohmic contact with signal devices are performed.

3.2 Microvascular Matrix Material Selection

3.2.1 Substrate Materials

A common material combination for PCB-integrated RF signal devices consists of copper cladding on a continuous fiber-reinforced polymer matrix composite with low electrical permittivity properties and high thermal stability. This thesis utilizes two similar commercially available glass-fiber reinforced polytetrafluoroethylene (PTFE) composite laminates with electrodeposited copper cladding (Duroid 6010 and 5880, Rogers Corp.). Material properties for 6010 and 5880 are presented in Tables 3.1 and 3.2 respectively. The degradation temperature for both systems is 500 °C by TGA mainly due to the high thermal stability of the PTFE polymer

matrix. Both of these materials allow for high power signal devices, which reach temperatures of 300 °C during operation. One or both sides of each laminate system is uniformly clad in 35 μm of electrodeposited copper with a root-mean-square roughness of 0.5 μm for the copper surface and 2.1 μm for the dielectric surface. Test patterns and signal devices are formed through selective milling of the coppery layer by the commercial supplier (Rogers Corp), exposing the underlying PTFE substrate (Figure 3.1).

3.2.2 Candidate Matrix Materials

Matrix materials for vascularized RF devices must be stable at high temperatures, adhere to PTFE/copper substrates, have a low dielectric constant, and have a low electrical loss tangent in the target RF range. Based on an initial screening, two different thermosetting polymers were investigated. Spurr resin (Sigma-Aldrich) was selected due to its low viscosity, mild processing conditions, and use in electron microscopy.[10] RenInfusion 8605 (Huntsman Corporation) was selected due to its relatively high thermal stability, superior mechanical properties, and use in fiber-reinforced composite systems.

Spurr Resin (Spurr) is a 4-part thermoset system consisting of a cycloaliphatic epoxy resin, an epoxy flexibilizer, an anhydride hardener, and a primary alcohol based accelerator, with respective chemical structures shown in Figure 3.2. Spurr possesses a mixed viscosity of 70 centipoise (cP) and has a manufacturer's recommended cure schedule of 8 hours at 70°C, although the gel time at room temperature (RT) is about 3 days.

RenInfusion 8605 (8605) is a three-part thermoset systems consisting of a bisphenol A epoxy resin pre-mixed with butanedioldiglycidyl ether, and a 2,2'-Dimethyl-4,4'methylenebis(cyclohexylamine) hardener, with respective chemical structures shown in

Figure 3.2. 8605 possesses a mixed viscosity of 700 cP and has a manufacturer's recommended cure schedule of 24 hours at RT followed by 2 hours at 121°C then 3 hours at 177°C.

3.2.3 Sacrificial Ink

Vascularized networks were formed through the deposition and subsequent removal of a sacrificial microcrystalline wax ink as described by Therriault *et al*. [7] The ink consisted of 60 w/wt% microcrystalline wax (SP-19, Strahl &Pitsch, Inc.) and 40 w/wt% heavy mineral oil (Fischer Scientific). The ink was prepared through mixing the two components in a beaker for 10 minutes at 100°C. The molten mixed ink was then placed into 3 mL syringe barrels and rapidly cooled to ambient temperature. Syringe tips of various diameters were then placed on the barrels for deposition. Sacrificial ink extrusion through the syringe tips was controlled using air pressure. Network architectures were written in computer numeric control G code. The corresponding movement, speed, and extrusion rate of the ink containing syringes was carried out by an air-bearing robocaster (custom build, Aerotech).

3.2.4 Network Formation and Thermal Stability

Simple straight lines of the sacrificial ink were printed on flat substrates, then embedded in freshly mixed and degassed candidate systems (8605 and Spurr) to investigate vascular network formation. Each system was allowed to gel at RT (1 day for 8605, 3 days for Spurr) then subjected to the manufacturer's recommended cure schedule. Upon completion of the cure cycle, network formation was confirmed by cross-sectional scanning electron microscopy (Philips XL30 ESEM-FEG, FEI Company) and light microscopy (DMR, Leica Microsystems). No changes in the sacrificial ink were observed in Spurr Resin. In contrast, some interaction occurred between the wax and the 8605 resin, causing large (1-2mm diameter) bubbles to form

(Figure 3.3) during the manufacturer's recommended cure cycle. A modified lower temperature cure cycle was adopted to reduce degradation and diffusion of the wax, which consisted of 24 hours at RT, then 2 hours at 50 °C, and finally 8 hours at 121 °C. The wax lines survived this cure schedule without diffusion or cracking of the matrix material (Figure 3.4).

The degree of cure of the 8605 was investigated using a dynamic scanning calorimeter (Q20-2272 DSC, TA Instruments). A baseline curve was established using a heat-cool-heat program from 0 °C to 300 °C at a ramp rate of 5 °C/min. Samples were uncured at the start of the program (freshly mixed), and 100% cured by the start of the second heat cycle. The integrated area between these two curves establishes the complete heat of reaction. By comparing the residual heat of reaction from partially cured samples to the full heat of reaction, the degree of cure was obtained by

$$H_R = \int_0^T \left(\frac{dQ}{dT}\right) dT \tag{3.1}$$

$$H = \int_0^T \left(\frac{dQ}{dT}\right) dT \tag{3.2}$$

$$\alpha = 1 - \frac{H}{H_R}, \tag{3.3}$$

where dQ/dT is the rate of heat generation, H_R is the full heat of reaction, H is the residual heat of reaction after some partial cure, and α is the full degree of cure. The manufacturer's recommended cure schedule resulted in a 99% degree of cure, while the modified cure schedule resulted in a 94% degree of cure. By comparison, the Spurr system achieved a 97% degree of cure following the manufacturer's recommended cure cycle.

The T_g of each resin system was measured using DSC as well. For Spurr and 8605 cured with the manufacturers' recommended cure cycles the Tg was 55 °C and 152 °C, respectively. The modified cure schedule of 8605 resulted in a lower Tg at 130 °C. Hence, 8605 has superior thermal stability over the Spurr resin system.

3.2.5 Dielectric Properties

Dielectric properties of both Spurr and 8605 were investigated in collaboration with Kurt Schab and Prof. Jennifer Bernhard in the ECE department at UIUC. Parallel-plate capacitor methods for measuring dielectric properties are limited to below 2 MHz frequency. To properly characterize the dielectric properties at radio frequencies, we used a modified NRW (Nicolson, Ross, and Weir) method.[11] A 2mm thick rectangular sample was placed in a 2-port square waveguide transmission line. The line was filled with air and calibrated using samples with a known permittivity and loss tangent (Figure 3.5).[12] An RF signal generator was used to pass test signals at various frequencies through the transmission line, with transmission and reflection parameters being directly measured by a RF signal analyzer (Figure 3.5). The direct measurements were then used to derive the scattering parameters which in turn yielded the complex permittivity and permeability.[12] The real parts of the complex permittivity and permeability values were normalized to those of vacuum and resulted in the relative permittivity as well as the loss tangent of the material under investigation.[13]

Dielectric testing results for Spurr and 8605 are summarized in Figures 3.6 and Figure 3.7. Over the frequency range of interest (8.5 – 10 GHz) both samples had desirable permittivity and loss characteristics, with average values for Spurr and 8605 of 2.7 and 2.9 for relative permittivity and loss tangent values of 0.03 and 0.04 respectively. While Spurr slightly

outperformed 8605, the dielectric properties for both epoxy systems were within the acceptable range for RF signal applications.

3.3 Bonding of Vascularized Epoxy to RF Devices

The planar RF devices consisted of PTFE composite substrates with a patterned electrodeposited copper layer which was used for the active device. Debonding from both the PTFE composite and copper surfaces occurred upon initial fabrication of microvascular test-lines in 8605, which was directly cast and cured on co-planar waveguides (Figure 3.8).

PTFE is chemically inert and difficult to bond to. Plasma etching has previously been used to improve adhesive bond strength between PTFE and various polymers.[14,15] Electrochemical reduction reactions of the PTFE surface resulted in carbonized surface structures (~ 1 μm depth).[16-18] Ammonia was required for this treatment and strong increase in the surface electrical conductivity was observed. In the current work, the reduction reaction was accomplished, without the use of ammonia or modification of surface electrical properties, using a new commercially available active salt based reduction agent, sodium naphthalene (Figure 3.9). This treatment replaces the fluorine atoms on the polymer backbone with hydroxyl, carbonyl, and carboxyl groups (Fluoroetch Safety Solvent, Acton Technologies). The PTFE composite substrates were immersed in the etchant solution for approximately 10 minutes at 35°C, after which the substrates were rinsed off using ethanol. Figure 3.9 contains images of the etched and unetched surfaces. Contact angle measurements confirmed a change in surface energy.

An etching-based approach was also attempted to improve the adhesion of the vascularized epoxy matrix to the copper surface. The copper surface was etched with a 50-50

wt% mixture of Iron (III) Chloride (Sigma-Aldrich) and ethanol, applied for no more than 5 seconds, and then rinsed off with pure ethanol. Etching alone did not appreciably increase the surface energy of the copper surface, as shown by the contact angle measurements in Figure 3.10 (and confirmed by continued debonding at the copper-epoxy interface in test-line samples). Interfacial bonding was improved by a silane treatment applied to the copper surface after etching.[19] The particular silane selected in this work for the copper-epoxy interface was (3-glycidyloxypropyl)trimethoxysilane, due to the dangling epoxide functional group which readily bonded with amine and anhydride groups present in the hardener portions of 8605 and Spurr. This treatment was applied by immersing the freshly etched copper surfaces in an aqueous solution at volume ratio of 1:100 (silane:water) for approximately 5 minutes. The silane solution was then gently removed from the copper surface, and the specimen was allowed to air dry at room temperature for a minimum of 24 hours before application of the epoxy. Contact angle measurements confirmed that application of the silane following etching increased the surface energy and interfacial debonding was not observed in samples which underwent silane treatment (Figure 3.10).

3.4 Conductive Fluid Selection and Ohmic Contact

The conductive fluid within the vascularized network must form a direct ohmic contact with the patterned copper layer. A common fluid discussed in the literature for similar reconfigurable RF applications is eutectic gallium-indium (EGaIn), a metallic liquid with a resistivity of $29.4*10^{-6}$ Ω-cm and bulk viscosity of 1.99 cP.[20-25] These properties allow EGaIn to form ohmic contact with other metallic conductors (copper) and easily flow through small vascular channels.

Sacrificial ink lines 300-500 μm in diameter were printed on a surface treated coplanar waveguide perpendicular to the signal and ground traces (Figure 3.9) These lines were then cast in epoxy (8605) and subsequently vascularized by removing the sacrificial ink using heat and vacuum after the epoxy cured. Syringe tips were inserted into the channel openings at either end and EGaIn was injected into the channels. The resistance between two copper traces with a 1.13mm gap was measured using a standard two-point probe method and a digital multimeter (USB-4065 DMM, National Instruments) before and after injection over multiple cycles. Representative results are shown in Figure 3.9. Control tests were also run where the resistance was measured over a single copper trace. Probe spacing for EGaIn contact and control resistance test were kept equal. EGaIn channel contact tests had an average resistance of 0.08 Ω while control tests had an average setup resistance of 0.078 Ω. The 0.002 Ω difference in resistance was attributed to the 1.13 mm EGaIn channel spanning distance and contact with copper. When the channel was not filled with EGaIn, resistance between the two separated copper traces was not measurable by the DMM, which could not measure resistances over 100 MΩ.

These results confirm that EGaIn is a promising candidate fluid for the reconfiguration of conductive devices. The surface treatments used to increase the adhesion strength of both copper and PTFE to epoxy did not prevent EGaIn from forming an ohmic contact and did not allow for parasitic currents to flow through the carbonized PTFE surface when no additional conductive pathway (such as EGaIn) was present. The results displayed in Figure 3.11 show 3 full on-off cycles, beyond which switching was not achievable by removing the EGaIn from the channel. This limited number of switching cycles was observed in all tests and was attributed to an oxide layer formation on the channel walls upon EGaIn removal, which has been reported previously.[25]

3.5 Conclusions

A simple vascular network was successfully integrated with a commercial PTFE RF substrate. Two candidate epoxy-based thermosets, 8605 and Spurr Resin, were investigated for thermal stability, ability to conform to sacrificial printed material, and dielectric properties. While Spurr Resin had good conformation to sacrificial structures and desirable dielectric properties, the low thermal stability limits its use in high-power applications. 8605 had good conformation to printed wax structures and desirable dielectric properties, as well as a relatively high thermal stability. Debonding from patterned RF substrates was observed for both systems. An etching treatment was applied to increase the adhesive strength of the epoxy-PTFE laminate interface. A multi-stage etching and silane treatment was used to increase adhesive strength of the epoxy-copper interface as well. EGaIn was introduced into the vascular channels to make ohmic contact with the patterned copper traces. Line resistance was successfully switched between 0.08Ω and > 100 MΩ (insulating) by sequential flow and removal of EGaIn from the channels.

3.6 References

1. G. Marconi, *Wireless Telegraphic Communication: Nobel Lecture, 11 December 1909*. Nobel Lectures, Physics 1901–1921. Amsterdam: Elsevier Publishing Company, 1967: 196–222. p. 206.
2. P.K. Bondyopadhyay, *Guglielmo Marconi - The father of long distance radio communication - An engineer's tribute*. 25th European Microwave Conference, 1995, 2, p. 879-885.
3. F.Sarvar, N. J. Poole, and P. A. Witting, *PCB glass-fibre laminates: Thermal conductivity measurements and their effect on simulation*. Journal of Electronic Materials, 1990, 19, p.1345–1350.
4. Z. N. Low, J. H. Cheong, and C. L. Law, *Low-Cost PCB Antenna for UWB Applications.* IEEE Antennas and Wireless Propagation Letters, 2005, 4, p. 237-239.
5. L. Lizzi, F. Viani, and A. Massa, *Dual-Band Spline-Shaped PCB Antenna for Wi-Fi Applications*. IEEE Antennas and Wireless Propagation Letters, 2009, 8, p. 6d16-619.
6. D. Therriault, S. R. White, and J. A. Lewis, *Chaotic mixing in three-dimensional microvascular networks fabricated by direct-write assembly.* Nature Materials, 2003, 2, p. 265-272.
7. D. Therriault, S. R. White, and J. A. Lewis, *Rheological behavior of fugitive organic inks for direct-write assembly.* Applied Rheology, 2007, 17, p. 10112-10120.
8. J. A. Lewis, *Direct ink writing of 3D functional materials.* Advanced Functional Materials, 2006, 16, p. 2193-2204.
9. A. J. King, J. F. Patrick, N. R. Sottos, S. R. White, G. H. Huff, and J. T. Bernhard, *Microfluidically Switched Frequency-Reconfigurable Slot Antennas*. IEEE Antennas and Wireless Propagation Letters, 2013, 12, p. 828-831.
10. A. R. Spurr, *A low-viscosity epoxy resin embedding medium for electron microscopy*. Journal of Ultrastructure Research, 1969, 26, p. 31-43.
11. A. M. Nicolson and G. F. Ross, *Automatic measurement of complex dielectric constant and permeability at microwave frequencies*. Proceedings of the IEEE, 1974, 62, p. 33–36.
12. K. Schab, *Electromangetic Characterization Of Carbon Nanotubes And Their Composites For Microwave Sensing Applications*, Master's of Science in Electrical and Computer Engineering Thesis, University of Illinois at Urbana-Champaign, 2013.
13. *Permittivity and loss tangent of materials (Two Fluid Cell Method).* Institute of Printed Circuits, Dec. 1987, Northbrook, IL.
14. *Teflon PTFE Properties Handbook.* E. I. du Pont de Nemours and Company, Wilmington, DE. retrieved Dec. 2013.
15. S. L. Kaplan, E. S. Lopata, and J. Smith, *Plasma Processes and Adhesive Bonding of Polytetrafluroethylene.* Surface and Interface Analysis, 1993, 20, p. 331-336.
16. D. J. Barker, D. M. Brewis, R. H. Dahm, J. D. Gribbin, and L. R. J. Hoy, *Surface Pretreatments of Polytetrafluoroethylene*. The Journal of Adhesion, 1981, 13, p. 67-76.
17. A. Yasuda and W. Mizutani, *Carbon nanostructure formation by a reduction of PTFE.* Thin Solid Films, 2003, 438, p. 313-316.

18. C. Combellas, F. Kanoufi, D. Mazouza, A. Thiébault, P. Bertrand, and N. Médard, *Surface modification of halogenated polymers. 4. Functionalisation of poly(tetrafluoroethylene) surfaces by diazonium salts.* Polymer, 2003, 44 p. 19-24.
19. S. Mishra and J. J. Weimer, *Comparative analysis of trimethylmethoxysilane and trimethylchlorosilane bonding on polished copper surfaces.* Journal of Vacuum Science & Technology A, 1995, 13, p. 1281-1285.
20. J. So, J. Thelen, A. Qusba, G. J. Hayes, G. Lazzi, and M. D. Dickey, *Reversibly deformable and Mechanically Tunable Fluidic Antennas*. Advanced Functional Materials, 2009, 19, p. 3632-3637.
21. M. Kubo, X. Li, C. Kim, M. Hashimoto, B. J. Wiley, D. Ham, and G. M. Whitesides, *Stretchable Microfluidic Radiofrequency Antennas.* Advanced Materials, 2010, 22, p. 2749-2752.
22. G. J. Hayes, J. So, A. Qusba, M. D. Dickey, and G. Lazzi, *Flexible Liquid Metal Alloy (EGaIn) Microstrip Patch Antenna*. IEEE Transactions on Antennas and Propagation, 2012, 60, p. 2151-2156.
23. M. Kelley, C. Koo, H. Mcquilken, B. Lawrence, S. Li, A. Han, and G. H. Huff, *Frequency reconfigurable patch antenna using liquid metal as switching mechanism.* Electronics Letters, 2013, p. 1370-1371.
24. A. J. King, J. F. Patrick, N. R. Sottos, S. R. White, G. H. Huff, and J. T. Bernhard, *Microfluidically Switched Frequency-Reconfigurable Slot Antennas*. IEEE Antennas and Wireless Propagation Letters, 2013, 12, p. 828-831.
25. M. D. Dickey, R. C. Chiechi, R. J. Larsen, E. A. Weiss, D. A. Weitz, and G. M. Whitesides, *Eutectic Gallium-Indium (EGaIn): A Liquid Metal Alloy for the Formation of Stable Structures in Microchannels at Room Temperature.* Advanced Functional Materials, 2008, 18, p. 1097-1104.
26. *RT/duroid® 6006/6010LM High Frequency Laminates Data Sheet 1.6*. Rogers Corporation Advanced Circuit Materials Division, Jun. 2014, Chandler, AZ.
27. *RT/duroid® 5870 /5880 High Frequency Laminates*. Rogers Corporation Advanced Circuit Materials Division, Jun. 2014, Chandler, AZ.

3.7 Tables

Table 3.1. Material properties of Duroid 6010, a fiber reinforced PTFE composite laminate for RF circuit applications. [27]

Rogers Corp. RT/Duroid 6010 Laminate Material Properties					
Property	**Typical Value**	**Direction**	**Units**	**Condition**	**Test Method**
Dielectric Constant, ε_r	10.2 ±0.25	Z	Relative to vacuum	10 GHz 23°C	IPC-TM-650 2.5.5.5 Clamped stripline
Dissipation Factor, tanδ	0.0023	Z		10 GHz/A	IPC-TM-650 2.5.5.5
Surface Resistivity	$5x10^6$	-	Mohm	1 A	IPC 2.5.17.1
Volume Resistivity	$5x10^5$	-	Mohm•cm	1 A	IPC 2.5.17.1
Young's Modulus	931	X	MPa	0.1/min. strain rate	ASTM D638
Young's Modulus	559	Y	MPa	0.1/min. strain rate	ASTM D638
Flexural Modulus	4364	X	MPa		ASTM D790
ultimate stress	17	X	MPa	0.1/min. strain rate	ASTM D638
ultimate stress	13	Y	MPa	0.1/min. strain rate	ASTM D638
Deformation under load	0.26	Z	%	24 hr/ 50°C/7MPa	ASTM D621
Moisture Absorption	0.01	-	%	D48/50°C, 0.050" (1.27mm) thick	IPC-TM-650, 2.6.2.1
Thermal Conductivity	0.86	-	W/m/°K	80°C	ASTM C518
Degradation Temp.	500	-	°C TGA	-	ASTM D3850

Table 3.2. Material properties of Duroid 5880, a fiber reinforced PTFE composite laminate for RF circuit applications.[28]

Rogers Corp. RT/Duroid 5880 Laminate Material Properties					
Property	**Typical Value**	**Direction**	**Units**	**Condition**	**Test Method**
Dielectric Constant, ε_r	2.20 ± 0.02	Z	Relative to vacuum	10 GHz 23°C	IPC-TM-650 2.5.5.5 Clamped stripline
Dissipation Factor, tanδ	0.0009	Z	-	10 GHz/A	IPC-TM-650 2.5.5.5
Surface Resistivity	$3x10^7$	-	Mohm	C96/35/90	ASTM D257
Volume Resistivity	$2x10^7$	-	Mohm•cm	C96/35/90	ASTM D257
Young's Modulus	1070	X	MPa	0.1/min. strain rate	ASTM D638
Young's Modulus	860	Y	MPa	0.1/min. strain rate	ASTM D638
ultimate stress	27	X	MPa	0.1/min. strain rate	ASTM D638
ultimate stress	29	Y	MPa	0.1/min. strain rate	ASTM D638
Moisture Absorption	0.02	-	%	D48/50°C, 0.050" (1.27mm) thick	IPC-TM-650, 2.6.2.1
Thermal Conductivity	0.20	-	W/m/°K	80°C	ASTM C518
Degradation Temp.	500	-	°C TGA	-	ASTM D3850

3.8 Figures

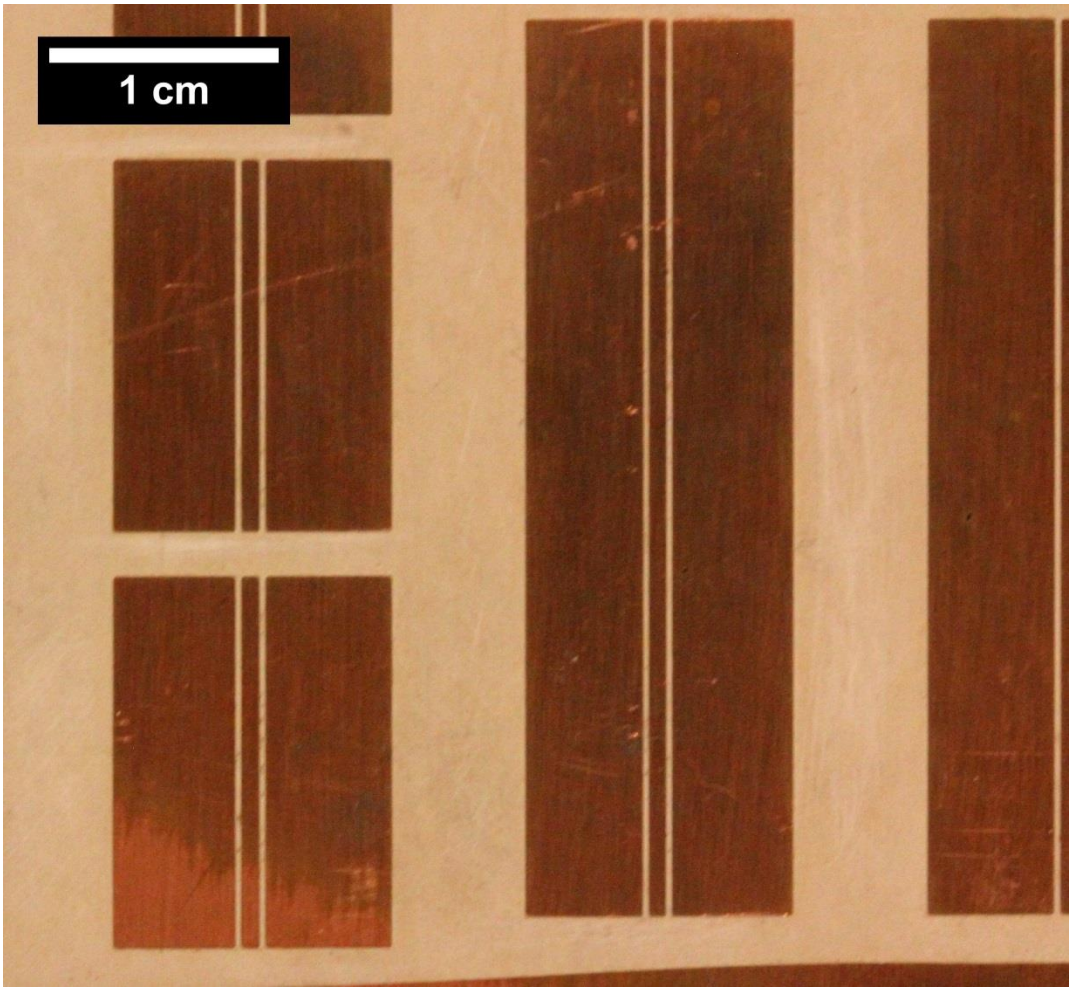

Figure 3.1. Glass fiber reinforced PTFE composite substrate with a 35 μm thick electrodeposited copper layer. The copper has been selectively milled away to form co-planar waveguides of various lengths.

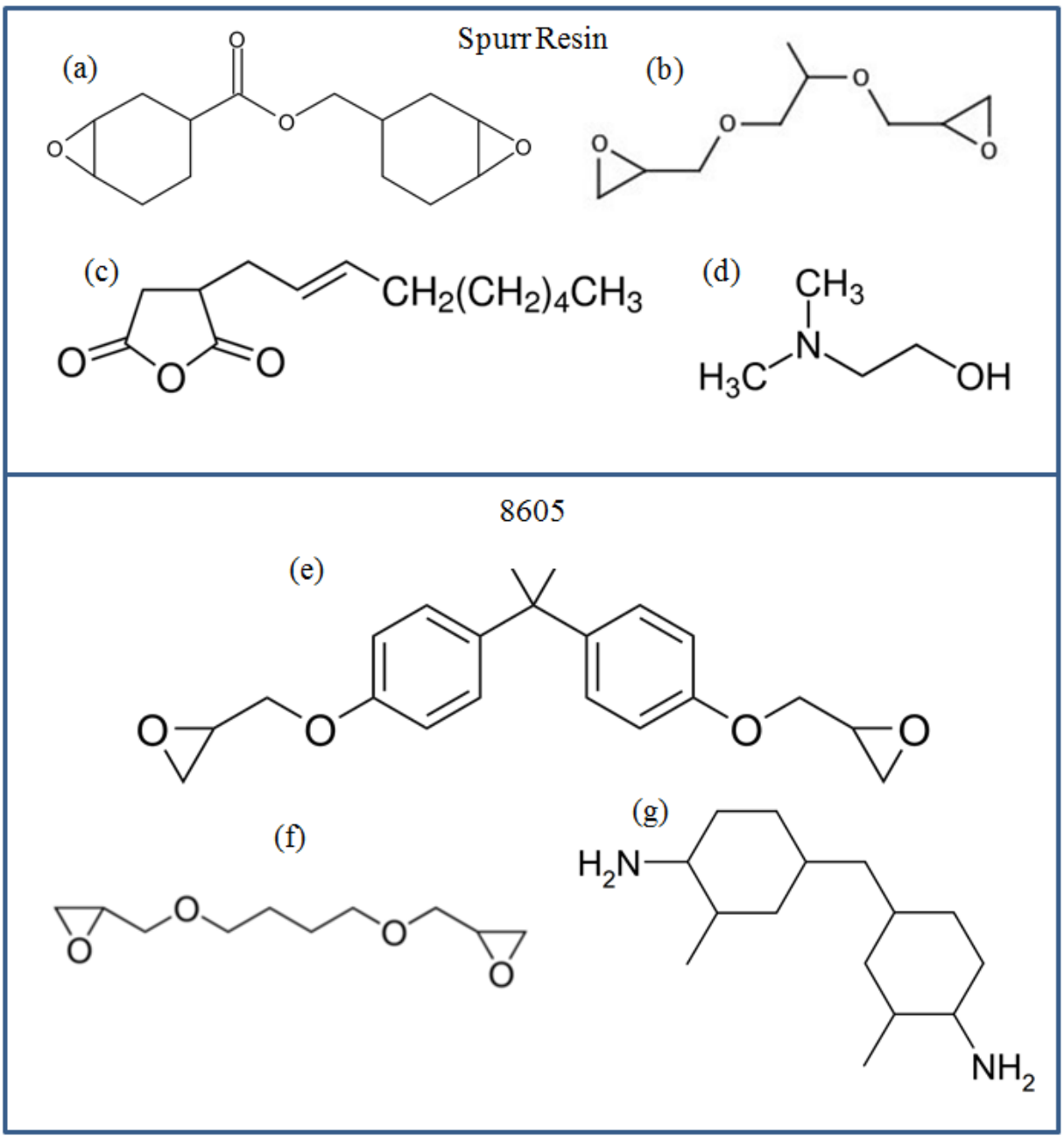

Figure 3.2. Chemical structures of constituents of Spurr Resin and 8605. Spurr consists of: (a) a cycloaliphatic epoxy monomer, (b) an epoxy flexibilizer, (c) an anhydride hardener, and (d) a primary alcohol based accelerator. 8605 consists of: (e) a Bisphenol A diglycidyl ether epoxy monomer, (f) an ether-based diluent, and (g) an amine hardener.

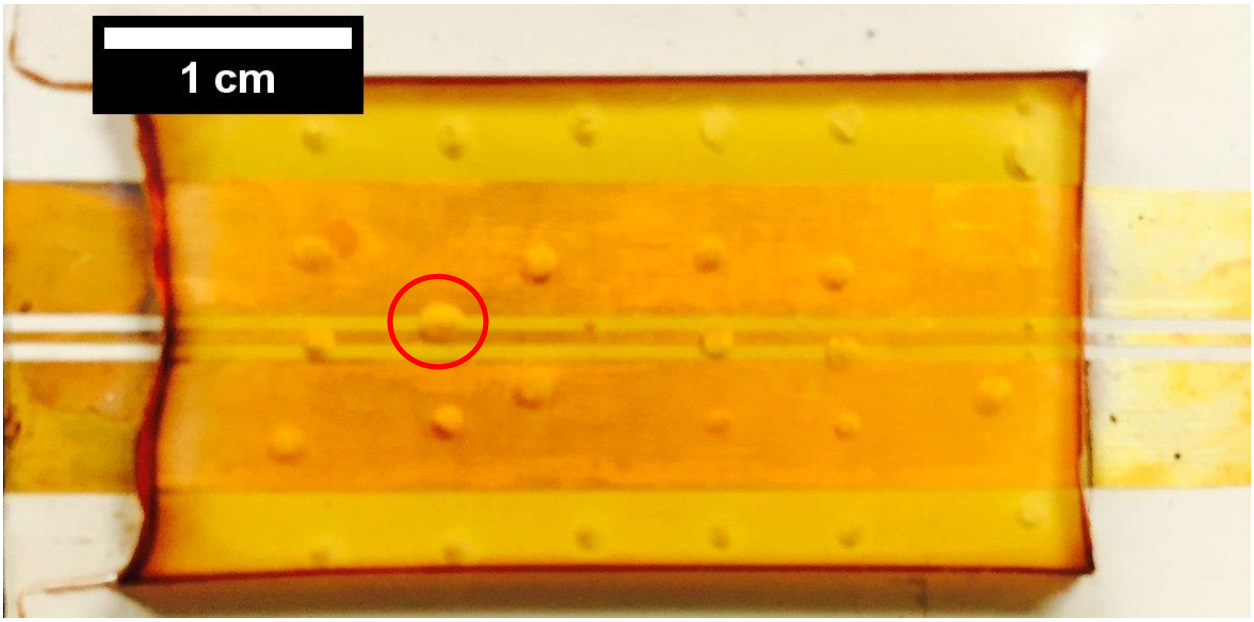

Figure 3.3. 8605 epoxy cast on top of a co-planar waveguide and then cured according to the manufacturer's recommended cure schedule. Straight sacrificial ink lines were printed directly onto the CPW before casting. Bubbles were formed during the cure cycle (as indicated by the red circle).

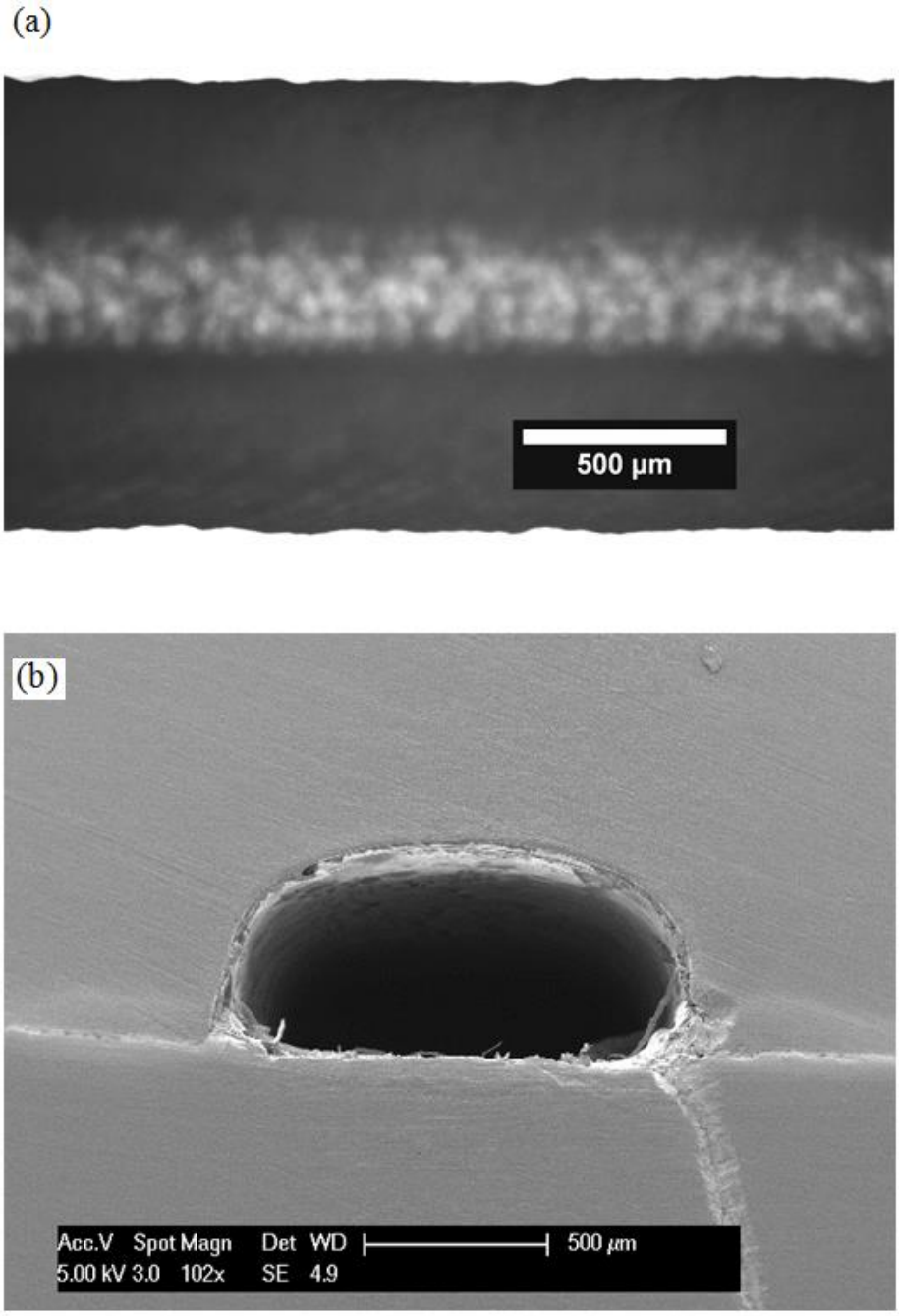

Figure 3.4. Printed sacrificial ink lines in 8605 after curing using a modified cure schedule. (a) A top-down image taken with an optical microscope at 5x magnification to confirm the line width. (b) A profile SEM image to confirm channel dimensions and conformation of the epoxy to the sacrificial ink upon casting.

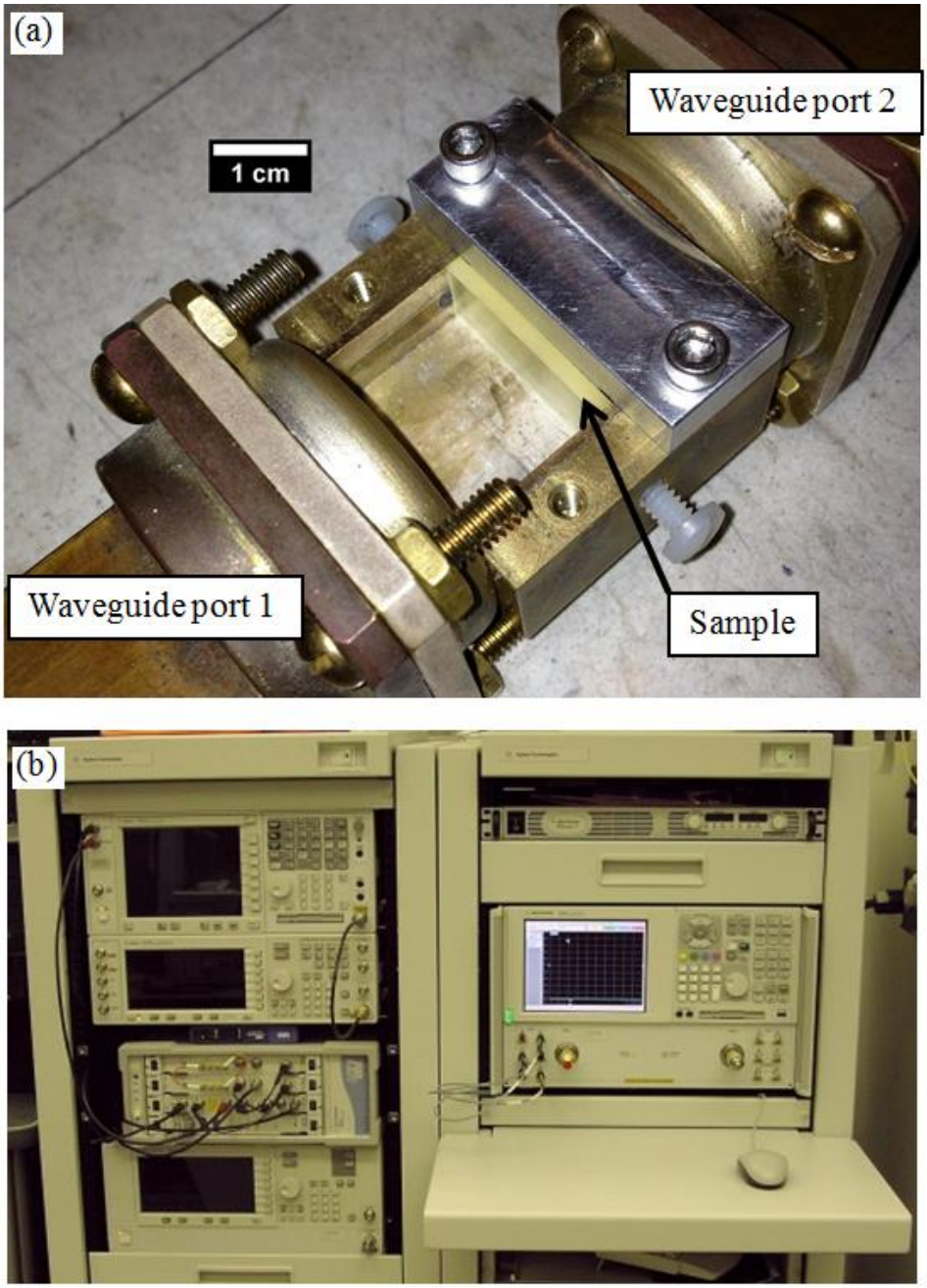

Figure 3.5. Test setup for dielectric property measurements at RF. (a) Sample housing in the rectangular waveguide with the top removed. RF test signals are passed across the sample thickness with reflection and transmission being measured at both ports. (b) Agilent test system setup with network analyzer and signal generator. Equipment use provided by Prof. Jennifer Bernhard, Electrical and Computer Engineering Department, UIUC.

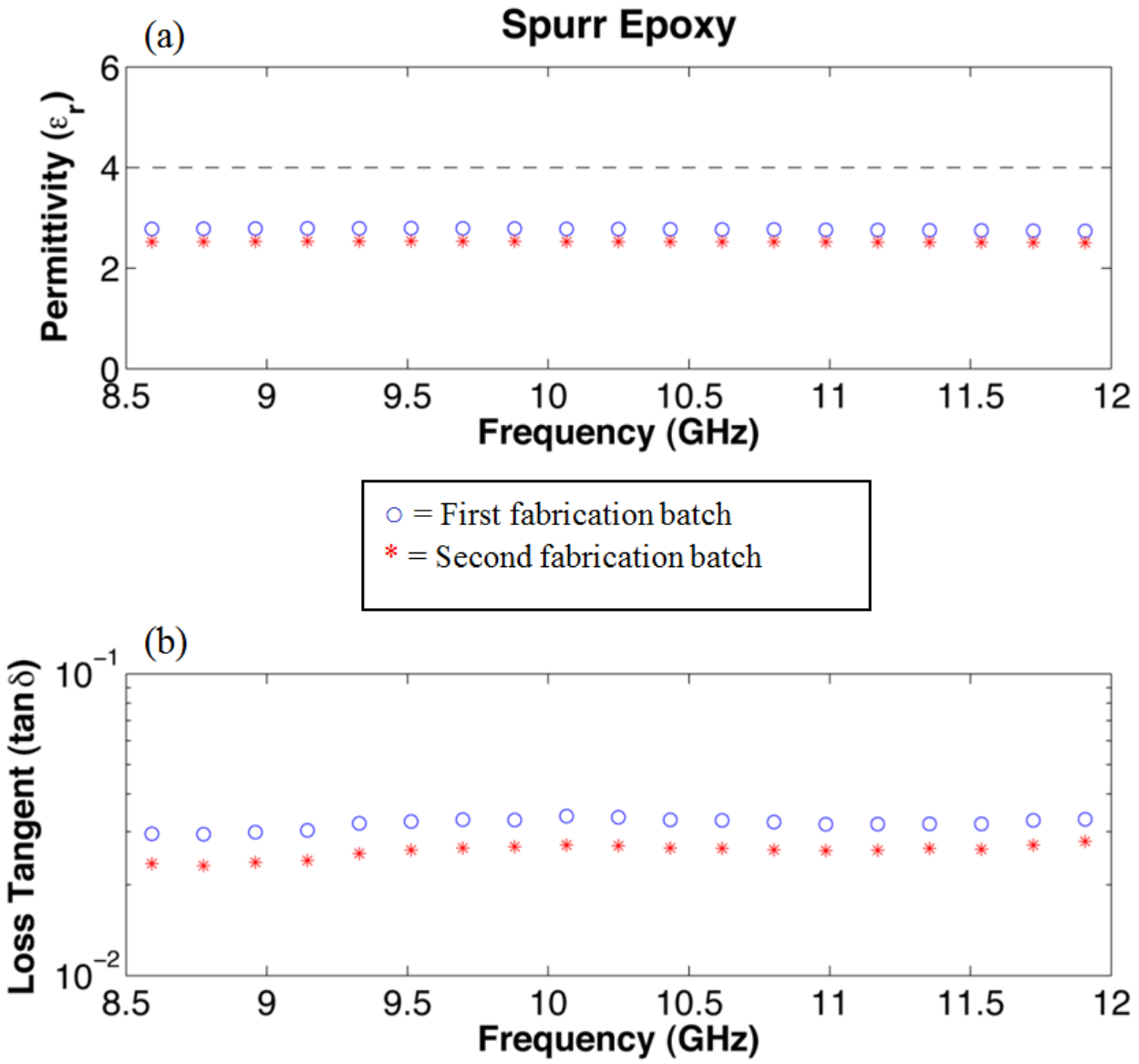

Figure 3.6. Dielectric testing results for Spurr Resin. (a) The relative permittivity from 8.5 to 12 GHz, with sample set results from two separate fabrication runs being displayed with red stars and blue circles. The dotted line is the maximum relative permittivity for acceptable losses in most applications. (b) Loss tangent data displayed vs. frequency on a logarithmic scale.

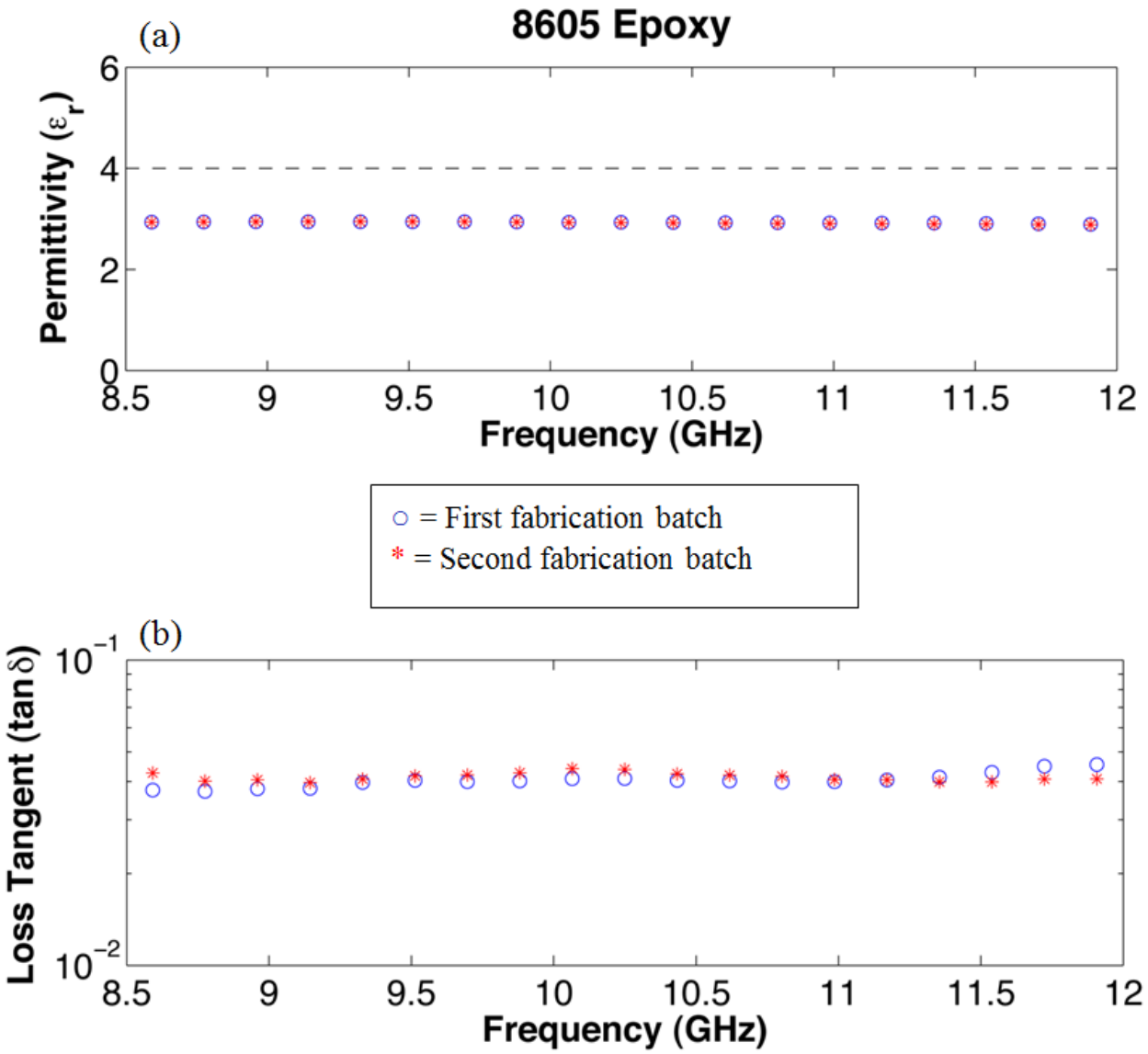

Figure 3.7. Dielectric testing results for 8605. (a) the relative permittivity from 8.5 to 12 GHz plotted in the same manner as for Spurr. (b) Loss tangent data for 8605. While 8605 has slightly higher values for both permittivity and loss tangent, they are similar to Spurr and still within acceptable ranges.

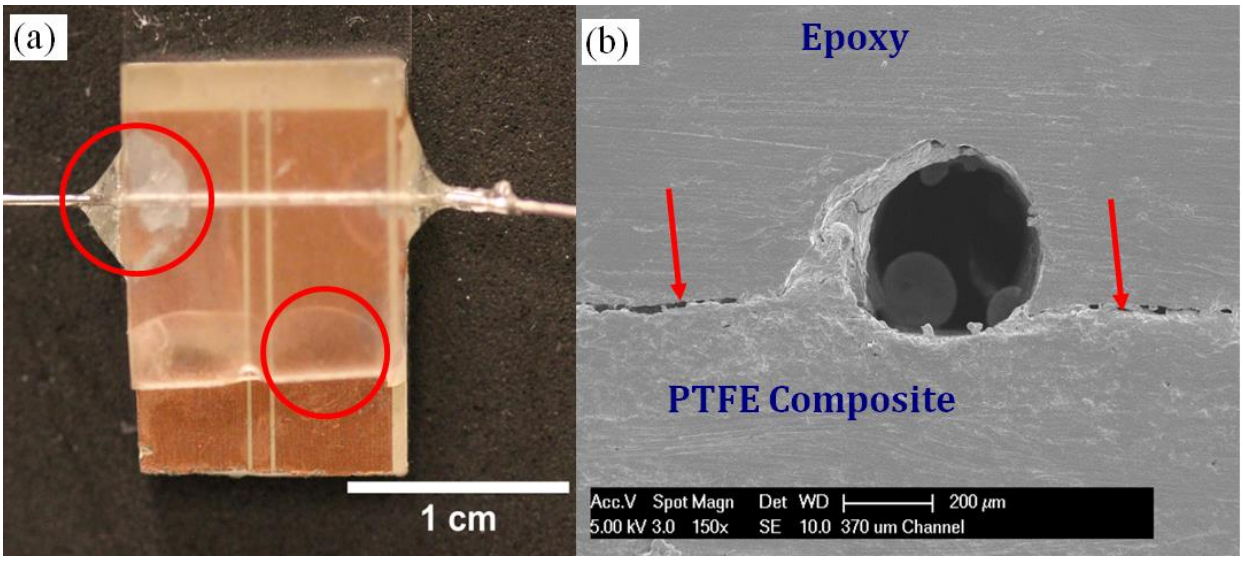

Figure 3.8. Debonding occurring between a cast epoxy layer and copper/PTFE electronic substrate. (a) Optical image of 8605 cast onto a co-planar waveguide with a single straight test channel. Large debonded regions between the epoxy and copper are highlighted. (b) An SEM image of a channel on a PTFE substrate cast in epoxy, again pointing out the debonded interface.

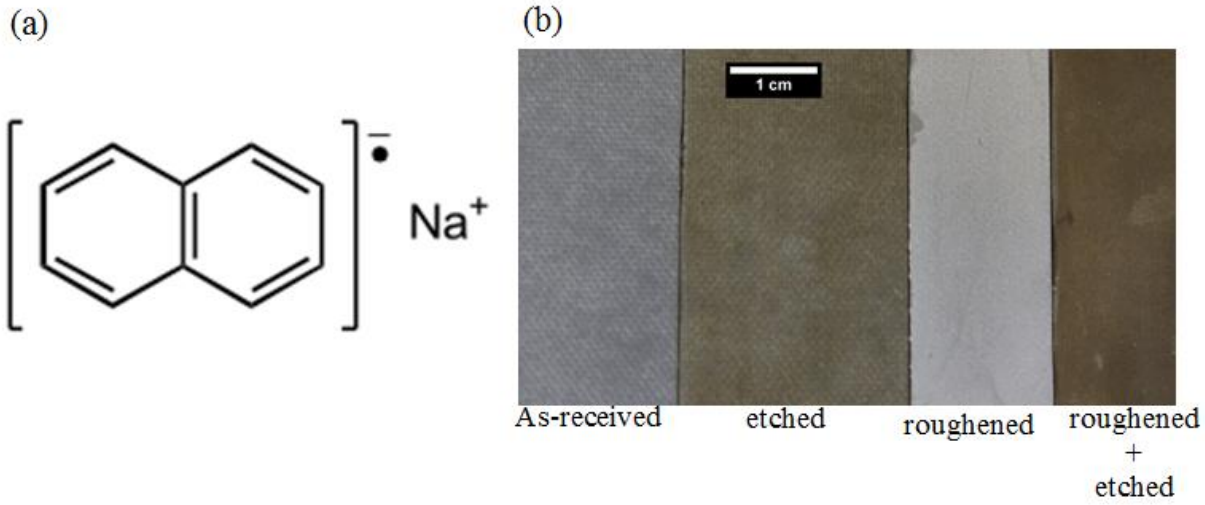

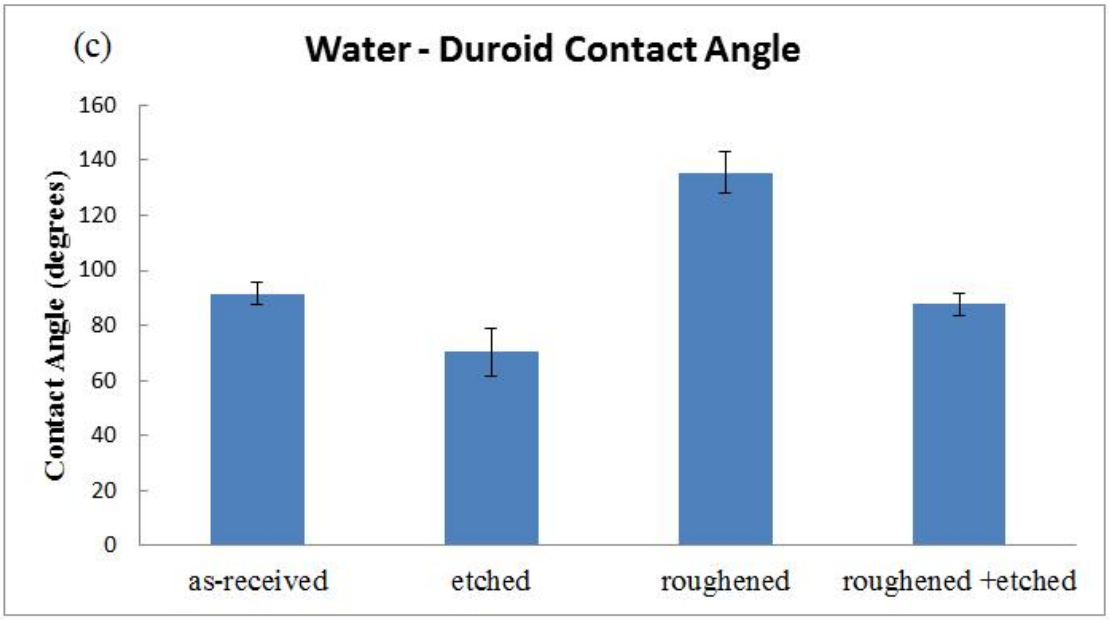

Figure 3.9. Surface treatment of PTFE laminates to increase adhesion strength with cast epoxy layer. (a) Chemical structure of sodium naphthalene, an active salt etchant for PTFE. (b) Visual comparison of Duroid 5880 (from left to right): as-received, etched, roughened, roughened and etched. Color differences indicate surface carbonization in etched samples. (c) Contact angle measurement results for the aforementioned Duroid 5880 samples, showing that etched samples have lower contact angles and thus higher surface energies.

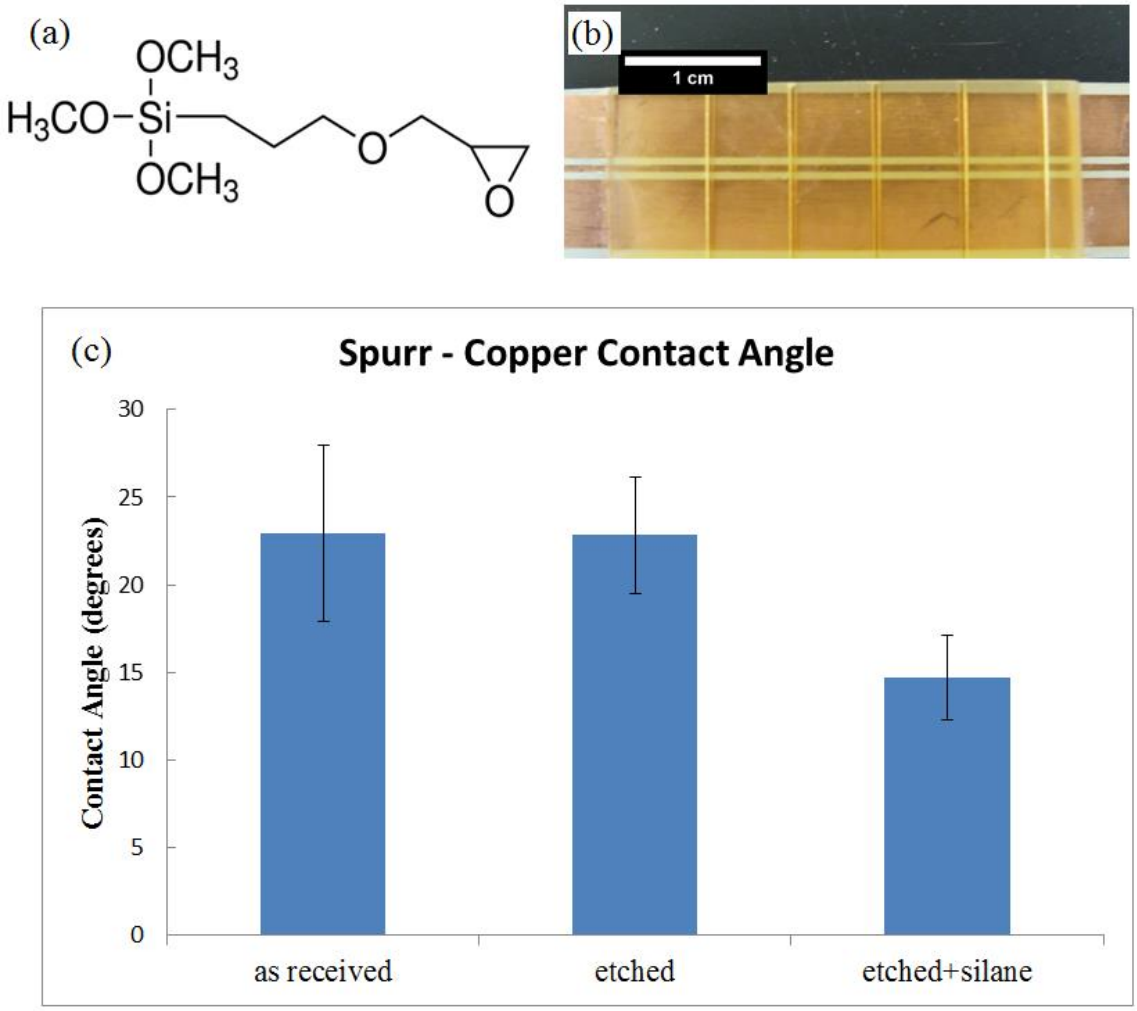

Figure 3.10. Surface treatment of patterned electrodeposited copper to increase adhesion strength with the cast epoxy layer. (a) Chemical structure of the silane with epoxide functional group applied after etching. (b) Visual confirmation that no debonding occurs between copper and epoxy in a straight channel co-planar waveguide specimen. (c) Contact angle measurements indicating that etching alone is not sufficient, but the silane treatment has a significant effect.

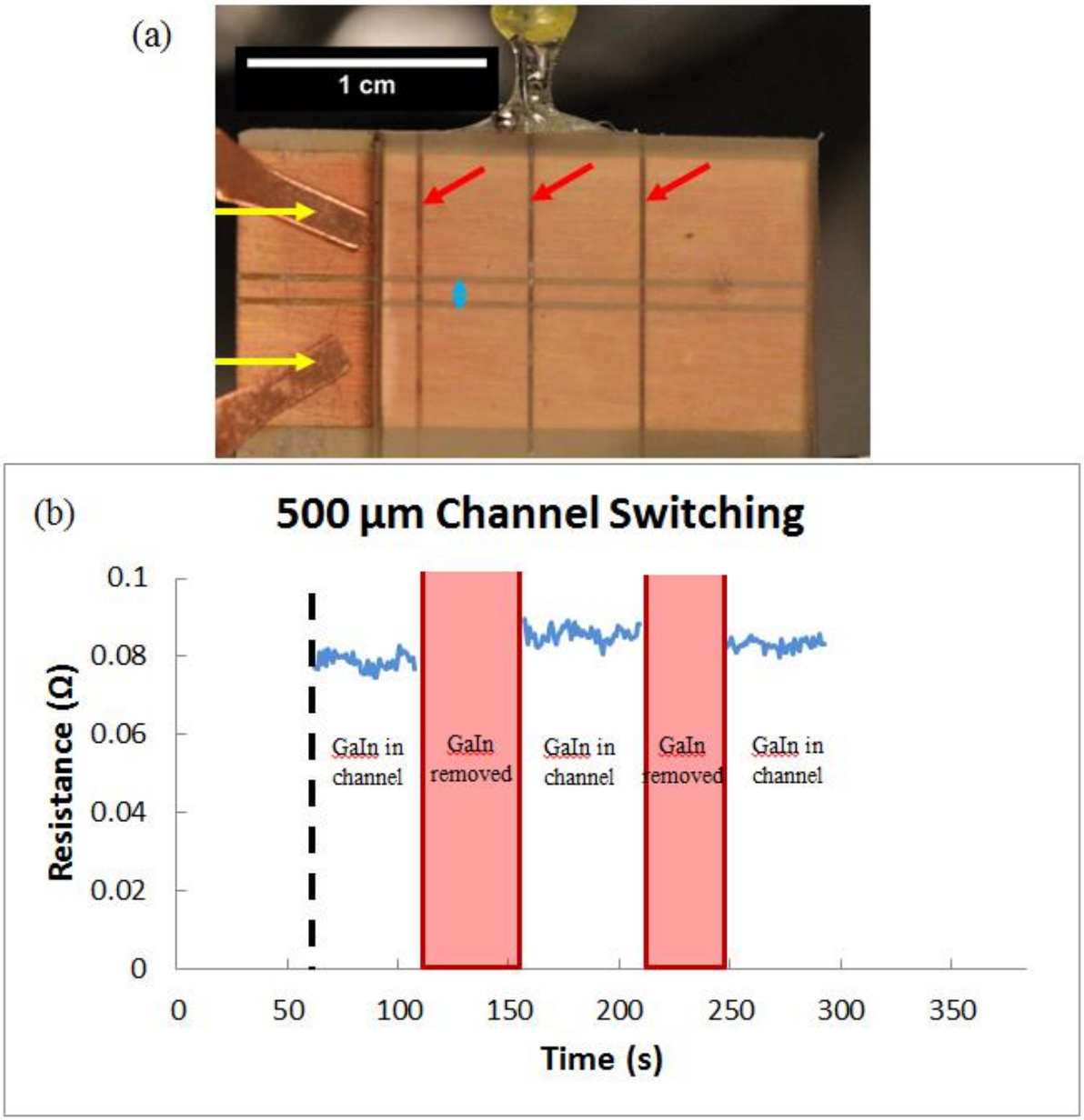

Figure 3.11. Resistance testing of EGaIn in 500 µm diameter channels on a coplanar waveguide. (a) The sample and test setup with microchannels indicated out by red arrows, the open-circuit gap by blue arrows, and the leads attached to the DMM by yellow arrows. Each microchannel was tested individually, allowing for multiple tests on a single coplanar waveguide. (b) Representative resistance measurements, indicating a low resistance when EGaIn is in the microchannels and low contact resistance between EGaIn and copper. The red regions represent resistances greater than 100 MΩ (maximum resistance detectable by equipment), demonstrating that the microchannels can facilitate repeatable switch-like behavior through injection and subsequent removal of EGaIn. Switching was not achievable after ~ 3 cycles due to the build-up of gallium oxide residue on the microchannel surface.

CHAPTER 4

PHASE RECONFIGURABLE COPLANAR WAVEGUIDES

4.1 Introduction

A coplanar waveguide (CPW) is a specific type of RF signal device originally developed by C.P. Wen at RCA Laboratories in 1969 for radar and communication applications.[1] The thin, planar nature of the design lends itself well to hybrid integrated systems, printed circuit board (PCB) technology and size-sensitive applications. A thin metallic surface strip transmission line acts as the signal transmitting portion of the CPW, while wide ground planes on either side of the signal line act as signal isolators, and finally a dielectric substrate creates a circular magnetic field polarization for nonreciprocal device applications, like radar detection (Figure 4.1). Coplanar waveguides have found use in microwave circuits, ultra-wideband bandpass filters, and tuning and impedance matching antenna assemblies, amongst other applications.[2-4]

Many recent applications of CPWs utilize phase-shifting in order to achieve circuit and signal tunability. This is usually achieved by capacitive loading of the signal line through the introduction of a conductive bridge which passes over the signal line and attaches to the ground planes on either side. Since CPWs are phase shifted in this manner, the physical dimensions of the CPW itself do not need to be altered, which allows for configurability without increasing the overall size of the system.[5] In addition to phase reconfiguration, capacitive loading of CPWs can also lead to frequency reconfiguration, which can be independently tuned through design.[6]

Phase reconfiguration of CPWs is primarily realized using microelectromechanical systems (MEMS) bridges, however this approach presents a number of problems for high-power applications. Self-actuation and latching are shown to occur in capacitive MEMS bridges above certain threshold driving powers, which are usually around 0.5W.[7] In addition, significant heat generation occurs in the MEMS bridges and signal line at high power inputs, which leads to performance degradation and unexpected transient physical effects on the thin bridges.[8] Various approaches have been taken to address both heating and self-actuation of MEMS bridges for CPW tunability including the addition of a top electrode to pull the bridge out of a latched state or various alterations to the design methodology, but these approaches can still only handle about 0.8W of power.[9,10] Another approach using dielectric blocks as the loading elements has found much more success in handling powers up to 20W and minimizing heating, but the additional control systems required for this approach interacts significantly with the CPW itself, and must be accounted for in overall design.[8]

4.2 Proof of Concept Phase Variable CPW

4.2.1 Design

A microfluidic network filled with liquid EGaIn is used to create a phase shifting CPW. Since EGaIn is circulated in and out of periodic channels, it will not experience latching or self-actuation (as MEMS devices do), does not require additional electrical control systems, is insensitive to heat, and can even remove heat with flow.[11] Using liquid EGaIn for reconfiguration allows for robust, pressure-controlled phase reconfiguration through circulation of liquid EGaIn across bridges for capacitive loading.

The initial design of this system includes ten parallel straight channels with a periodic separation, which are fabricated using the materials and methods discussed in Chapter 3. Each channel passes over the signal and ground traces, but is vertically separated from the traces through the inclusion of an insulating superstrate layer consisting of Duroid 5880 (Figure 4.2). Capacitive loading occurs when a channel is filled with EGaIn, which acts as a conductive bridge in a similar manner to previously utilized MEMs bridges. The EGaIn fluidic bridge is grounded through vertical copper vias which connect the channel to the ground planes on either side of the signal trace, as shown in Figure 4.2. Grounding the liquid metal prevents additional transmission-line modes arising from undesired reactance, which has been encountered previously.[12] Due to the discrete nature of the channel architecture, each channel in this design is individually accessed by a fluid feed system from the edges of the device, allowing for an additive phase shift based on the number of channels filled.

4.2.2 Simulation and Results

Simulation of the design architecture given in Figure 4.2 was carried out in ANSYS High Frequency Structural Simulator (HFSS) software with an input impedance of 50Ω in collaboration with J.D. Barrera and Prof. Greg Huff, ECE, Texas A&M University. Simulation results of the S21 phase and S11 magnitude as a function of frequency for both “on” (filled) and “off” (unfilled) states of a single unit cell are shown in Figure 4.3. S11 and S21scattering parameters were calculated according to Eqns. (4.1) and (4.2), where 1 denotes the input port for an antenna under investigation (the CPW in this case) and 2 denotes the output port of a receiving test antenna. The magnitude of S11 is indicative of the CPW design power efficiency, while the S21 phase difference is regarded as the phase shift between states.

$$S11 = 10 * Log \frac{Power_{returned}}{Power_{input}} \quad 4.1$$

$$S21 = 10 * Log \frac{Power_{recieved}}{Power_{input}} \quad 4.2$$

S11 simulation results show a loss of less than -15 dB (~3% power loss) for both the off (channels unfilled) and on (channels filled) states due to good impedance matching. S21 predictions show a consistent phase difference between off and on states over the frequency range of interest. Electromagnetic field simulations for all empty channels and all filled channels also confirm capacitive loading of the signal trace and little signal reactance in the grounded liquid metal bridges (Fig. 4.3). The predicted per-channel phase shift is 8.3° at 10 GHz, allowing for a total phase shift of 83° when all 10 channels are filled, providing 11 total states of operation.

Although simulation results for this proof of concept phase shifter were promising, the complicated design using vertical vias, adhesive film, a superstrate layer, individually accessed channels, and isolated volumes of EGaIn were problematic for both fabrication and practical use. One major limitation is that EGaIn leaves an oxide residue on the channel surface, which can interfere with normal operation and was not taken into account in simulations. A simpler design was developed to overcome this physical complexity.

4.3. Redesigned Serpentine Network Phase Variable CPW

4.3.1 Design

The second design iteration of the phase-shifting CPW simplified the first design by removing the adhesive layer, superstrate layer, vertical vias, and sectioning of isolated volumes of EGaIn. A single 3-dimensional channel was introduced that periodically passes over the signal

trace in a serpentine architecture (Figure 4.4). A major advantage over the previous design is the ability to access all the capacitive bridges, and thus all the reconfigurable states, through a single continuous flow path. Furthermore, the channel is continuously grounded through direct contact with the ground planes at all points, thus the superstrate layer, vertical vias, adhesive film, and EGaIn sectioning are no longer required. Discrete displacement of the fluid allows each subsequent bridge in the design to be filled, such that an additive phase shift can still be achieved. When passing over the central gap, the channel is raised such that no physical contact is made between the channel and the signal trace, which are separated by a thin layer of epoxy (Figure 4.4).

4.3.2. Fabrication

The vascular design shown in Figure 4.4 was fabricated through 3D printing of sacrificial material as described in Chapter 3. The CPW ground planes and signal line were first milled out of a continuous copper layer on Duroid 6010. The Duroid was then etched using the procedure outlined in Chapter 3, followed by etching and silane treatment of the copper traces. The vascular architecture was printed directly onto the treated surface. This ink was deposited through a 200 μm syring tip nozzle using the setup described in Chapter 3. The architecture was printed in two layers, the first was the grounded portions of the channel and the second layer formed the raised bridge region of the channel. Epoxy (8605) was cast and cured on top of the sacrificial network and planar copper traces. After curing, the entire device was cut to size and the sacrificial ink was melted and removed with application of vacuum at 100°C.

Dimensions of the copper traces were measured through optical imaging and light microscopy (Figure 4.5), while network architecture dimensions were determined by micro-computed-tomography imaging (MicroXCT-200, Xradia), shown in Figure 4.6. Resistance measurements made when the channel was filled with EGaIn confirmed a low-resistance (<0.005Ω) between the two ground planes, confirming ohmic contact between EGaIn in the channel and the ground planes. Open-circuit resistance measurements (>100 MΩ) between the ground planes and the signal trace confirmed that the channel does not physically contact the signal trace at any point.

4.3.3 RF Testing Results and Discussion

RF testing of the fabricated 8-state CPW was carried out using a high frequency signal generator, network analyzer, test antenna fixture, and anechoic chamber. Testing was carried out by the Greg Huff Lab in the Electrical and Computer Engineering Department at Texas A&M University, College Station, TX. S11 magnitude (in decibels) and S21 phase (in degrees) were both measured and used as a metric to assess efficiency and reconfigurability. Each state (1-8) was achieved by filling the respective number of subsequent unit cells with EGaIn; state 0 corresponds to no EGaIn present in the vascular network.

S11 measurements (Figure 4.7) show that all 8 states operate in a similar manner with regards to efficiency and operating frequency. These measuremnts indicate that each unit cell of the fabricated serpentine network consistently makes ohmic contact to the ground planes and passes over the signal trace without making contact. Multiple local minimums suggest that the structure may be giving rise to harmonic modes. This behavior is also seen in state 0 (network empty) suggesting that the fluidic network is not the cause of this behavior. The lack of

significant deviation of any state from state 0 demonstrates that no additional transmission line modes are arising from the vascular network and it is properly grounded. In addition, the S11 minima around 8.15 GHz are between -12 and -15 dB indicate high (94%-97%) power efficiencies for all states.

S21 measurements (Figure 4.8) reveal an average phase shift of 1.8° between subsequent states, with maximum average phase shift of 2.4° per state occurring at 12 GHz. The average total phase range (difference between state 0 and state 8) is 14.6°, with a maximum of 19.4° again occurring at 12 GHz. At the operating frequency of 8.15 GHz, the average phase shift per state is 1.5° with a total phase shift range of 11.5°.

Both S11 and S21 results differ from the simulations of the previous design for a number of reasons. First, the continuous single channel serpentine design offers less control of channel width and bridge height over the signal trace, both of which govern the phase shift. The smaller channel widths in the serpentine network (380 μm) offers less capacitive loading than the straight channel design (1.2mm), thus resulting in a smaller phase shift per unit cell. Also, the initial design uses a RF circuit board material (Duroid 5880) to separate the channels from the signal trace, while neat epoxy is used in the serpentine network CPW. Finally, the difference in operating frequency and efficiency between the straight and serpentine channel designs is attributed to the modification of the signal trace dimensions between the two designs. The straight channel design calls for a 1mm thick signal trace with 750 μm spacing from the ground planes on either side, while the serpentine network CPW had a signal trace thickness of 780 μm with 240 μm spacing. Despite the various differences between the two designs, the fabricated serpentine network design offers high radiation efficiency and multi-state phase configurability within the RF range of interest.

4.4 References

1. C. P. Wen, *Coplanar Waveguide: A Surface Strip Transmission Line Suitable for Nonreciprocal Gyromagnetic Device Applications.* IEEE Transactions on Microwave Theory and Techniques, 1969, 17, p. 1087-1090.
2. H. D. Chen, *Broadband CPW-fed square slot antennas with a widened tuning stub.* IEEE Transactions on Antennas and Propagation, 2003, 51, p. 1982-1986.
3. H. Wang, L. Zhu, and W. Menzel, *Ultra-wideband bandpass filter with hybrid microstrip/CPW structure.* IEEE Microwave and Wireless Components Letters, 2005, 15, p. 844-846.
4. F. Martin, J. Bonache, F. Falcone, M. Sorolla, and R. Marqués, *Split ring resonator-based left-handed coplanar waveguide.* Applied Physics Letters, 2003, 83, p. 4652-4654.
5. M. A. Antoniades and G. V. Eleftheriades, *Compact Linear Lead/Lag Metamaterial Phase Shifters for Broadband Applications*. IEEE Antennas and Wireless Propagation Letters, 2003, 2, p. 103-106.
6. E. Erdil, K. Topalli, M. Unlu, O. A. Civi, and T. Akin, *Frequency Tunable Microstrip Patch Antenna Using RF MEMS Technology.* IEEE Transactions on Antennas and Propagation, 2007, 55, p. 1193-1196.
7. B. Pillans, J. Kleber, C. Goldsmith, and M. Eberly, *RF power handling of capacitive RF MEMS devices*. IEEE MTT-S International Microwave Symposium Digest, 2002, 1, p. 329-332.
8. N. Somjit, G. Stemme, and J. Oberhammer, *Power Handling Analysis of High-Power W-Band All-Silicon MEMS Phase Shifters*. IEEE Transactions on Electron Devices, 2011, 58, p. 1548-1555.
9. B. Jlassi and A. Merdassi, *Design methodology of a high power RF MEMS switch for wireless applications*. 4th Annual Caneus Fly by Wireless Workshop, 2011, p. 1-4.
10. D. Peroulis, S. P. Pacheco, and L. P. B. Katehi, *RF MEMS switches with enhanced power-handling capabilities.* IEEE Transactions on Microwave Theory and Techniques, 2004, 52, p. 59-68.
11. J.D. Barrera, G. H. Huff, S. R. White, N.R. Sottos, A. S. Griffin, and J.T. Bernhard, *A novel fluidic switch for high power applications.* 8th European Conference on Antennas and Propagation (EuCAP), 2014, p. 122-123.
12. A. J. King, J. F. Patrick, N. R. Sottos, S. R. White, G. H. Huff, and J. T. Bernhard, *Microfluidically Switched Frequency-Reconfigurable Slot Antennas*. IEEE Antennas and Wireless Propagation Letters, 2013, 12, p. 828-831.

4.5 Figures

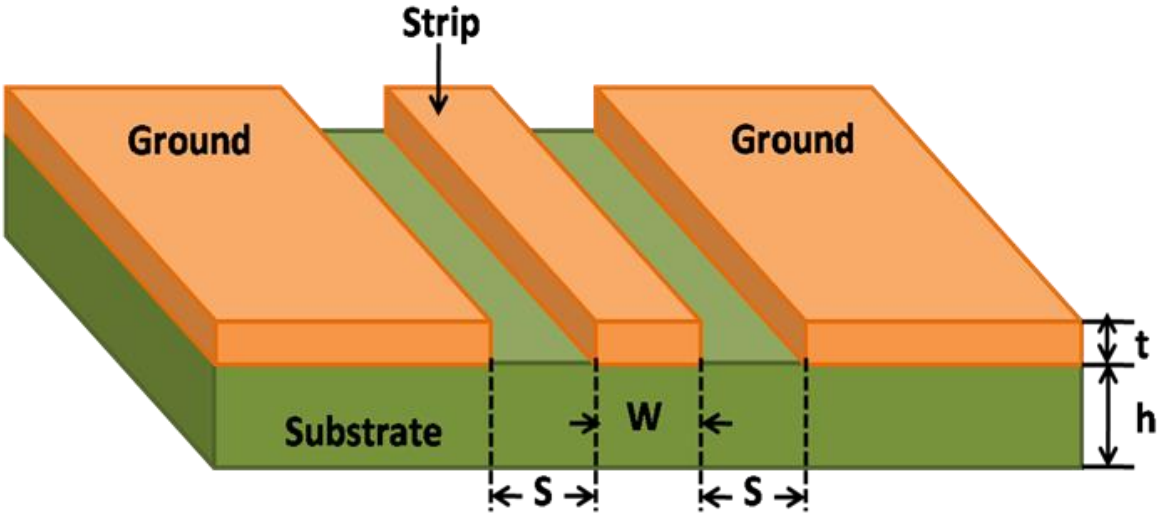

Figure 4.1. Isometric cross-section diagram of a simple CPW. The substrate consists of a dielectric material, while the ground planes and center strip are conductive copper traces. The width of the ground planes is much larger than the width (W) of the center strip in CPWs, while the thickness of the conductive layer (t) is small compared to the substrate thickness (h).

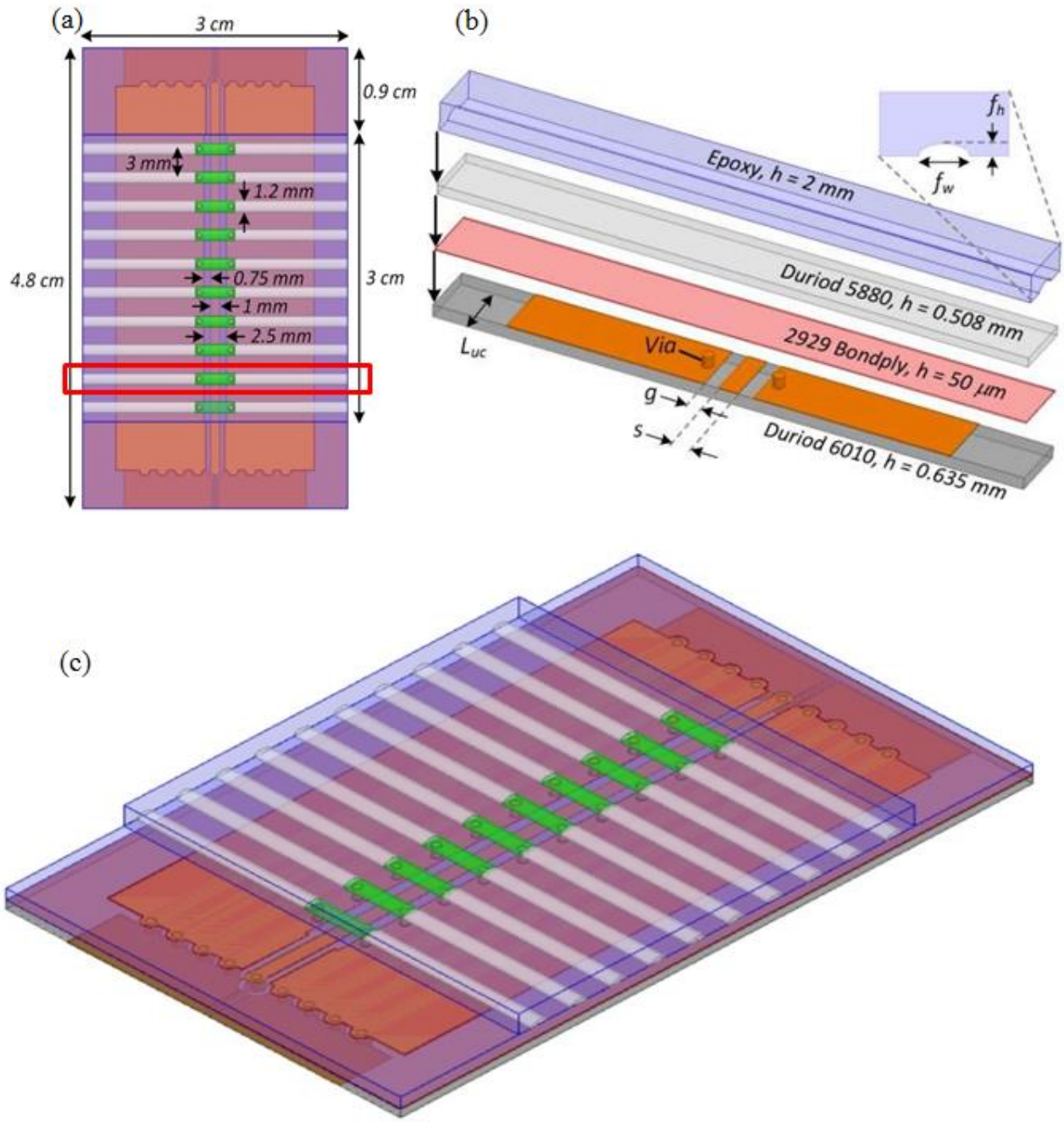

Figure 4.2. Initial fluidic phase reconfigurable CPW design. (a) Top view of assembled CPW with dimensions specified and a single unit cell highlighted in red. (b) Exploded isometric view of a single unit cell showing the layer stack sequence. Channel dimensions f_h = 0.6mm and f_w = 1.2mm. (c) Isometric view of the entire reconfigurable CPW assembly design with green sections representing where EGaIn will be placed within the channels.

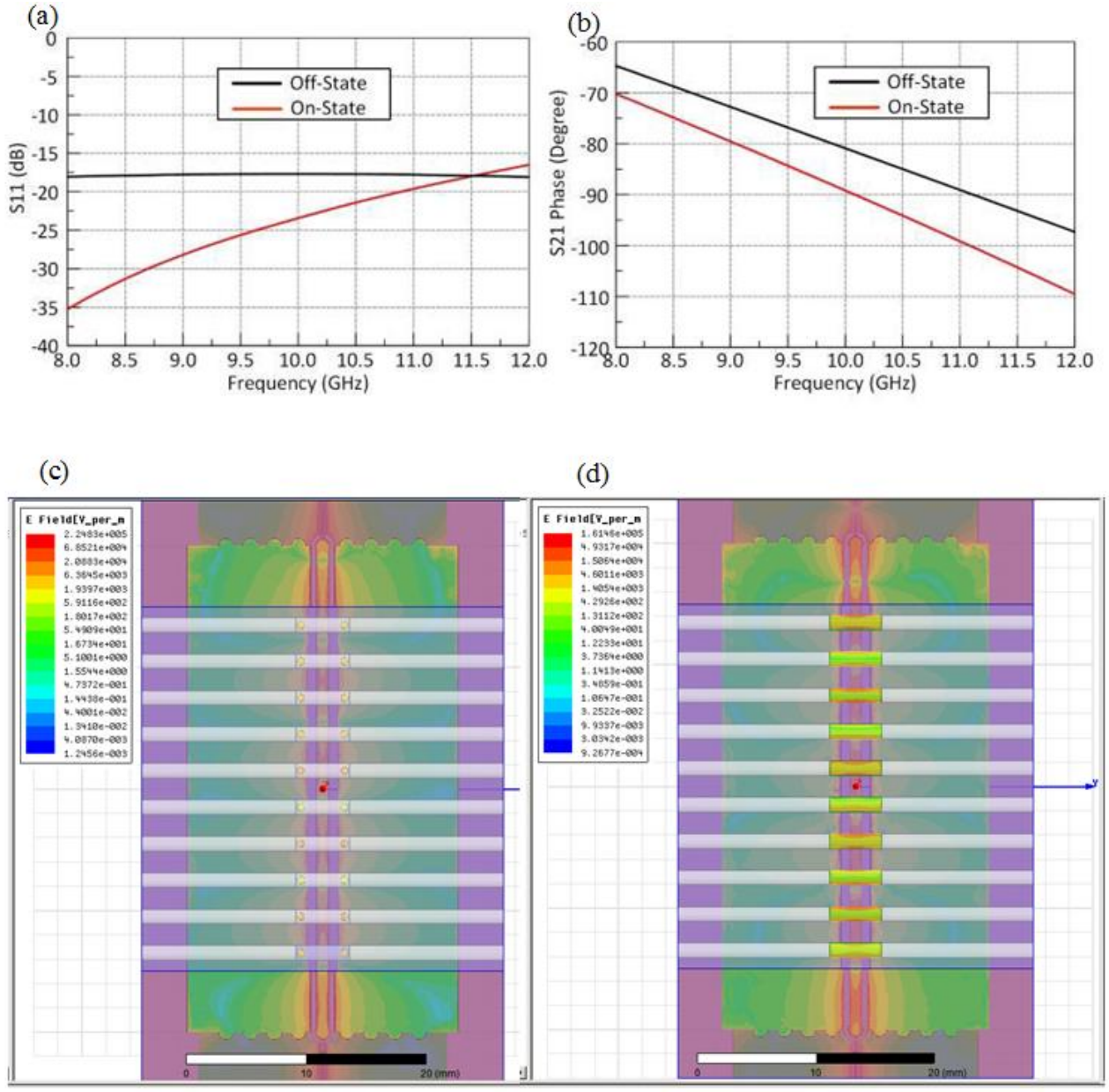

Figure 4.3. HFSS simulation results for the fluidic channel enabled phase reconfigurable CPW. (a) The return loss from 8 to 12 GHz for both the on and off states for a single unit cell, indicating a low loss over the entire frequency range of interest. (b) The S21 phase (test receiver phase relative to input phase) for both on and off states, with the difference at any given frequency being considered the phase shift. (c) In-plane electromagnetic field strength across the CPW when all channels are in the off state (unfilled). (d) In-plane electromagnetic field strength across the CPW when all channels are in the on state (filled). Note the shift in EM field strength peaks along the signal line between (c) and (d).

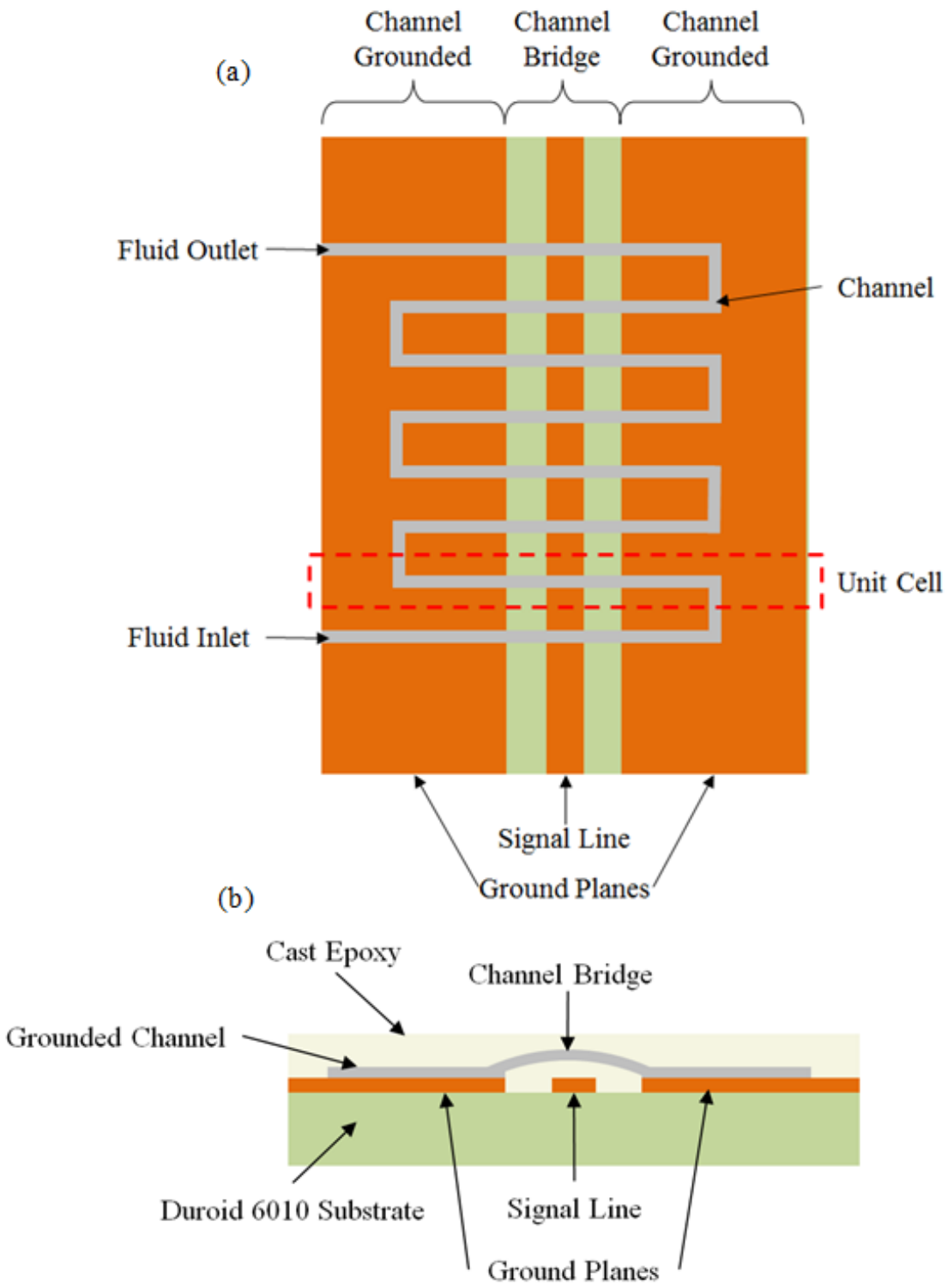

Figure 4.4. Revised design schematic for a phase reconfigurable CPW device using a single fluidic channel. (a) Top view showing the pathway of the channel periodically crossing over the signal line. (b) Profile view revealing where the channel is in contact with the ground planes.

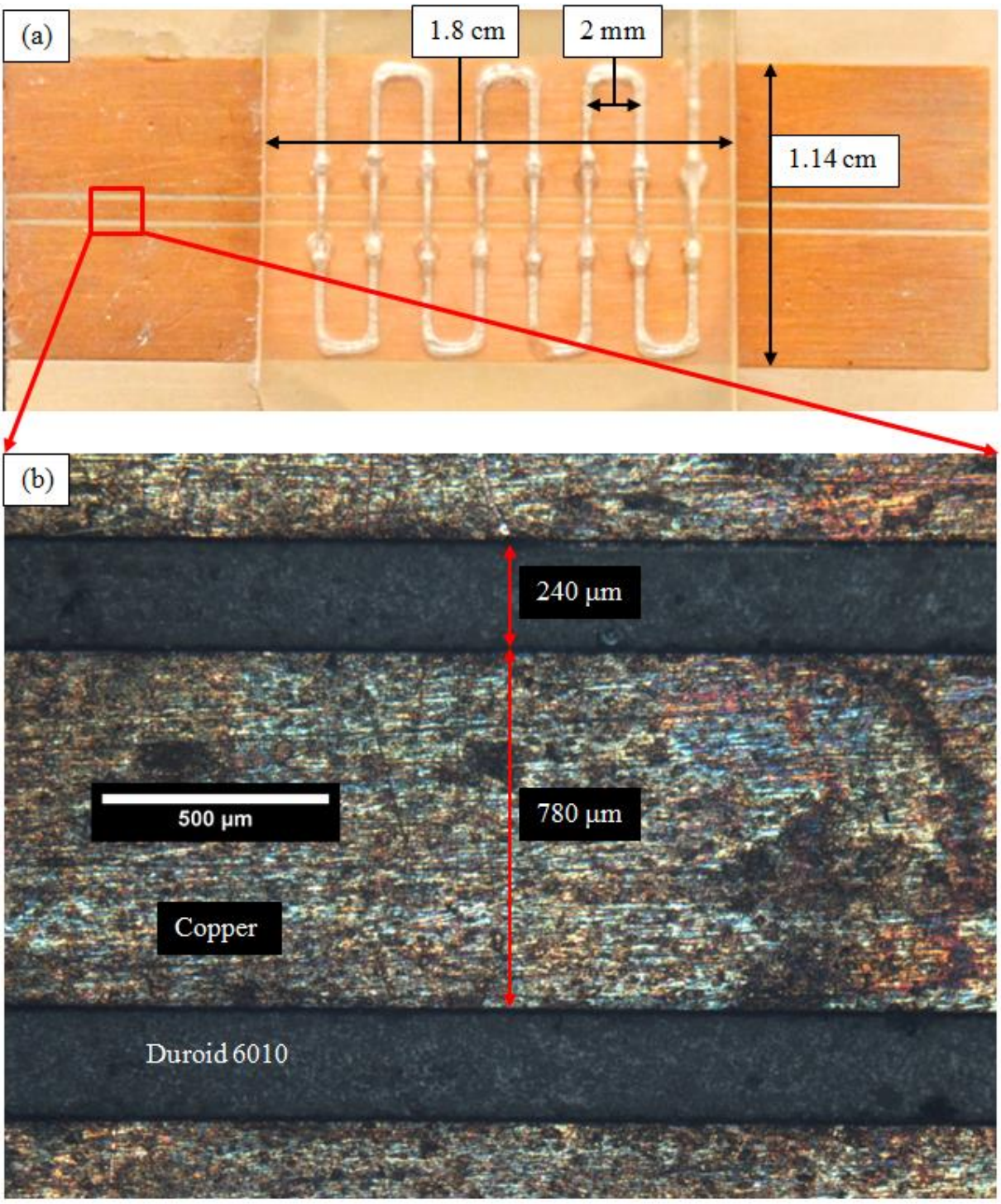

Figure 4.5. (a) Top view optical image of the fabricated 8-state phase reconfigurable CPW where the channel is completely filled with EGaIn. (b) Reflective light microscope top view of the signal trace and gaps with dimensions indicated.

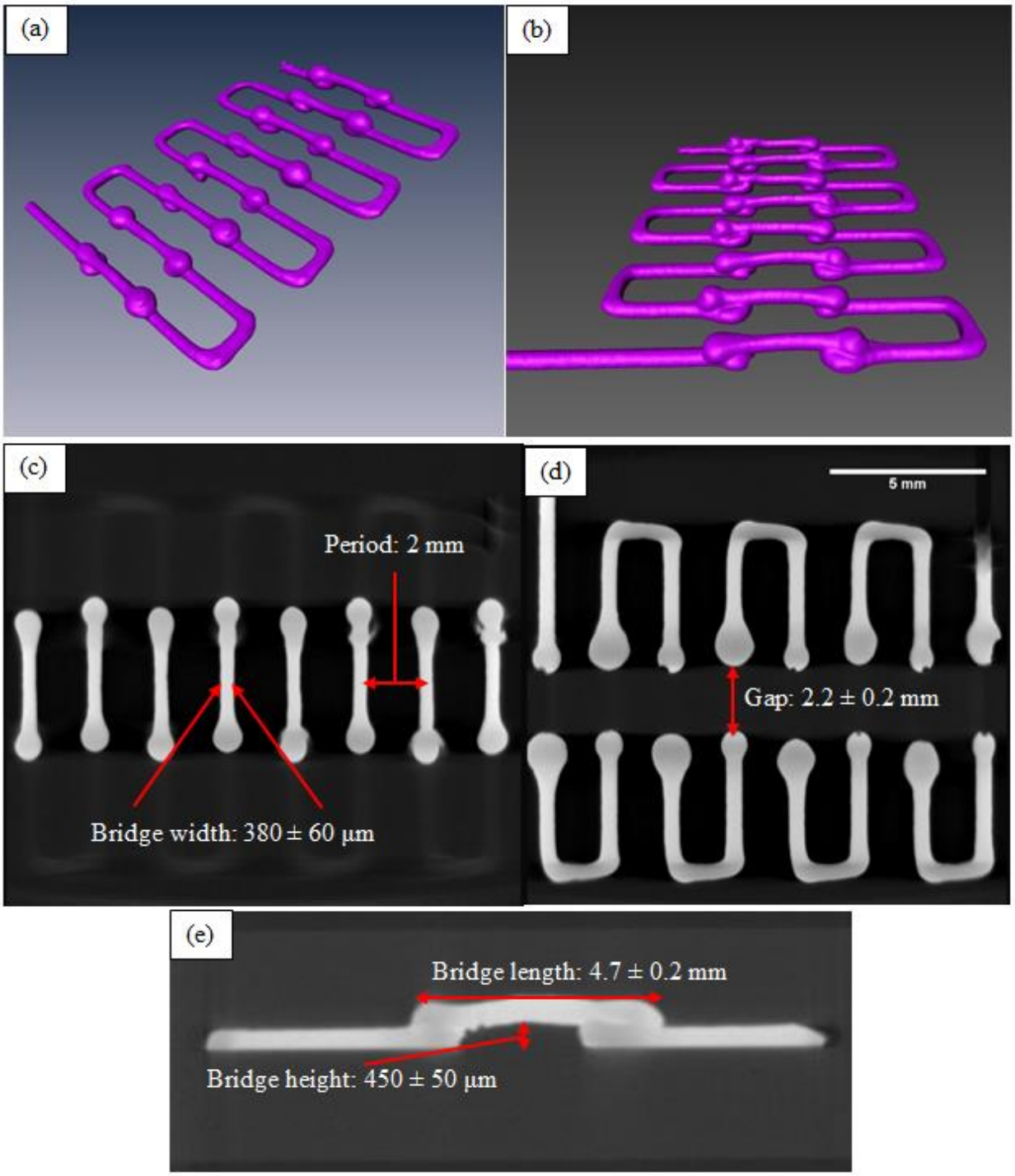

Figure 4.6. Images extracted from MicroCT scans of the fabricated network filled with EGaIn for contrast. (a) and (b) Isometric views of 3D reconstructions of the MicroCT scans showing the embedded channel architecture. (c) Overhead cross-section of the bridges, indicating key dimensions. (d) Overhead cross-section of the grounded layer, indicating the gap over which the bridge traverses. (e) Side cross-section of a bridge.

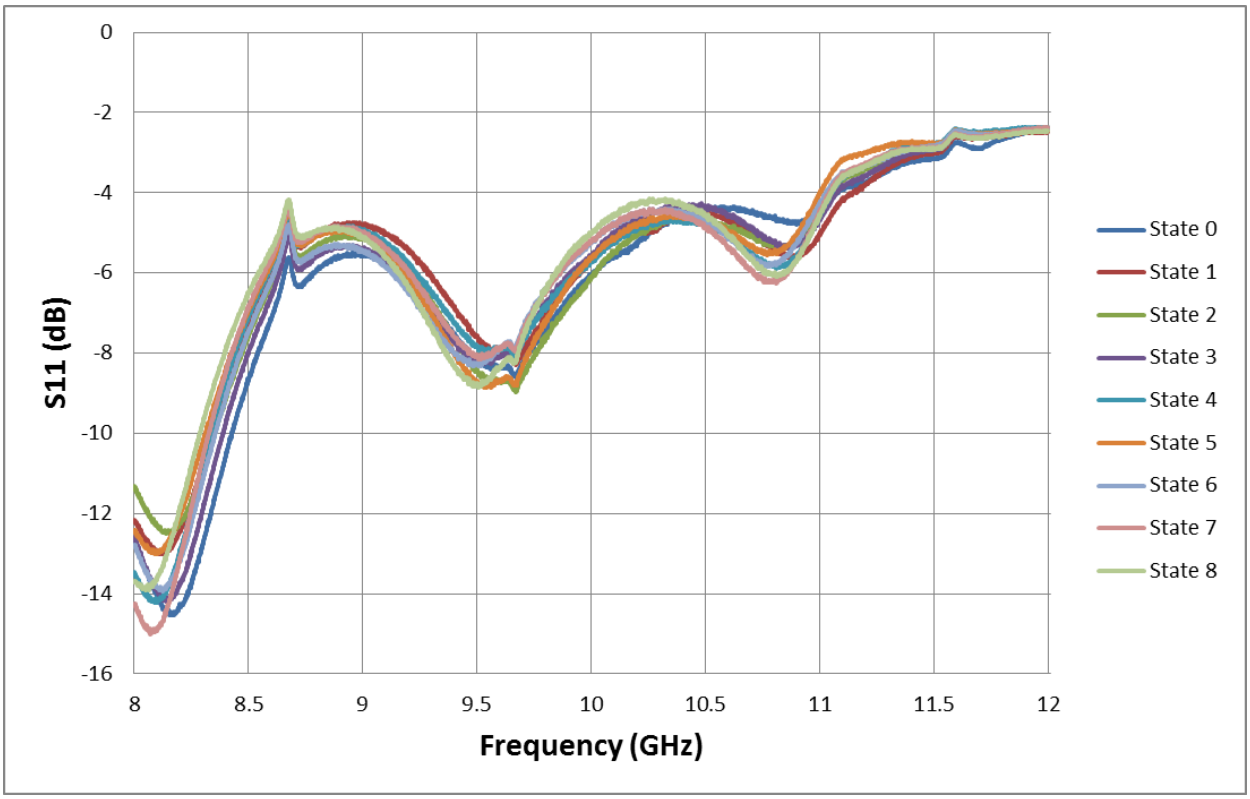

Figure 4.7. S11 as a function of frequency for all 8 states of the serpentine phase reconfigurable CPW. State 0 corresponds to an empty network, while in state 8 the network is completely filled with EGaIn. Maximum radiation efficiency is observed around 8.15 GHz with 94-97% power being transmitted. S11 for all 8 states is closely grouped across the frequency range, indicating all 8 bridges are operating in a similar manner.

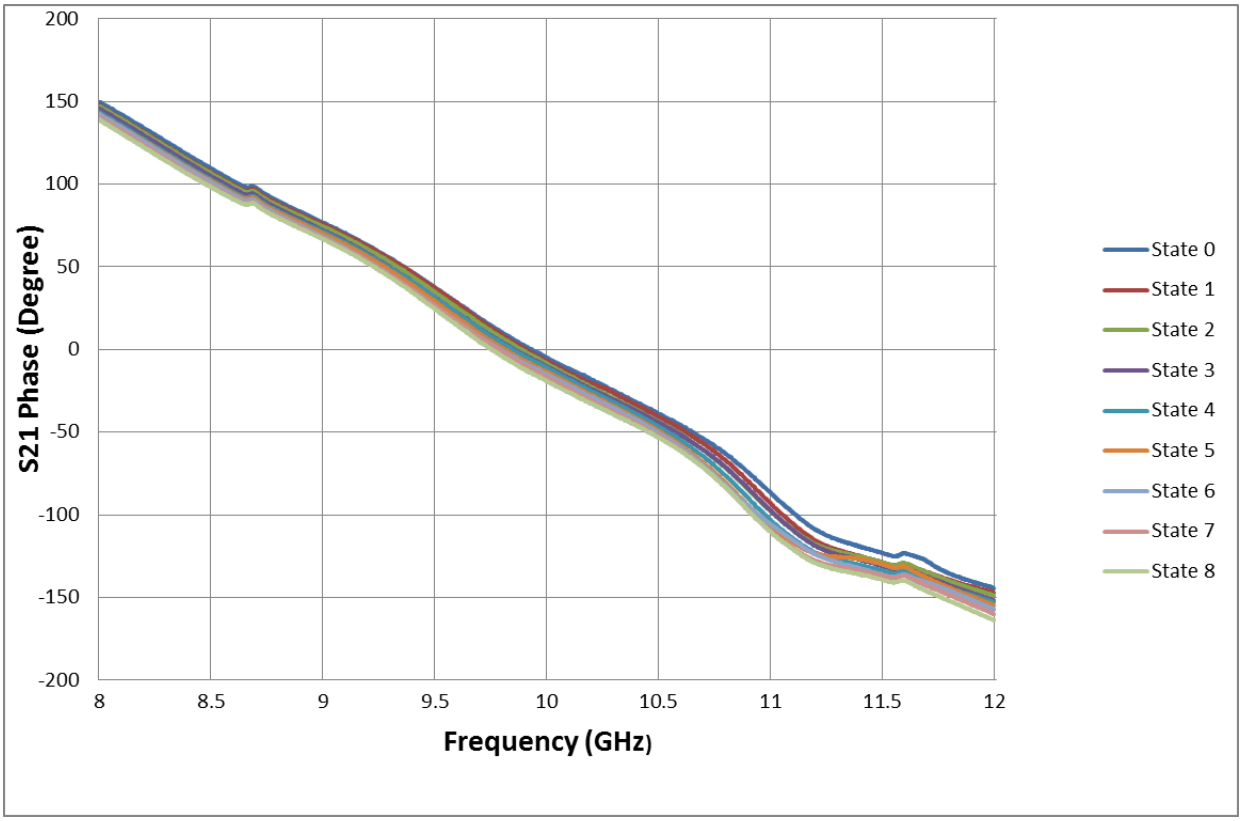

Figure 4.8. S21 phase as a function of frequency for all 8 states of the serpentine phase reconfigurable CPW. The average phase change between states is 1.83°, the maximum average phase shift between states is 2.43° at 12 GHz, and the minimum is 1.35° at 8 GHz. The phase shift at the frequency of maximum radiation efficiency (8.2 GHz) is 1.46°.

CHAPTER 5

POLARIZATION RECONFIGURABLE PATCH ANTENNA

5.1 Introduction

Microstrip patch antennas are a family of planar antennas with a wide variety of geometries for use in wireless communication, positioning, and radar applications. Advantages of patch antennas, which include their compact size, light weight, and ease of integration into circuit-board technology have led to widespread adoption of the technology and numerous studies on novel functions and applications.[1-3]

The fixed geometry of a given patch antenna provides limited functionality and results in a fixed resonant frequency, bandwidth and polarization.[4,5] Several approaches towards reconfiguration of patch antennas have been developed, including configuration of signal polarization in moving or rotating applications, such as personal mobile devices. Reconfiguration was achieved through electrical coupling of discrete patches to change the effective antenna geometry. The use of solid-state varactors, PIN diodes, and MEMS devices have been shown to alter polarization in patch antennas, but various problems such as interference, loss, and limited configurability control were encountered.[7-11] More recently, polarization reconfiguration was achieved with dielectric fluids in microfluidic channels. A direct comparison between fluidic reconfiguration with water and a solid-state approach with RF PIN diodes reveals that the fluidic method is more efficient and results in less cross-polarization.[12]

5.2 Single Channel Polarization Reconfigurable Antenna

An initial polarization reconfigurable antenna (PRA) design, shown in Figure 5.1, consisted of 2 orthogonal crossed microstrip patches with the four arms separated from the center feed patch by small (300 μm) gaps. A single channel (1.2mm wide and 600 μm in height) embedded in a cast epoxy layer (8605) passed directly over all four gaps. Conductive fluid within the channel shorted the gaps and electrically connected the arms to the center patch, where the sub-miniature type A (SMA) coaxial feed was located (Figure 5.1). Depending on the location of the fluid in the channel, an electrically continuous microstrip with a long axis along either the X or Y axis was formed. A similar design reported by Barrera and Huff [12] utilized water to change polarization states. In this work, EGaIn was used as the conducting fluid due to low viscosity (similar to water) with much lower resistivity ($29.4*10^{-6}$ Ω-cm).[13]

A single polarization state (either X or Y) with low cross-polarization was formed when the EGaIn liquid metal covered parallel gaps. A rectangular patch with long-axis perpendicular to the filled gaps was formed while the other two gaps remained open (Figure 5.2). The EGaIn was sectioned into isolated volumes with lengths equal to the gap lengths and separated by air. While this strategy previously worked well with water, a co-fluid was used with EGaIn to prevent oxide formation on the channel walls (Figure 5.2). Prevention of oxide formation was achieved by applying a small (500μm in length) section of aqueous HCl solution (5 w/wt%) to both ends of the two isolated volumes of EGaIn. The application of HCl sections allowed for movement of the EGaIn through the channel in either direction without leaving a residual oxide layer. HCl was not used to completely fill the space between EGaIn sections because of the relatively high conductivity of the aqueous solution.[14] Pressure is then applied on the channel inlet to move the EGaIn between orthogonal polarization states repeatedly.

S11 and voltage standing wave ratio (VSWR) measurements were obtained with a signal generator, network analyzer and anechoic chamber (Greg Huff Lab, ECE Department, Texas A&M University) for both polarization states (Figure 5.3). THE VSWR is defined

$$VSWR = \frac{1+|\Gamma|}{1-|\Gamma|}\ , \tag{5.1}$$

where Γ is the reflection coefficient, which is given by the ratio of the reflected (lost) voltage to the transmitted voltage.

$$\Gamma = \frac{V_r}{V_t}\,. \tag{5.2}$$

Low Γ values are indicative of good impedance matching and high power efficiencies, meaning that VSWR values near 1 are desirable. Both S11 and VSWR values at the resonance frequency show good impedance matching and high efficiency, with more than 95% of input power being transmitted in both polarization states. An operating (resonance) frequency of 2.45 GHz is observed for both states, which is advantageous since the antenna is meant to switch between polarization states while maintaining the same operating frequency. Figure 5.4 shows the radiation pattern for the X polarization state in the XZ plane, where E_θ is the θ polarized component of the electric field and E_ϕ is the ϕ polarized component of the electric field. The radiation pattern for the Y state was not obtained. Due to rotation of the antenna in the anechoic chamber the EGaIn sections moved unexpectedly within the channel. Placement of EGaIn was overly sensitive to any movement of the antenna or slight pressure differences on either end of the channel.

5.3 Dual Channel Polarization Reconfigurable Antenna

The sensitivity of the microvascular EGaIn switching mechanism to pressure, movement, and precise positioning within the single channel PRA motivated a second generation design, shown in Figure 5.5. Although the copper patches and overall antenna dimensions were the same as described in Section 5.2, the vascular network architecture and epoxy layer were altered. Instead of a single channel passing over all four patch gaps, a dual network system was adopted so that each gap was covered by a discrete channel. This dual network architecture allowed polarization states (X and Y) to be activated independently of each other using separate fluid delivery systems (Figure 5.5). Vertical vias were drilled through the substrate and ground plane at each end of the discrete gap-covering channels to allow for fluid delivery through a branched back-side network behind the ground plane. This channel placement prevented additional transmission-line modes interfering with the antenna since all effects of the EGaIn in the network on the back-side of the device are screened out by the ground plane. Delivery of EGaIn to parallel gap channels was achieved by completely filling one of the two networks which configured the antenna to a given polarization state. 3D microCT scan reconstructions of both X and Y polarization networks are shown in Figure 5.6, indicating the location of the gap-covering active network portions, vertical vias, and back-side delivery networks.

S11, VSWR, and full radiation patterns were obtained for both X and Y polarization states in the same manner as the previous single channel design (Figures 5.7 and 5.8). The operating frequencies in both X and Y polarized states remained around 2.45 GHz, and low cross-polarization was observed, demonstrating operation similar to that of the previous design. Radiation efficiencies were similar to the values from the previous design for the X polarization state. The Y polarization state was slightly less efficient with a minimum S11 of -8 dB,

corresponding to a power efficiency of 84%. The decreased efficiency was mainly attributed to small amounts of EGaIn in contact with the ground plane as it is passes through the vertical vias, partially grounding the entire antenna structure. Since the lower efficiency was only seen in the Y polarization state, we hypothesize the ground plane was not exposed to every vertical via. This problem can be prevented by milling out 1mm circles in the ground plane around the vertical vias, preventing unwanted contact of the EGaIn and the ground plane.

5.4 References

1. D. M. Pozar, *Microstrip antenna coupled to a microstrip-line.* Electronics Letters, 1985, 21, p. 49-50.
2. K. L. Virga and Y. Rahmat-Samii, *Low profile enhanced-bandwidth PIFA antennas for wireless communications packaging.* IEEE Transactions on Microwave Theory and Technology, 1997, 45, p.1879-1888.
3. I. Papapolymerous, R. F. Drayton, and L. P. B. Katehi, *Micromachined patch antennas*. IEEE Transactions on Antennas and Propagation, 1998,46, p. 275–283.
4. N. Herscovici, *New considerations in the design of microstrip antennas*. IEEE Transactions on Antennas and Propagation, 1998, 46, p. 807–812.
5. F. Yang, X.X. Zhang, X. Ye, and Y. Rahmat-Samii, *Wide-band E-shaped patch antenna for wireless communications.* IEEE Transactions on Antennas and Propagation, 2001, 49, p. 1094-1100.
6. F. Yang and Y. Rahmat-Samii, *A reconfigurable patch antenna using switchable slots for circular polarization diversity*. IEEE Microwave and Wireless Components Letters, 2002, 12, p. 96-98.
7. Y. J. Sung, T.U. Jang, and Y.S. Kim, *A reconfigurable microstrip antenna for switchable polarization.* IEEE Microwave and Wireless Components Letters, 2004, 14, p. 534-536.
8. C. Rui-Hung and J. S. Row, *Single-fed microstrip patch antenna with switchable polarization.* IEEE Transactions on Antennas and Propagation, 2008, 56, p. 922–926.
9. T. Jia-Fu and R. Jeen-Sheen, *Reconfigurable square-ring microstrip antenna*. IEEE Transactions on Antennas and Propagation, 2013, 61, p. 2857–2860.
10. X.X. Yang, B.C. Shao, F. Yang, A.F. Elsherbeni, and B. Gong, *A polarization reconfigurable patch antenna with loop slots on the ground plane*. IEEE Antennas Wireless Propagation Letters, 2012, 11, p. 69–72.
11. G. H. Huff and J. T. Bernhard, *Integration of packaged RF MEMS switches with radiation pattern reconfigurable square spiral microstrip antennas*. IEEE Transactions on Antennas and Propagation, 2006, 54, p. 464–469.

12. J.D. Barrera and G.H. Huff, *A fluidic loading mechanism in a polarization reconfigurable antenna with a comparison to solid state approaches*. IEEE Transactions on Antennas and Propagation, 2014, 62, p. 4008-4014.
13. M. D. Dickey, R. C. Chiechi, R. J. Larsen, E. A. Weiss, D. A. Weitz, and G. M. Whitesides, *Eutectic Gallium-Indium (EGaIn): A Liquid Metal Alloy for the Formation of Stable Structures in Microchannels at Room Temperature.* Advanced Functional Materials, 2008, 18, p. 1097-1104.
14. *FILMTEC Membranes Technical Manual Excerpt.* DOW Chemical Company, Liquid Seperations Division, Midland, MI. Retrieved May, 2015.

5.5 Figures

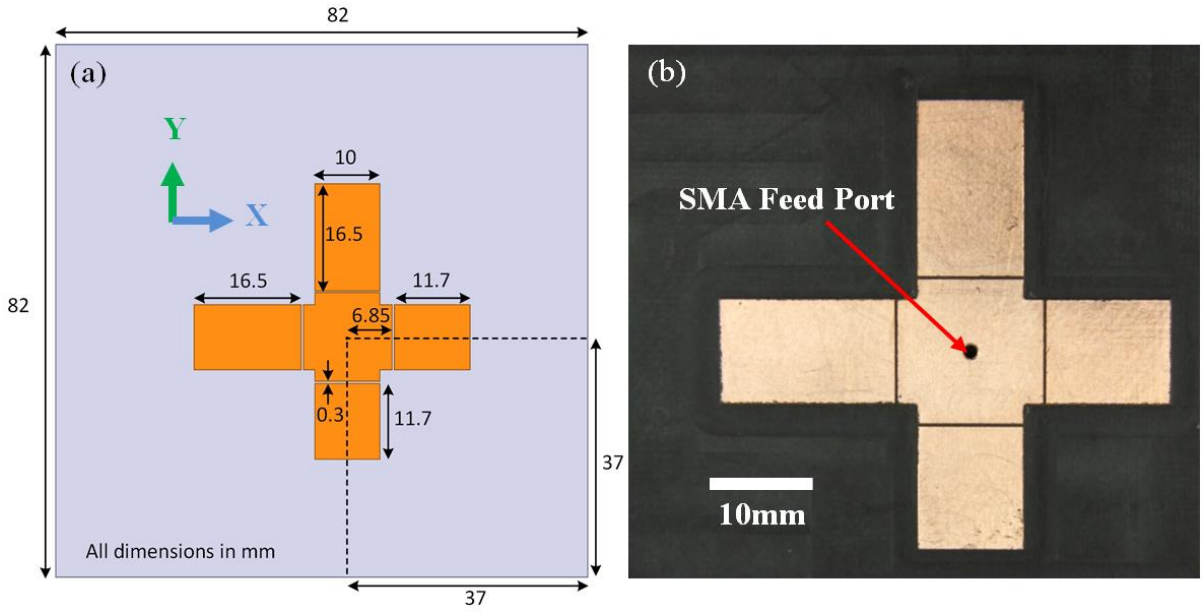

Figure 5.1. Bare patch antenna with four arms which are disconnected from the center patch. (a) Top view schematic with patch dimensions and axis conventions. (b) Optical image of the bare patch antenna with the SMA connection port noted.

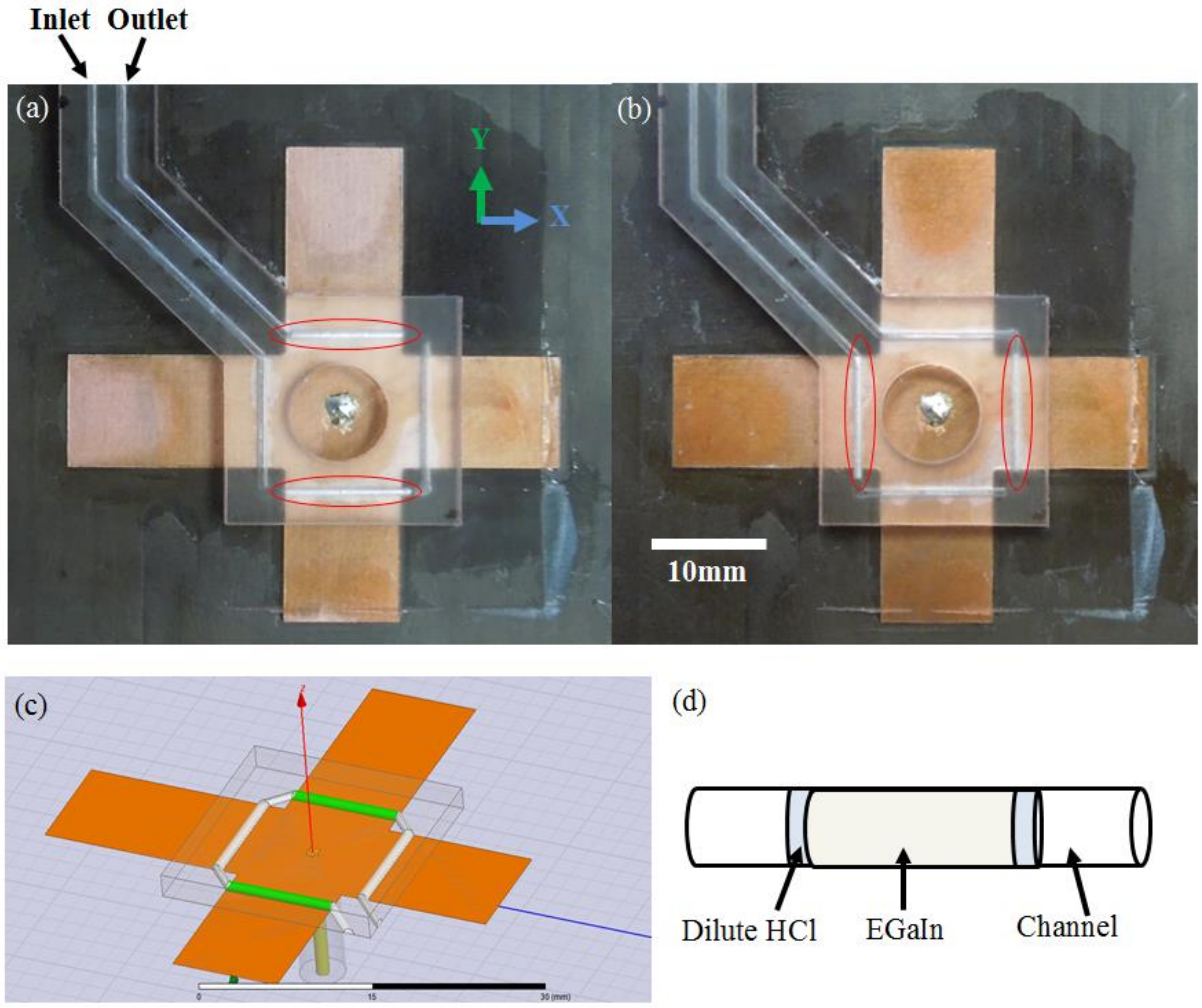

Figure 5.2. PRA with a single channel in an epoxy layer to achieve reconfigurability. (a) Antenna with EGaIn sections, circled in red, connecting patch segments along the Y-axis, forming the Y polarization state. (b) PRA with EGaIn sections connection patch segment along the X-axis, forming the X polarization state. (c) Isometric schematic showing the PRA in the Y polarization state, with ideal EGaIn sections as the green segments in the single channel. Note that parallel gaps are covered with EGaIn but the other two gaps are left open. (d) Schematic of the EGaIn section in the channel showing the HCl end-caps which prevent gallium oxide formation on the channel walls.

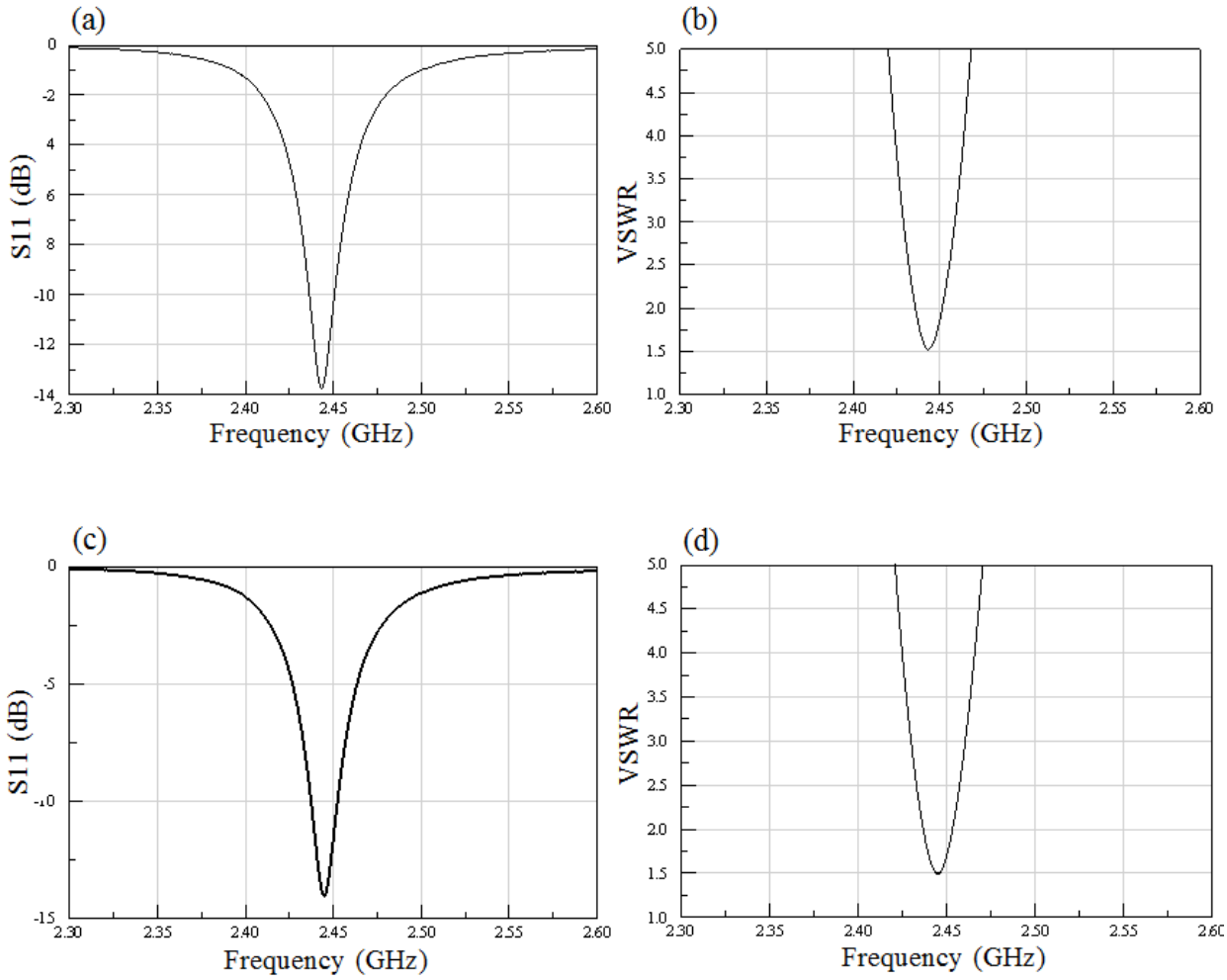

Figure 5.3. RF testing results for the single channel PRA. (a) S11 as a function of frequency for the Y polarized state. (b) VSWR as a function of frequency for the Y polarized state. (c) S11 as a function of frequency for the X polarized state. (d) VSWR as a function of frequency for the X polarized state. Note the minimums in S11 and VSWR are indicative of the operating (resonance) frequency and radiation efficiency.

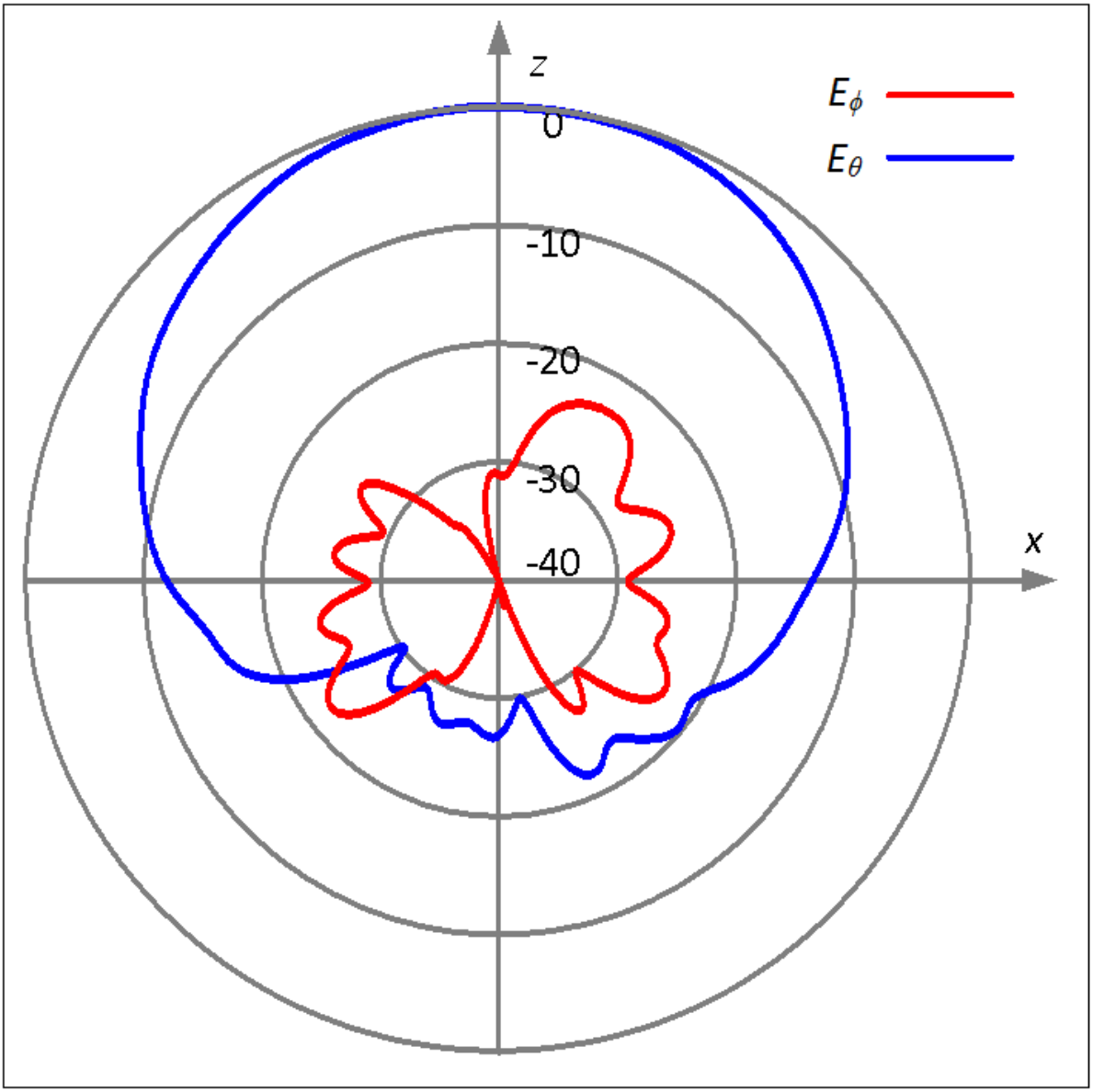

Figure 5.4. Full electric field radiation pattern for the X polarized state on the XZ plane. Units are decibels (logarithm to base 10 of the ratio of the radiation power to the maximum radiation power along the Z axis). The radiation consists of ϕ and θ polarized waves, where E_θ is the component of the electric field polarized in the selected direction along the XZ plane at any given angle. E_ϕ is the undesired component of the electric field polarized in the orthogonal direction.

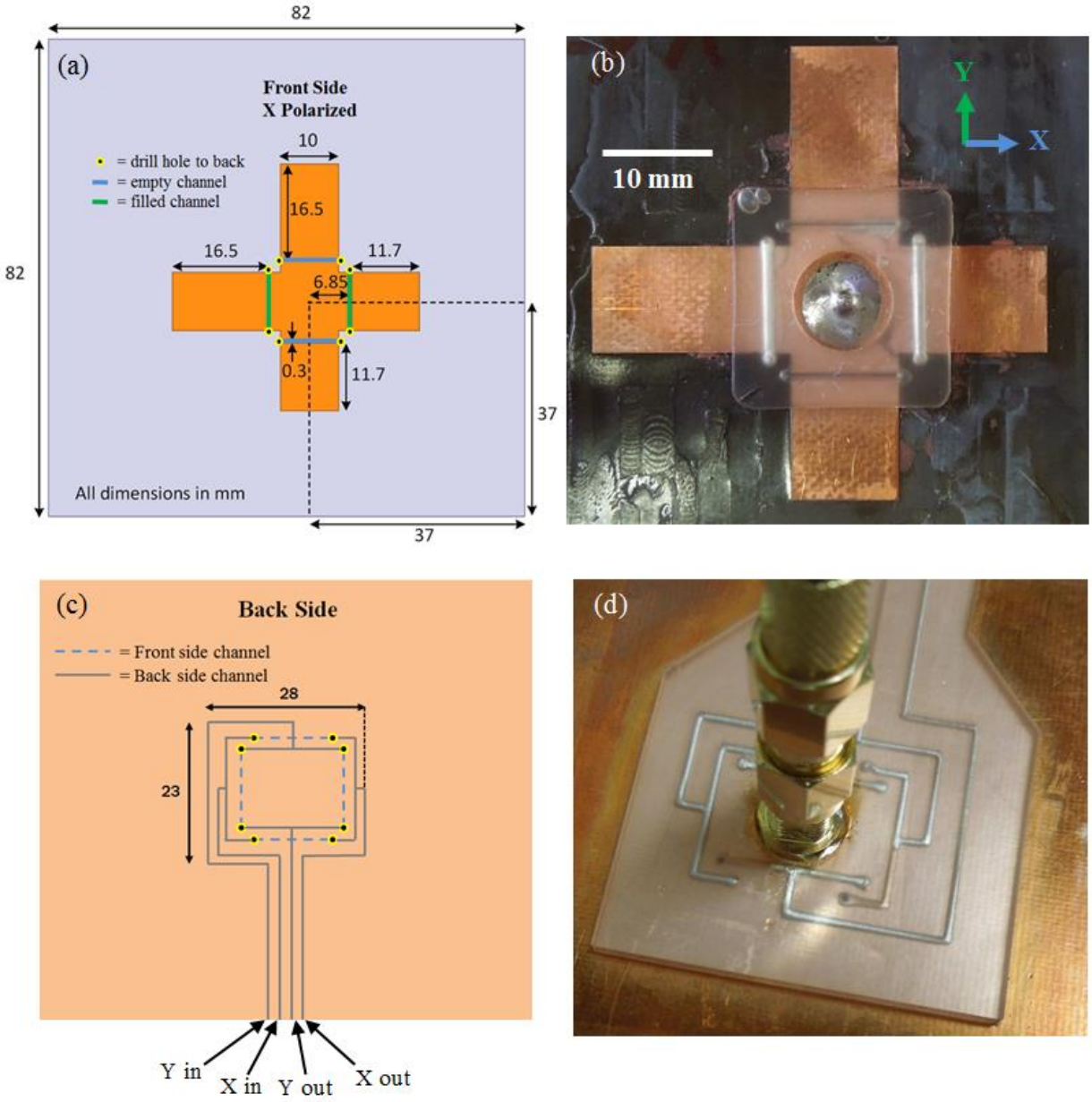

Figure 5.5. PRA with dual 3D networks to achieve reconfiguration. (a) Schematic of the patch antenna in the X polarization state for example. (b) PRA in the X polarization state; EGaIn can clearly be seen in the two parallel channels. The SMA feed is soldered on in the middle. (c) Schematic of the delivery network located behind the ground plane. (d) Back side delivery network in epoxy being filled with EGaIn. The large cable in the center is the SMA feed.

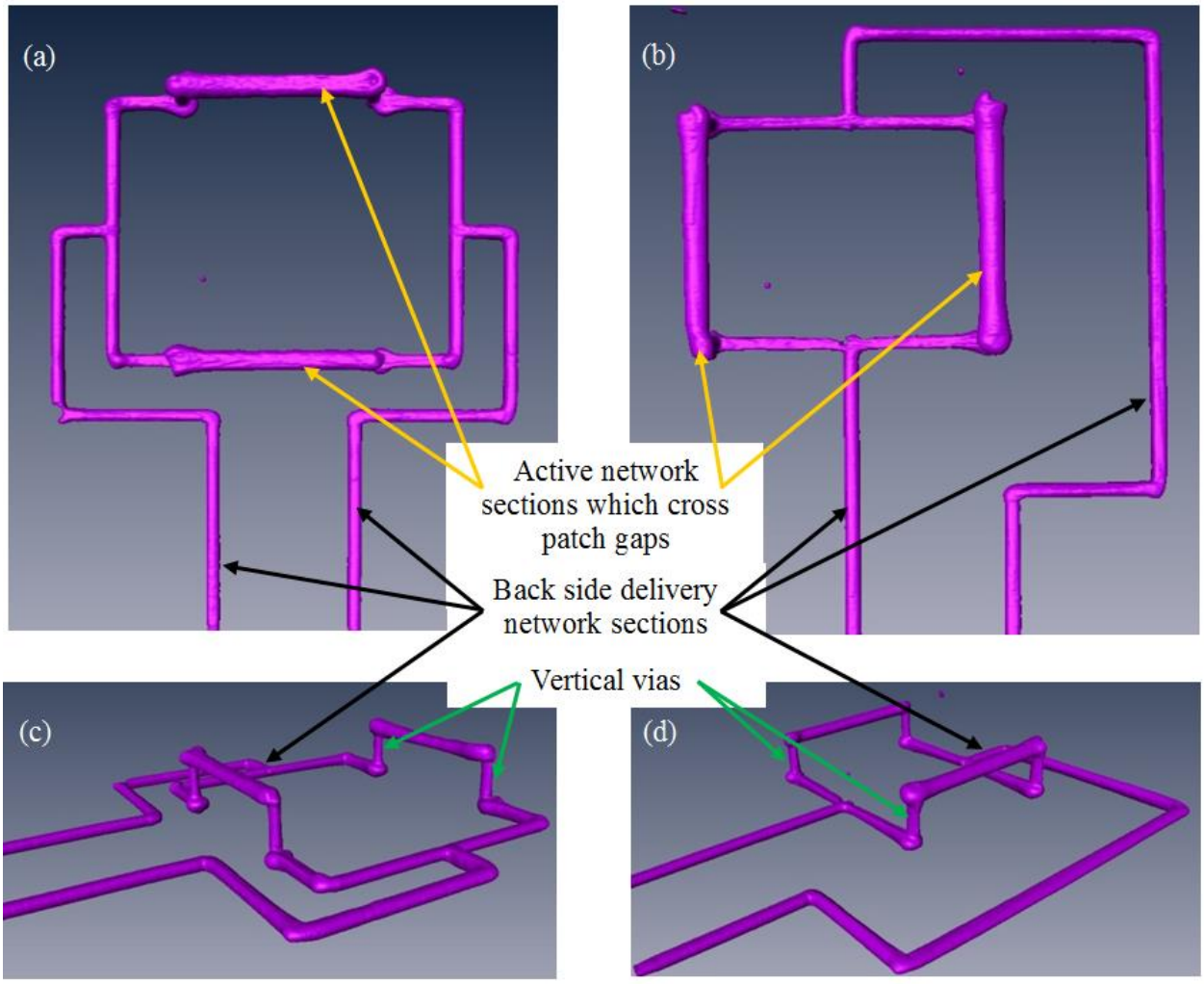

Figure 5.6. Reconstructed microCT scans of both networks filled with a radiocontrast agent for imaging. Important features are noted for all scans. (a) Top-down view of the filled Y polarization state network, (b) top-down view of the filled X polarization state network, (c) isometric view of the filled Y polarization network, and (d) isometric view of the filled X polarization network. Note that the two networks are completely separate and the vertical vias which carry fluid from behind the ground plane to the active patch antenna. The back side delivery networks are completely screened from the active components by the ground plane.

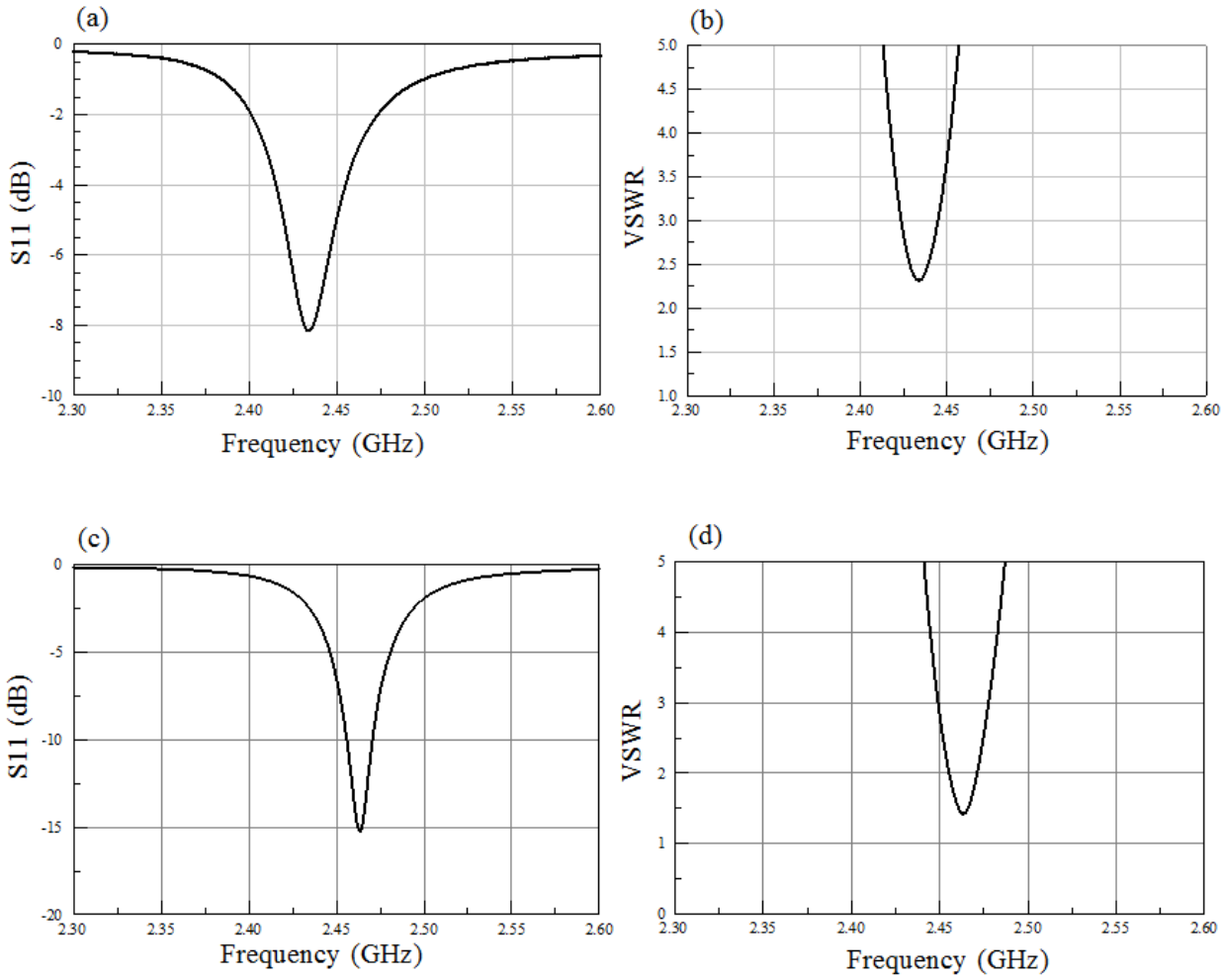

Figure 5.7. RF testing results for the dual network PRA. (a) S11 as a function of frequency for the Y polarized state. (b) VSWR as a function of frequency for the Y polarized state. (c) S11 as a function of frequency for the X polarized state. (d) VSWR as a function of frequency for the X polarized state. Minimums in S11 and VSWR are indicative of the operating frequency and radiation efficiency.

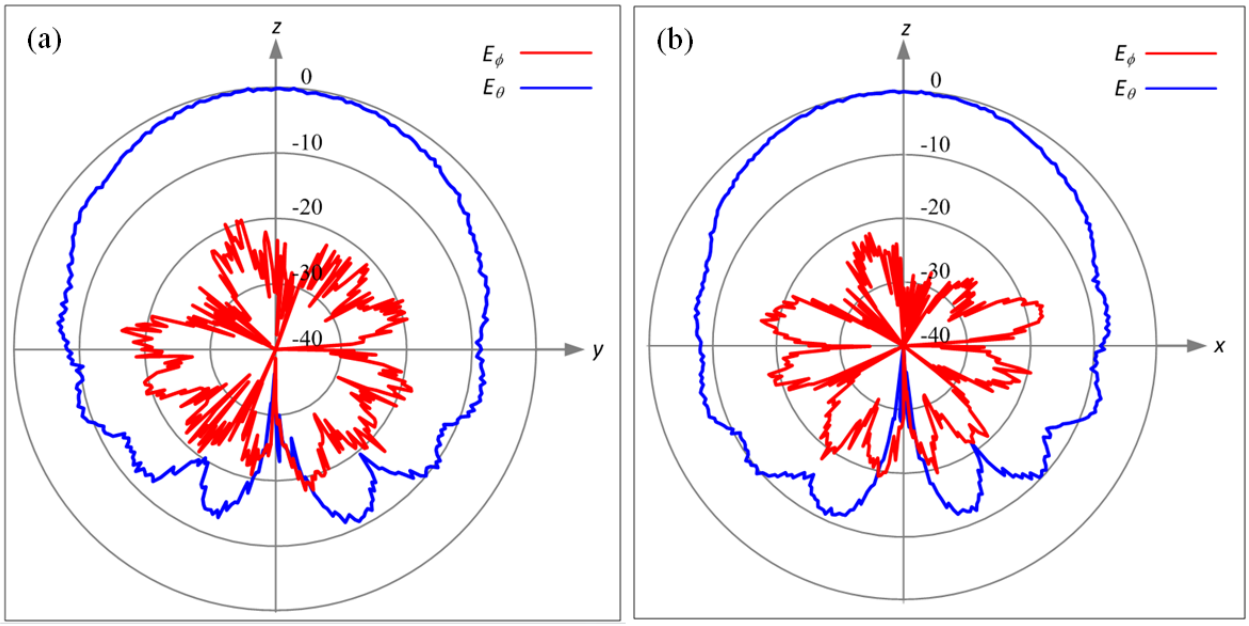

Figure 5.8. Full electric field radiation patterns for the dual network PRA, with units of decibels. (a) Y polarized state electric field radiation pattern on the YZ plane. (b) X polarized state electric field radiation pattern on the XZ plane. In both cases E_θ is the component of the electric field which is polarized in the selected direction when viewed from respective planes.

CHAPTER 6

CONCLUSIONS AND FUTURE WORK

6.1 Conclusions

This thesis provides a description of general fabrication techniques developed for embedded microvascular networks in reconfigurable signal devices. The work presented here is motivated by the use of microvascular systems in other material applications and recent investigations into reconfigurable RF devices.

A selection process was performed to identify materials with desirable structural, thermal, and electronic properties. Electronic substrate composites commonly used in RF applications were first selected, followed by a structural epoxy with desirable dielectric properties which was successfully able to be vascularized using 3D printing of a sacrificial ink. A bonding procedure was developed which utilized etching of substrates as well as active copper traces, followed a conductive silane treatment. This procedure allowed for adhesion between the vascularized epoxy layer and the electronic substrate. Finally, a low viscosity liquid metal, eutectic gallium indium, which forms ohmic contact with copper traces which have undergone the bonding treatment, was identified. The metal was even able to form ohmic contact with copper test traces when contained within microchannels.

Using these materials and techniques, two reconfigurable radio frequency signal devices were designed, fabricated, and evaluated. The first was a co-planar waveguide with a grounded microvascular network which passed over the active signal line. This enabled signal radiation

phase shifts, with nine total reconfigurable states based on the location of the liquid metal within the vascular network. The average phase difference between each state for the entire frequency range was 1.83°, with an average phase difference of 1.46° per state and total phase difference of 11.5° observed at the resonance frequency. The second application was a cross patch antenna with microvascular networks in direct contact with the patch gaps, allowing for two-state signal radiation polarization configurability. Two versions of this reconfigurable antenna were developed, the first with a single planar network, and the second with dual 3D networks. While the single network approach provided high radiation efficiency, switching and fluid placement were extremely difficult to control. The second network provided simple switching and did not required precise fluid placement, but parasitic contact to the ground plane decreased radiation efficiency from -14 dB to -8 dB. Radiation efficiency in the X polarized state remained high at 15 dB. Both states generated highly polarized electric fields in the selected directions.

6.2 Future Work

Immediate future work will consist of slight alterations in design and fabrication of both phase reconfigurable CPWs and polarization reconfigurable patch antennas. The CPW serpentine network design will continue to be used, however thicker channels and more unit cells will be fabricated to improve the range and diversity of phase configurability. An increase in channel width will result in a higher phase shift per unit cell, while more unit cells allow for a greater overall range in signal phase. Efficiency issues encountered in the phase reconfigurable patch antenna will be addressed with a second design using the dual network architecture will be fabricated and evaluated. This new design will incorporate an additional insulating layer between the ground plane and the back side delivery network and milled out areas of the ground plane

around the vertical vias to assure no contact is made between the ground plane and conductive fluid within the delivery network.

Further future work will consist of incorporating electronically active vasculature into structural composites. Due to the easily deformable nature of the sacrificial ink used for this thesis, a newly developed technique known as Vascularization of Sacrificial Components (VaSC) will be utilized to form vascular channels.[1,2] This process is achieved by sublimating catalyst-treated PLA fibers which are incorporated into a host matrix in order to form vasculature, as seen in Figure 6.1. The versatility of this method has allowed for the fabrication of a wide range of structures from 0D spheres to intricate 3D networks.[3]

Three systematic methodologies will be utilized in order to incorporate reconfigurable electronic devices into structural composites (Figure 6.2). The first method will employ VaSC technology to create vascular composites directly on top of PTFE/copper antenna substrates. Composites can be manufactured through either a vacuum-assisted resin transfer molding (VARTM) or prepreg lamination. In both cases sacrificial VaSC structures will be incorporated into the composite preform prior to curing. The second method will employ 3D printing of VaSC materials directly onto PTFE/copper antenna substrates. In this case, more complex architectures that can be used for a wider range of reconfigurations are possible. Finally, the third approach will utilize liquid metal within a vascular network as the active electronic devices, thereby removing the traditional copper parts and non-structural substrate (PTFE), providing superior mechanical properties. This approach also has potential for wireless damage detection within the composite. In this case the fluid will be an active RF signal device, and cracks in the composite during damage events will result in flow of conductive fluid from the vascular networks into

damage regions. This will change the device geometry and thus resonance frequency, which can be detected by signal receivers, alerting them that some damage has occurred.

Finally, the use of electronically active fluids within microvascular networks can be combined with other functionalities, such as self-healing and cooling. This can be accomplished by incorporating conductive colloids into self-healing and/or coolant fluids, allowing for vascularized composite materials which utilize electronic functionality to monitor and even trigger other functions.

6.3 References

1. H. Dong, A.P. Esser-Kahn, P.R. Thakre, J.F. Patrick, N.R. Sottos, S.R. White, and J.S. Moore, *Chemical Treatment of Poly(lactic acid) Fibers to Enhance the Rate of Thermal Depolymerization.* Applied Materials and Interfaces, 2012, 4, p. 503-509.
2. A.P. Esser-Kahn, P.R. Thakre, H. Dong, J.F. Patrick, V.K. Vlasko-Vlasov, N.R. Sottos, J.S. Moore, and S.R. White, *Three-Dimensional Microvascular Fiber-Reinforced Composites*. Advanced Materials, 2011, 23, p. 3654-3658.
3. R.C.R. Gergely, S.J. Pety, B.P. Krull, J.F. Patrick, T.Q. Doan, A.M. Coppola, P.R. Thakre, N.R. Sottos, J.S. Moore, and S.R. White, *Multidimensional Vascularized Polymers using Degradable Sacrificial Templates.* Advanced Functional Materials, 2015, 25, p. 1043-1052.

6.4 Figures

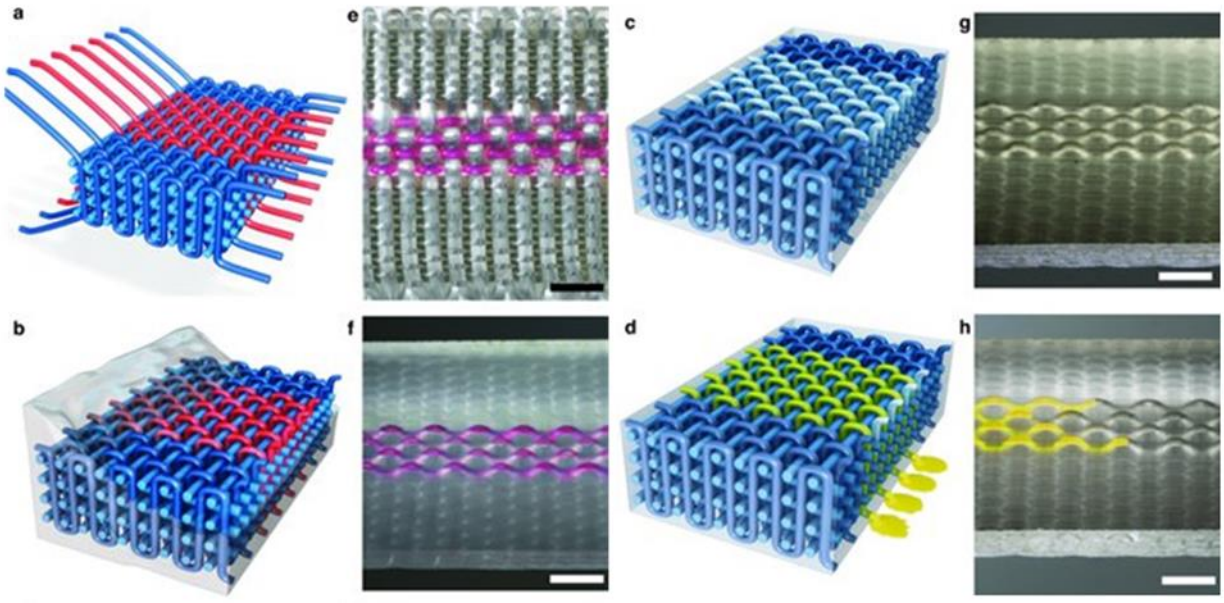

Figure 6.1. Schematics of (a) sacrificial fibers being woven into the composite fabric preform; (b) resin infiltration of the preform; (c) VaSC process where the sacrificial fibers are sublimated, leaving hollow channels in the finished composites, and (d) fluid being passed through the resulting vasculature. Optical images of (e) catalyst-treated fibers incorporated into a 3D woven fabric preform; (f) the same fibers after resin infiltration and curing; (g) channels resulting from the VaSC procedure and (h) dyed fluid in the channels. All scale bars = 5mm. Figure adapted from [2].

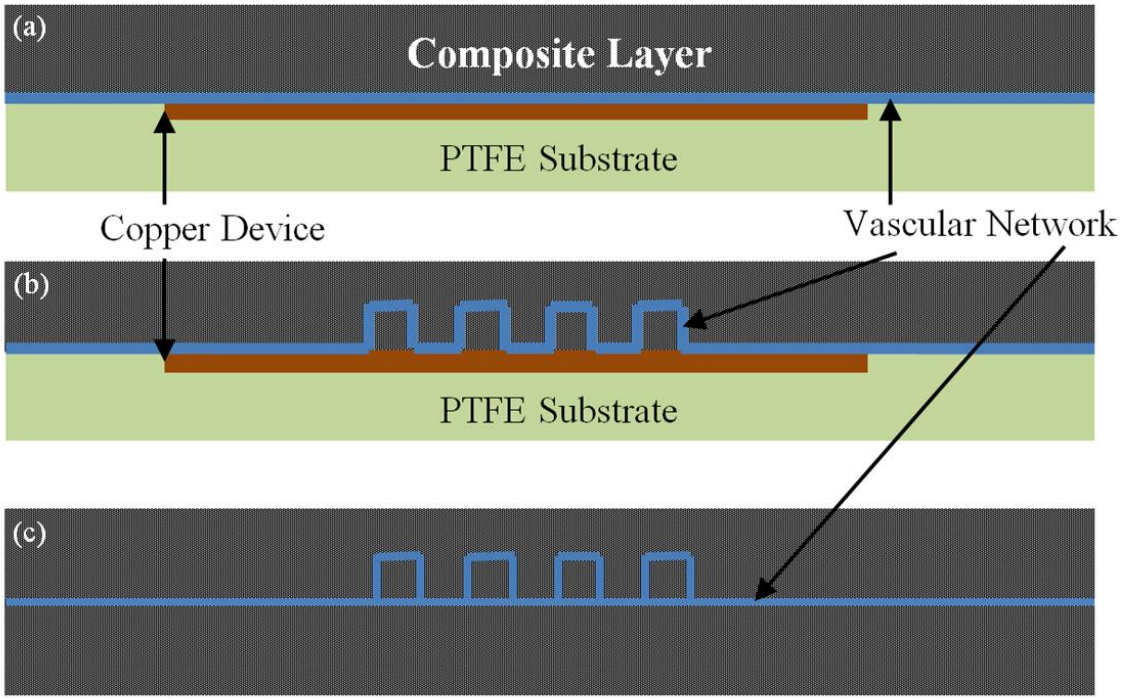

Figure 6.2. Cross-sectional schematics of reconfigurable signal devices produced through: (a) the first proposed fabrication methodology where vasculature is placed directly on the active signal device, (b) the second fabrication methodology where 3D printing is used to create the vascular architecture, and (c) the third fabrication methodology where conductive fluid within the vasculature is used as the active signal device.